Graduate Theses and Dissertations   Graduate School

11-10-2015

Use of FDM Components for Ion Beam and Vacuum Applications

Eric Miguel Tridas
University of South Florida, eric.m.tridas@gmail.com

www.manaraa.com

Use of FDM Components for Ion Beam and Vacuum Applications

by

Eric M. Tridas

A dissertation submitted in partial fulfillment
of the requirements for the degree of
Doctor of Philosophy
Department of Mechanical Engineering
College of Engineering
University of South Florida

Co-Major Professor: Rudiger Schlaf, Ph.D.
Co-Major Professor: Rasim Guldiken, Ph.D.
Matthias Batzill, Ph.D.
Nathan Crane, Ph.D.
Jing Wang, Ph.D.

Date of Approval:
October 30, 2015

Keywords: Ion Funnel, SIMION, Flexible PCB,
Fused Deposition Modeling, Electroplating

DEDICATION

For Rachel, who has been with me for my entire doctoral student career.

ACKNOWLEDGEMENTS

TABLE OF CONTENTS

LIST OF TABLES

LIST OF FIGURES

v

ABSTRACT

This study focuses on novel approaches to the modeling and construction of devices used in ion beam and vacuum systems. Turbulent computational fluid dynamics simulations were performed to model the air flow into an ion funnel system. The results of these simulations were coupled one-way with electrodynamics simulations of the fields generated by the ion funnel. Using the turbulence kinetic energy (k), a spatially varying estimation of the fluctuating component of the velocity field was calculated. These resulting simulations more accurately predicted the ion transmission through the system. Using fused deposition modeling (FDM) novel construction methods for the ion funnel and the vacuum chamber components the ion funnel system utilizes were developed. An FDM fabricated frame, in the shape of the ion funnel, was quickly and inexpensively produced. This frame supported a flexible printed circuit board that served as both the lenses of the ion funnel and power distribution circuit. The transmission of ions was as good as the traditionally constructed ion funnel. The device cost and weighed less and had lower intrinsic impedance, requiring less power to be driven. FDM was also used to produce vacuum components by post-processing using electroplating. Initial tests to determine whether electroplating would adequately produce a hermetic seal for vacuum components were performed. It was observed that thinner plated components could not withstand the stresses required from the gaskets and flanges to adequately seal, subsequently

vi

cracking. Thicker samples adequately sealed against atmosphere and maintained this seal over the entire test period. A proof of concept KF-25 full nipple was produced and processed using electroplating. The device was able to reach and ultimate pressure of 1×10^{-6} Torr, however, it was not able to reach the ultimate pressure of the chamber, which was 5×10^{-7} Torr due to the inability to be adequately cleaned of contaminant water.

CHAPTER 1: INTRODUCTION

Detection and characterization of unknown materials is a critically important task for national security and scientific discovery. Mass spectrometers, which identify the mass to charge ratio (m/q) and fragmentation patterns of ionized compounds, make detection and identification of unknown compounds possible. Moreover, atmospheric ion sources, such as electrospray ionization, allow for the detection of complex and large bio- and macromolecules. The objectives of the following study were to analyze and model existing technologies, notably the ion funnel, used in modern mass spectrometers as well as develop novel ways of constructing and housing these devices.

The structure and content of the dissertation are as follows:

- Chapter 2 discusses the relevant background information regarding the studies in the subsequent chapters and methods used therein. This chapter also briefly discusses the materials and physical apparatuses used to perform the studies.

- Chapter 3 discusses the numerical modeling of vacuum chamber containing an ion funnel that utilizes a jet disrupter and was published in the *Journal of Mass Spectrometry* in January 2015 [1]. Modeling of ion-gas interactions within mass spectrometry systems is an active field of research and is important for understanding and developing atmospheric ionization sources. In vacuum systems employing differential pumping, high velocities and turbulence exist and

1

influence then trajectories of the ions injected into the system. Computational fluid dynamics (CFD) simulations that model the gas flow and turbulence effects were coupled with an electrodynamic simulation and compared to experimental results. At the time of this writing, this paper has been cited twice [2, 3], indicating the activity within the field.

- Chapter 4 discusses a novel fabrication method for the ion funnel that utilizes flexible printed circuit board technology and fused deposition modeling (FDM or 3D printing). The objective of the study was to generate an ion funnel that would perform as well as the original design but cost far less and could be fabricated in a simpler manner. Original designs of the ion funnel used a series of stacked stainless steel ring electrodes. These rings formed the cavity through which the ions travel. Through the FDM process, which can generate complex shapes normally too costly and time consuming for traditional fabrication methods, the cavity through which the ions travel through was easily produced. The electrodes and power distribution circuit of the ion funnel could then be created using flexible PCB fabrication methods, which was inserted into the cavity, conforming to its shape. This study was published in the *Journal of Mass Spectrometry* in June 2015 [4].

- Chapter 5 extends the work of Chapter 4 by attempting to utilize FDM to produce more components of the ion funnel system. In this study, the goal was to produce a vacuum chamber with components fabricated from low-cost commercially available FDM systems. FDM-fabricated components made with systems such as the Stratasys uPrint used in this study, are very porous, readily

2

allowing air and other fluids to pass through their walls when a pressure gradient exists. Electroless and electroplating was used in order to seal the part. Other groups that have worked on sealing methods for FDM components have listed electroplating as a promising method of sealing that had yet to be explored by other researchers [5]. This chapter was submitted to the journal *Additive Manufacturing* in September 2015 and is awaiting review.

- Chapter 6 ends the document, summarizing the conclusions of the studies proposing future work.

3

CHAPTER 2: BACKGROUND

2.1 Electrospray Ionization

Electrospray ionization (ESI) is a technique used to generate gas phase macromolecules from a solution at atmospheric conditions. This process is considered a "soft" ionization technique due to the fact that many of the original structural and functional features of the molecule are preserved. The ionization technique was originally developed by Dole [6] in order separate singular polymers from solution. Fenn developed the process further and was awarded the Nobel Prize in chemistry for his
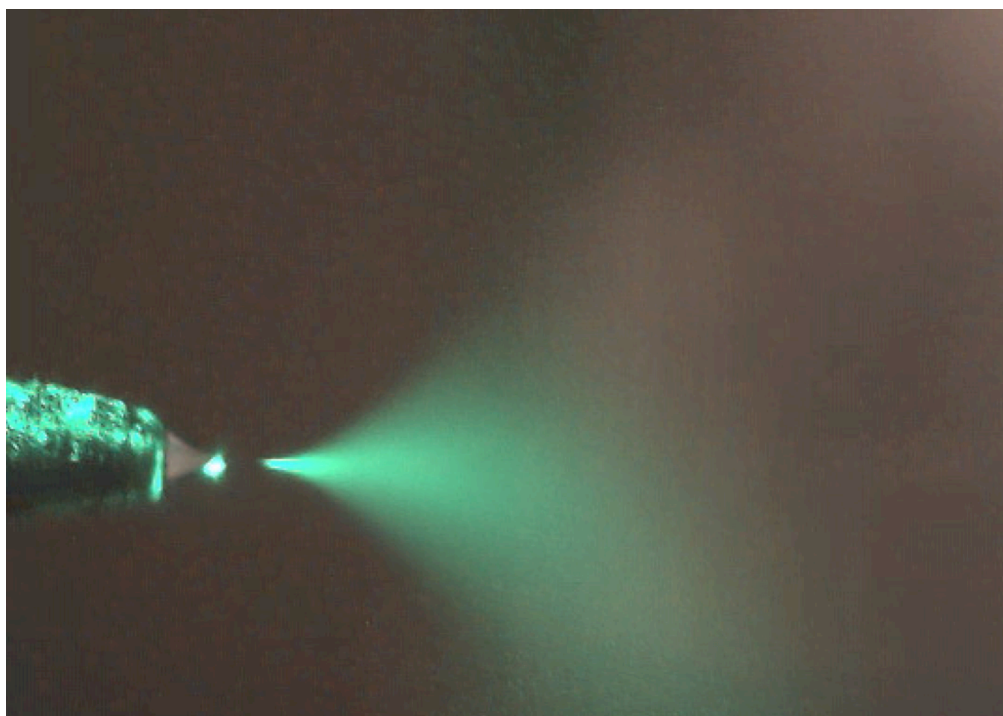
Figure 1: Image of an electrospray plume illuminated by an orthogonally oriented laser. The electrospray emitter, Taylor cone, and electrospray plume are shown.

work on electrospray mass spectrometry (ESI-MS) [7].   Other applications for electrospray are numerous including the injection of ions in to ultra-high vacuum for TEM analysis, atmospheric thin film deposition, and in vacuum thin film deposition for photoemission analysis [8-11].

Initially, droplets emitted from the electrospray capillary which are relatively large with respect to the ions, travel away from the Taylor cone. As these droplets travel
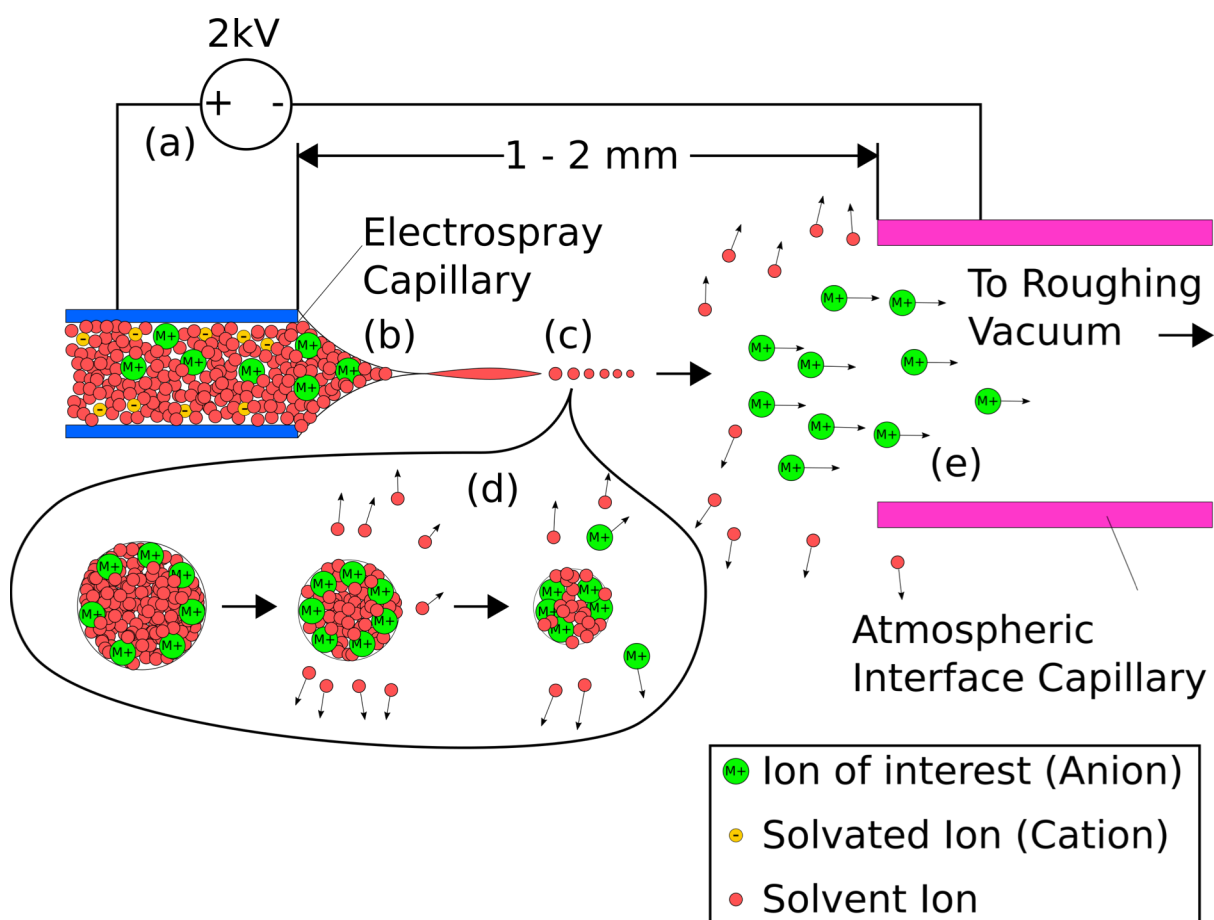
Figure 2: The electrospray process is shown schematically. A high voltage is applied between the electrospray capillary and the atmospheric interface capillary, generating a strong electric field. In the case of a positive voltage applied to the electrospray capillary, positively charged droplets will be emitted from the meniscus at the tip of the capillary. As the droplets travel through the air they evaporate and generate gas phase ions through the process of Coulomb fission.

through the air, the solvent component of the droplet begins to evaporate resulting in a reduction in volume while maintaining a constant charge. This increase in the charge density of the droplet will eventually result in instability and the subsequent breakup of droplets; a process called Coulomb fission. The maximum charge a droplet can stably contain is given by the following equation:

$$q_R = 8\pi(e_0\gamma R^3)^{1/2}$$

where q_R is the charge limit (known as the Rayleigh Limit, named after Lord Rayleigh), e_0 is the permittivity of free space, γ is the surface tension of the droplet, and R is the radius of the droplet. The process of Coulomb Fission is shown in Figure 3 from [14].
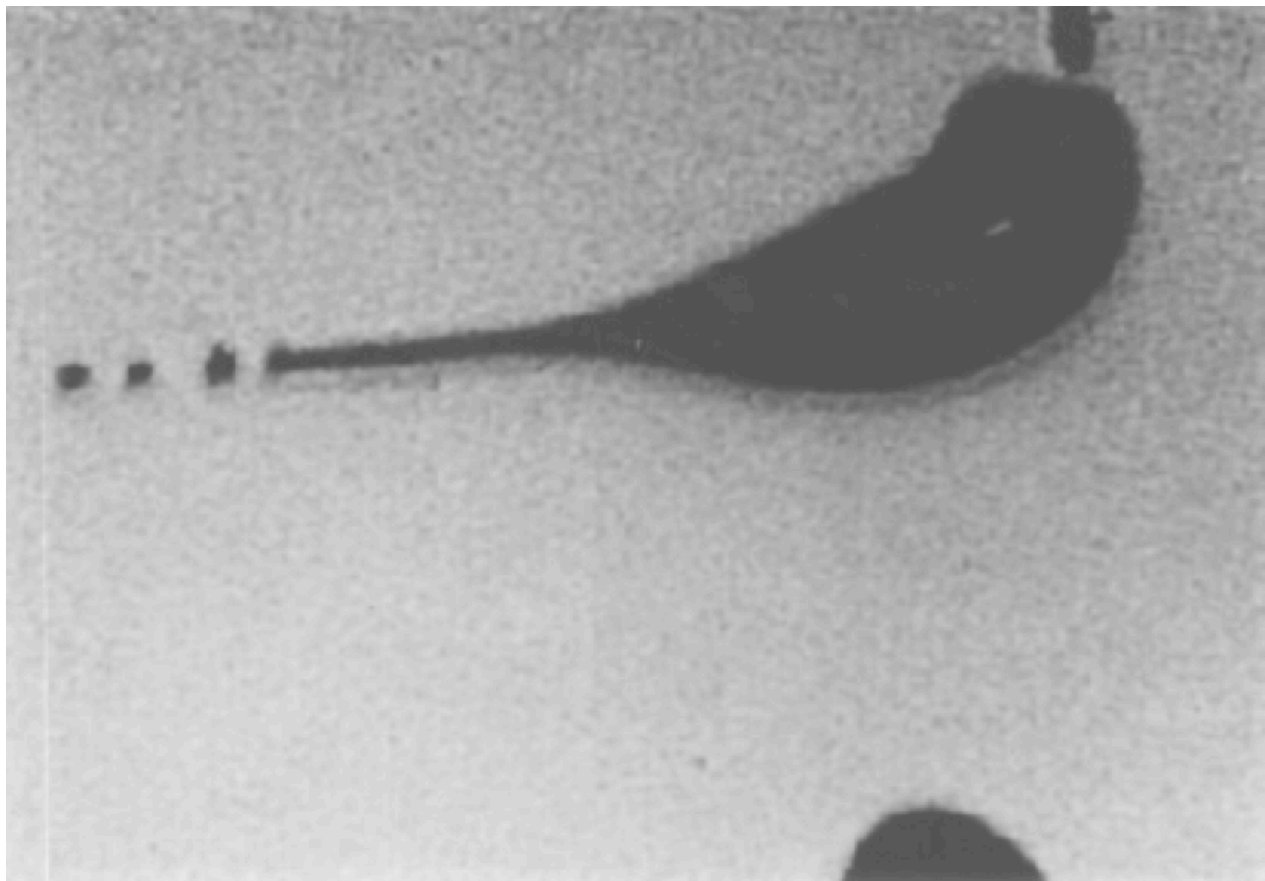
Figure 3: Photograph of a droplet undergoing Coulomb Fission. Satellite droplets can be seen ejecting from the droplet on the left side of the image. Reprinted with permission from [14].
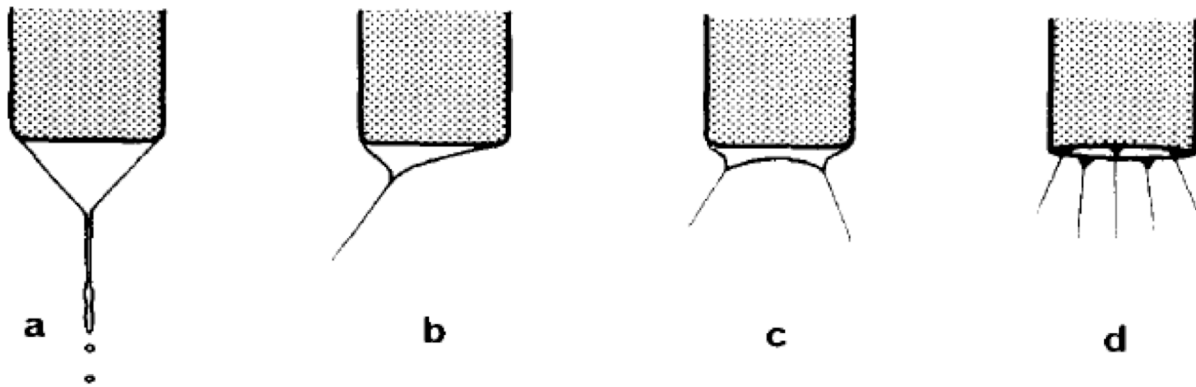
Figure 4: This image depicts the various forms of the menisci that form when an electric field is applied to the tip of a fluid-containing capillary. Panel (a) represents the most stable form, the Taylor cone. The menisci formed when the field strength is progressively increased are shown in panels (b – d). Reprinted with permission from [13].

The instability leading to Coulomb Fission is a result of the competition between the surface tension of the droplet and the charges within it. As the droplet decreases in size, its charge density increases. The charges within the droplet, being of similar polarity, will repel each other and arrange themselves on the surface of the droplet. The force between ions within the droplet becomes greater than that of the surface tension of the liquid, resulting in an ejection of smaller satellite droplets from the original parent droplet. After several iterations of Coulomb Fission gas phase ions are produced.

There are two theories on how the final Coulomb Fission steps generate the gas phase ions: the ion evaporation model (IEM) and the charged residue model (CRM). The IEM proposes that Coulomb Fission will occur several times until the size of the droplets reaches approximately 10 to 20 nm. At this point, gas phase ions will spontaneously eject from the droplets, absent of extra solvent ions. In the CRM, droplets will undergo Coulomb Fission until only single ions remain within each droplet.

Then, the remaining solvent ions within the droplet will continue to evaporate until only the ion (residue) remains [12].

The ions leaving the electrospray emitter generate an electrical current, which is proportional to the amount of charged material within the spray. For the ion funnel experiments performed in this study, the ion current is the measureable property that gives an indication of the performance of the device. The amount of current produced during electrospray can be quantified using the following equation proposed by Hendricks equation [15]

$$i_{ES} = A_H V_f^v E^\epsilon \sigma^n$$

where i_{ES} represents the electrospray current, A_H represents a constant whose value depends on the dielectric constant and the surface tension of the solvent, V_f represents the volumetric flow rate of the solution through the electrospray capillary, E represents the electric field at the tip of the Taylor Cone, and σ represents the solution conductivity.

Cloupeau systematically examined all of the major operating parameters of an electrospray apparatus and their relation to the properties of the resulting electrospray, including applied voltage, solution conductivity, solution flow rate, and electrospray emitter diameter [13]. Importantly, he noted that as flow rate and solution conductivity increase, ion current and droplet diameter increase, whereas droplet frequency decreases. The authors Fernandez de la Mora and Loscertales in a separate study demonstrated that the current generated at the electrospray emitter varied proportionally with the square root of the solution volumetric flow rate and conductivity [16].

2.2 Ion Funnel Theory

The ion funnel, developed by Smith et al. [17], is a device used to focus ion in the roughing vacuum pressure range (1 to 30 Torr). It primary use is in transporting ions generated using electrospray from atmospheric conditions into vacuum where they can subsequently be analyzed or deposited as a thin film. The ion funnel is generally the first stage in a differentially pumped system whose function is to carry material from atmosphere to high or ultra-high vacuum.
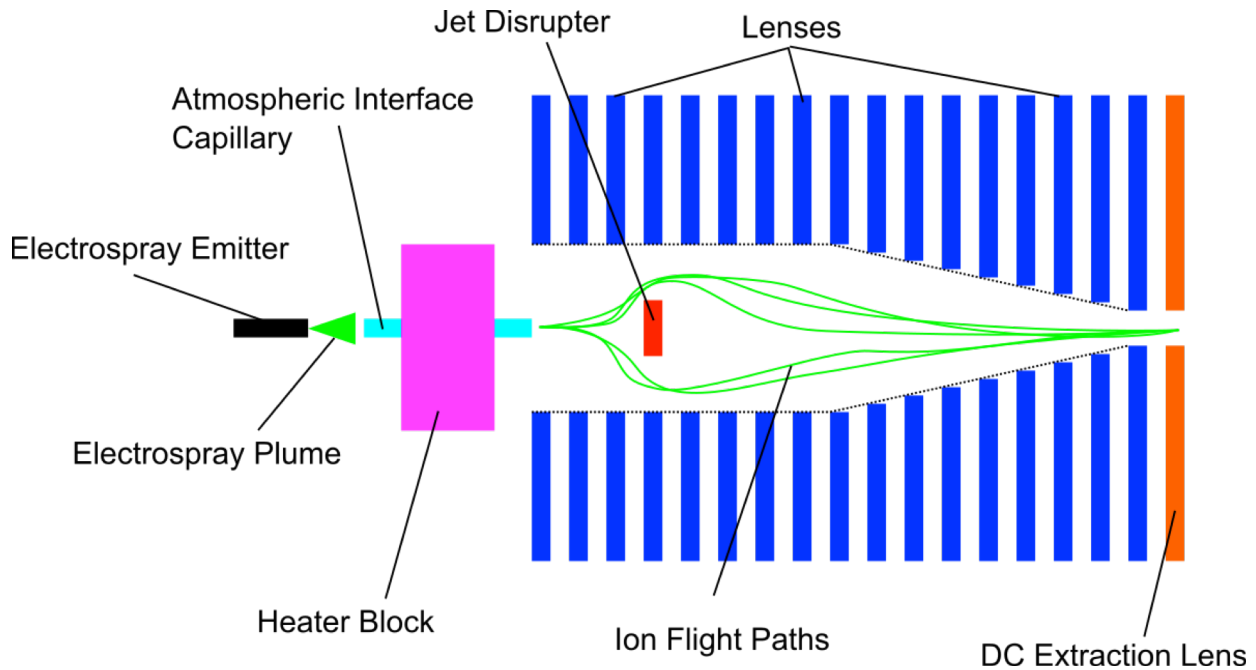
Figure 5: Schematic of electrospray generation and ion funnel. An electrospray plume, generated at atmospheric conditions is transported in to roughing vacuum via the atmospheric interface capillary. The Jet disrupter, lenses and DC extraction lenses are shown.

The device consists of a series of stacked ring electrodes. The inner diameters of these electrodes are constant for approximately the first half of the device. Subsequently, the diameters of the electrodes are decreased linearly toward the end of the funnel. The internal cavity of these electrodes creates a funnel shape. Applied to

المنارة للاستشارات

www.manaraa.com

these lenses is a combination of DC and radio frequency (RF) signals. The DC voltage applied to each lens decreases linearly from the beginning of the funnel toward the end. The RF signals applied to adjacent lenses are 180 degrees out of phase with one another. The DC voltage gradient is on the order of 10 V/cm. The RF signal generally has a peak-to-peak voltage of around 100 V_{pp} at a frequency around 700 kHz.
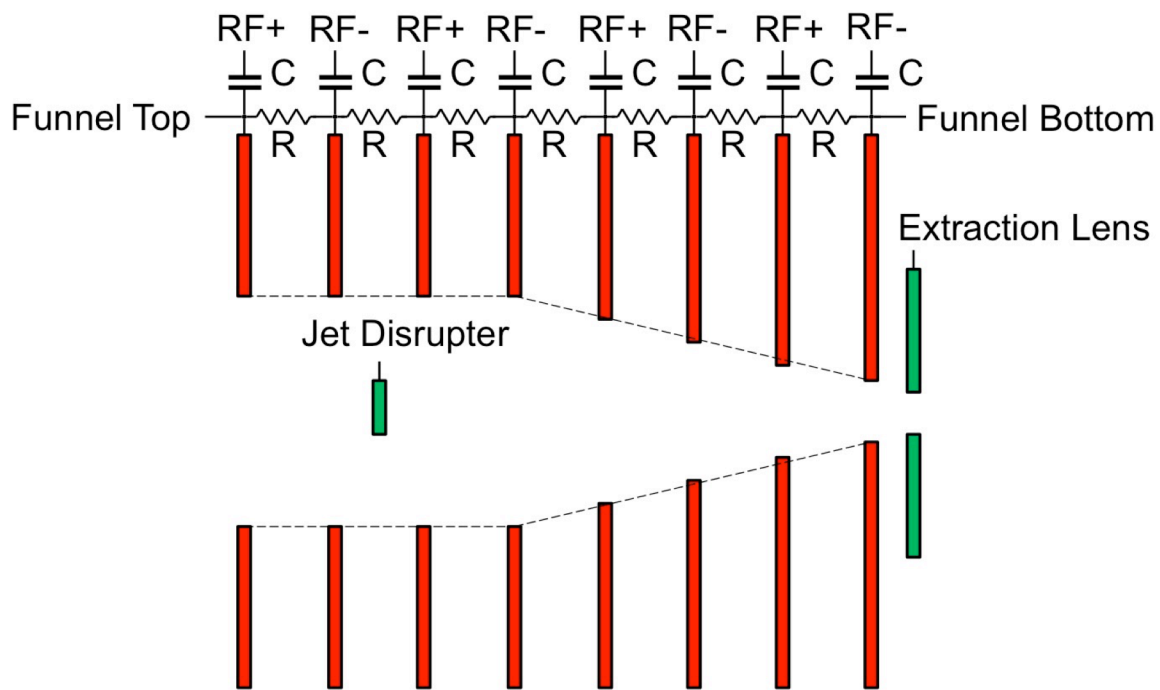
Figure 6: Electrical schematic of the ion funnel. DC signals are applied to "Funnel Top", "Funnel Bottom", "Jet Disrupter", and "Extraction Lens". The equal valued resistor chain (R) between "Funnel Top" and "Funnel Bottom" creates the voltage gradient along the axis of the funnel. The coupling capacitors (C) allow the RF signals to be superimposed on the DC gradient.

The signals applied to the ion funnel serve two purposes. First, the DC gradient serves to create an electric field that is favorable for the ions to travel along the axis of the device. In this way, ions injected in to the start of the funnel will travel down from the area of highest potential, at the start of the device, to the area of low potential at the

10

end. The linearly varying field ensures a constant axial force. Second, the applied RF signals, with adjacent lenses being of opposite polarity, results in a focusing force. Near the inner edges of the ring electrodes an extremely high pseudopotential is produced. The focusing force of this pseudopotential is directed perpendicular to the line connecting two adjacent electrodes. The magnitude of this pseudopotential quickly diminishes moving inward from the ring electrode edges, resulting in a virtually field-free region along the axis of the funnel. The combined effect of the linear voltage gradient along the funnel axis and the repulsive force of the RF signal near the electrode edges confines the ions to the axis of the funnel. As the diameter of the ring electrodes is reduced, this results in the production of a highly focused beam of ions.

The use of the extraction lens after the last of the RF lenses generates a high potential gradient that ensures that the ions are effectively removed from the lower potential end of the funnel. Because the focusing force generated by the RF signal is directed perpendicularly to the line connecting adjacent ring electrodes, in the conical section of the lower portion of the ion funnel there is a field component that directs the ions back toward the top of the funnel. The field generated by the voltage applied to the extraction lens is used to overcome this component and draw the ions out of the device.

The initial versions of the ion funnel consisted solely of the parallel plate ring electrodes [17, 18]. It was observed, however, that the high-velocity jet emitted from the atmospheric interface capillary carried with it unevaporated droplets, large mass neutral molecular species, and a high gas load that increased the pressure in subsequent systems. To alleviate this, the "jet disrupter" was introduced to newer versions of the ion funnel [19]. It serves to block any unevaporated droplets, large neutral species, and

11

high pressure gas jets that happen to enter the system. The result of this is the need for less aggressive pumping to achieve equivalent pressures in the subsequent chambers of the system. The jet disrupter is a small diameter disk that has a DC only potential applied to it. It is located in the constant diameter section of the funnel concentric to the other ring electrodes.

Typically, the device consists of 100 ring electrodes, or lenses. These are stainless steel plates with holes cut in to their centers. These lenses are connected in series with a constant valued resistor chain. Additionally, each lens will be connected to a capacitor, which serves to couple the RF signal. The DC extraction lens has a dedicated DC power supply. To create the voltage gradient, two DC voltages are applied to the first and last lenses. The difference between these voltages will establish the gradient. The capacitors serve as high-pass filters for the RF signal. In this way the RF signal can be superimposed on the DC gradient.

Initial versions of the ion funnel were constructed of stainless steel plates, as described previously. This is the type of funnel that is used for comparison purposes in this study. However, more recently, a design based on traditional PCB technology has been introduced [20]. Each of the lenses is constructed from a printed circuit board. A hole is cut in to the beard and is a metalized via in traditional PCB processing, which serves as the electrode. The hole diameter is varied and the boards stacked on top of one another to generate the funnel cavity shape. This process greatly reduces the cost, weight, and construction complexity of the ion funnel.

12

2.3 Simulation Background

Computational fluid dynamics (CFD) has become a powerful tool in modeling complex flow fields in which there is no analytical solution. The Navier-Stokes equations, which describe the motion of fluid flows, are linearized and discretized where they can then be solved over a domain. Most real-world systems have no analytical solution and must therefore employ CFD to predict the fluid flow properties of the system as well as any interaction with solid bodies. The solutions can be used as background bulk flow fields allowing for the modeling of viscous forces in the prediction of particle trajectories. In this study, the fluid flow fields around the electrospray ionization ion funnel and the capillary used to inject material into the system were modeled using CFD. The resulting flow fields were coupled in to an ion trajectory simulation software package (SIMION).

2.3.1 Fluid Flow Background

The two most important considerations when modeling the fluid flow are whether the fluid can be treated as a continuum and whether the flow is laminar or turbulent [21]. The fluid flow involved with the controlled leak of atmospheric gas into a vacuum system is quite complex. High velocities and pressure gradients, supersonic shock features, turbulent fluctuations, and rarefied flow are all encountered and must be considered when modeling the system [22].

To accurately model a system, the fluid under investigation must be treated as a continuum [23]. The Knudsen number (Kn), named after the Danish physicist Martin Knudsen, is a dimensionless parameter that defines whether the flow can be treated as a continuum or as discrete particles. It is defined as:

$$Kn = \frac{\lambda}{d}$$

where Kn is the Knudsen number, λ is the mean free path of the fluid, and d is the characteristic length of the flow. As the flow becomes mores rarefied (i.e. the mean free path of the particles increases), the Knudsen number will increase. There three flow regimes defined by the Knudsen number: viscous, transition, and free molecular flow. The bounds of the transmission regime are approximately 0.01 and 1.0, with flows less that 0.01 treated as viscous and those above 1.0 treated as free molecular. Free molecular flows are modeled using Direct Simulation Monte Carle (DSMC) in which gas-wall interactions dominate and there is little molecule-molecule interaction [24]. In this study however, all of the Knudsen numbers fall below the minimum limit for continuum flow and can be modeled using CFD.

Continuum flows are often broken in to two regimes, laminar or turbulent. Laminar flow is defined by parallel planes of flow with little mixing normal to these planes. Through a tube, such as the interface capillary of the electrospray system, a laminar flow's streamlines will all be parallel to the walls of the tube. Turbulent flows are characterized by random velocity and pressure fluctuations, resulting in unsteady vortices which are present over a wide range of length scales [25]. The Reynolds number (Re), named after British scientist Osborne Reynolds, is a dimensionless parameter used to define whether a continuum flow is in the laminar or turbulent regimes. It is defined as:

$$Re = \frac{U\rho d}{\mu}$$

14

where ρ is the fluid density, d is the characteristic length of the flow, and μ is the dynamic viscosity. The numerator of the Reynolds number represents the forces due to momentum of the system. If these are high enough, and not damped by the viscous forces (the denominator of Re), instabilities can arise resulting in a turbulent flow. Flows will have a "critical" Reynolds number, after which they become unstable and will transition from laminar to turbulent.

An estimation to determine whether the flow within the atmospheric interface capillary is turbulent can be made using the commonly accepted critical Reynolds number for flow within a smooth tube of 2100. The characteristic length used is the diameter of the electrospray atmospheric interface capillary and the density and viscosity are estimated for air at 130 ºC (the temperature of the heater block). The velocity of a flow at the critical Reynolds number for this configuration is 72 m/s. Because of the large pressure gradient that exists between atmosphere and the vacuum chamber, it is expected the flow will become choked within the capillary [26]. Choked flow occurs in an internal flow when the Mach number (the ratio of the flow velocity to the speed of sound) reaches unity. After this condition is reached, the velocity of the flow will no longer increase. The speed of sound of air at 130 ºC is 402 m/s, which is much higher than the critical velocity needed for the onset of turbulence. Therefore, it is assumed the flow within this capillary is turbulent.

Due to the large pressure ratio that exists between the atmospheric region and vacuum across the capillary, several shock features will form within the flow at and around the capillary exit. After exiting the orifice, the fluid accelerates to supersonic speeds and rapidly expands forming the shock features. These features are common of
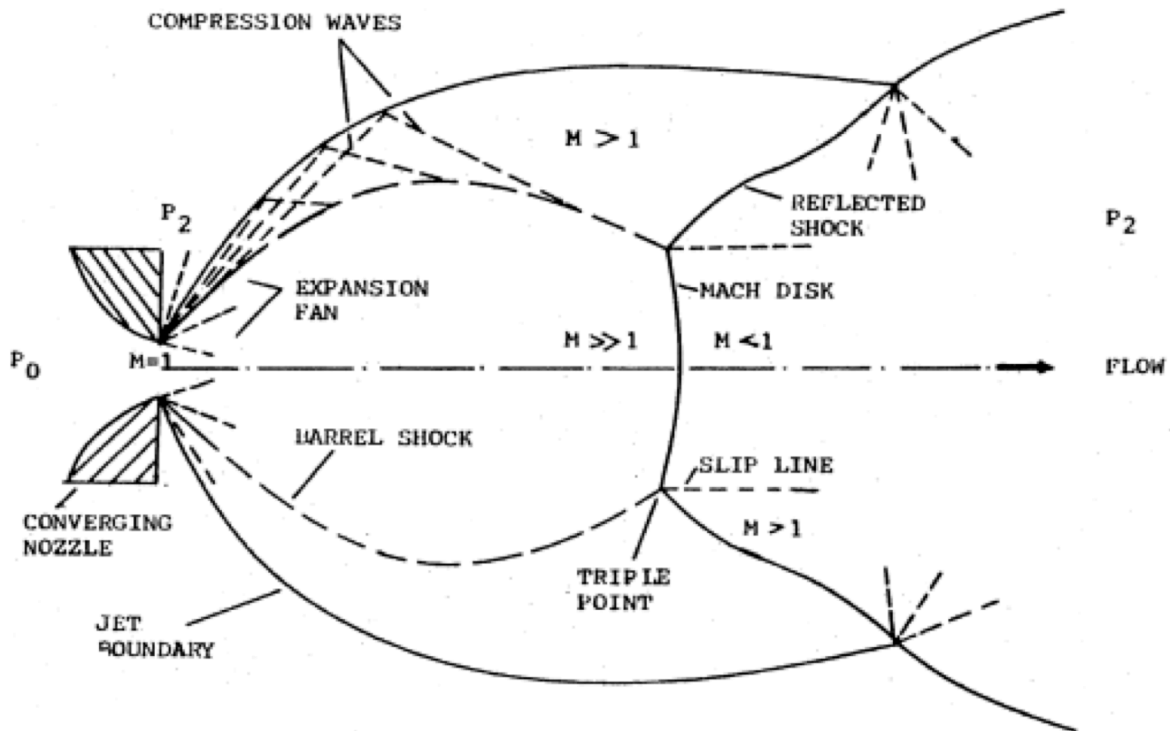
Figure 7: Schematic of a highly underexpanded jet issuing from a converging nozzle. The characteristic shock features are shown including the barrel shock and Mach disk. Reprinted with permission from [22].

underexpanded jets and include the barrel shock, Mach disk, and the "zone of silence" [22]. The barrel shock is formed after expansion waves fanning from the capillary exit contact the jet boundary and are reflected inward where they contact expansion waves issuing from the opposite side of the capillary exit. Where these waves combine, the barrel shock is formed. At a singularity, labeled in Figure 7 as the "Triple Point", the barre shock bifurcates. The resulting split generates a wave normal to the jet axis called the Mach disk. For a more complete description of the mechanisms behind the formation of the see Fenn et al., 2000 [22].

The position of the Mach disk along the jet axis has been determined experimentally and is define by the equation:

$$x_{MD} = \frac{2}{3} d \left(\frac{p_0}{p_2}\right)^{1/2}$$

where x_{MD} is the position of the Mach disk along the axis of flow, d is the diameter of the nozzle or capillary exit, p_0 is the upstream pressure, and p_2 is the ambient pressure in the region where the jet is ejecting. This equation however, assumes that the nozzle through which the fluid is flowing has an infinitesimally small length.

For an orifice of zero length, the sonic line (the location where the Mach number is unity) appears flush with the orifice exit. In practice this is not the case, as real-world nozzle and ejectors have a finite length. It has been shown though numerical and experimental investigation that the sonic line of a capillary is clamped to the edges of the internal diameter of the capillary and extends inward, forming a curved plane where the supersonic expansion occurs [27]. This is shown schematically in the bottom panel of Figure 8.

2.3.2 Fluid Flow Governing Equations and Turbulence

As mentioned previously, to model fluid flow, the Navier-Stokes equations, the governing equations describing fluid motion, are linearized and discretized over a mesh representing the fluid. In order to incorporate the turbulent effects of the flow, common in many real world applications, the process of Reynolds decomposition is performed on the velocity and pressure quantities. Reynolds decomposition involves breaking a flow quantity up in to its average value and its fluctuating value, with the condition that the

17
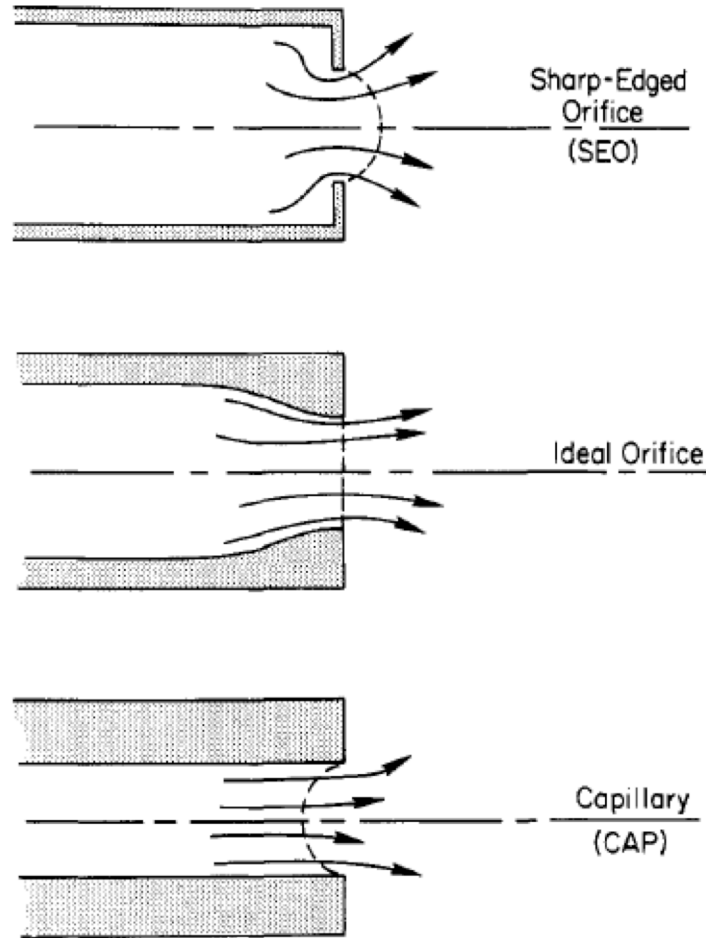
Figure 8: Locations of the sonic lines for various capillary geometries. The sonic line of the capillary (bottom panel) shows that the supersonic expansion begins interior to the orifice exit plane. Reprinted with permission from [27].

average of the fluctuating component be zero. Examples of the velocity vector and pressure scalar operated on with Reynolds decomposition is shown below:

$$\mathbf{u}(t) = \mathbf{U} + \mathbf{u}'(t)$$

$$p(t) = P + p'(t)$$

where $\mathbf{u}(t)$ and $p(t)$ are the actual velocity and pressure with resect to time, $\mathbf{U}$ and P are the mean values for all time, and $\mathbf{u}'(t)$ and $p'(t)$ are the time varying, fluctuating components whose average value is zero. Insertion of the decomposed quantities into the Navier-Stokes equations results in additional stresses within the equation, known as

18

the Reynolds stresses. These equations are known as the Reynolds Averaged Navier Stokes (RANS) equations and are shown below:

$$\frac{\partial \bar{\rho}}{\partial t} + \text{div}(\bar{\rho}\widetilde{\mathbf{U}}) = 0$$

$$\frac{\partial(\bar{\rho}\widetilde{U})}{\partial t} + \text{div}(\bar{\rho}\widetilde{U}\widetilde{\mathbf{U}}) = -\frac{\partial \bar{P}}{\partial x} + \text{div}(\mu \text{ grad } \widetilde{U}) + \left[-\frac{\partial\left(\overline{\bar{\rho}u'^2}\right)}{\partial x} - \frac{\partial(\overline{\bar{\rho}u'v'})}{\partial y} - \frac{\partial(\overline{\bar{\rho}u'w'})}{\partial z}\right] + S_{Mx}$$

$$\frac{\partial(\bar{\rho}\widetilde{V})}{\partial t} + \text{div}(\bar{\rho}\widetilde{V}\widetilde{\mathbf{U}}) = -\frac{\partial \bar{P}}{\partial y} + \text{div}(\mu \text{ grad } \widetilde{V}) + \left[-\frac{\partial(\overline{\bar{\rho}u'v'})}{\partial x} - \frac{\partial\left(\overline{\bar{\rho}v'^2}\right)}{\partial y} - \frac{\partial(\overline{\bar{\rho}v'w'})}{\partial z}\right] + S_{My}$$

$$\frac{\partial(\bar{\rho}\widetilde{W})}{\partial t} + \text{div}(\bar{\rho}\widetilde{W}\widetilde{\mathbf{U}})$$

$$= -\frac{\partial \bar{P}}{\partial z} + \text{div}(\mu \text{ grad } \widetilde{W}) + \left[-\frac{\partial(\overline{\bar{\rho}u'w'})}{\partial x} - \frac{\partial(\overline{\bar{\rho}v'w'})}{\partial y} - \frac{\partial\left(\overline{\bar{\rho}w'^2}\right)}{\partial z}\right] + S_{Mz}$$

$$\frac{\partial(\bar{\rho}\widetilde{\Phi})}{\partial t} + \text{div}(\bar{\rho}\widetilde{\Phi}\widetilde{\mathbf{U}}) = -\text{div}(\Gamma_\Phi \text{ grad } \widetilde{\Phi}) + \left[-\frac{\partial(\overline{\bar{\rho}u'\varphi'})}{\partial x} - \frac{\partial(\overline{\bar{\rho}v'\varphi'})}{\partial y} - \frac{\partial(\overline{\bar{\rho}w'\varphi})}{\partial z}\right] + S_\Phi$$

where symbols with the tilde (~) represent the density-weighted average of the flow property (i.e. $\widetilde{\mathbf{U}}$ represents the density-weighted average of the velocity vector), Φ and φ represent a generic transport scalar and specific transport scalar respectively with Γ_Φ.

To ensure closure of the RANS equations, Boussinesq approximated the Reynolds stresses with the following equations:

$$-\rho\overline{u'_i u'_j} = \mu_t \left(\frac{\partial u_i}{\partial x_j} + \frac{\partial u_j}{\partial x_i}\right) - \frac{2}{3}\rho k \delta_{ij}$$

and

$$-\rho\overline{u'_i \varphi'} = \Gamma_t \frac{\partial \Phi}{\partial x_i}$$

19

for the transport of momentum and a generic scalar respectively. In these equations k is the turbulence kinetic energy, and δ_{ij} is the Kronecker delta. The Kronecker delta is unity when i and j are equal and zero for all other cases. For the generic scalar, Γ_t is the turbulent diffusivity.

In order to calculate the Reynolds stresses using the turbulence kinetic energy and turbulent viscosity, new equations are introduced. The two most common turbulence models are the k-ε [28] and k-ω models [29]. Transport of the turbulence kinetic energy (k) and turbulence dissipation to thermal energy (ε) or specific turbulence rate of dissipation (ω) is modeled using these equations.

The turbulent viscosity is related to the turbulence dissipation and specific turbulence dissipation bye the following equations:

$$\mu_t = \rho C_\mu \frac{k^2}{\epsilon}$$

$$\mu_t = \rho \frac{k}{\omega}$$

The constant C_μ is taken as 0.09. The turbulence kinetic energy is defined as:

$$k = \tfrac{1}{2}\left(\overline{u'^2} + \overline{v'^2} + \overline{w'^2}\right)$$

The turbulence dissipation and the specific rate of dissipation are defined by the following:

$$\epsilon = 2v\overline{s'_{ij} \cdot s'_{ij}}$$

$$\omega = \frac{\epsilon}{C_\mu k}$$

Both the k-ε and k-ω models have strengths and weaknesses. The k-ω model is more accurate when predicting flows close to boundaries and low Reynolds number

flows. It is however, very sensitive to the free stream value of ω. In contrast, the k-ε model is much less sensitive to the free stream value of ε, but lacks when modeling flows close to boundaries. To compensate, Menter developed the k-ω shear stress transport model (k-ω-SST), which combines the two models using a blending function [30-32]. Compared to other commonly employed turbulence models, the k-ω-SST model provides the best match to experimental results for modeling shock features [33].

Close to boundaries, the k-ω model is utilized, while farther from boundaries the k-ε model is employed. In this way, the shortcomings of each model are mitigated by use of the opposite in the necessary regions. Reynolds stresses are calculated using the formulae for the k-ω model. The turbulence kinetic energy transport equation in the k-ω-SST model is:

$$\frac{\partial(\rho k)}{\partial t} + \text{div}(\rho k \mathbf{U}) = \tilde{P}_k - \text{div}[(\mu + \sigma_k \mu_t)\text{grad}(k)] - \beta^* \rho k \omega$$

where

$$\tilde{P}_k = \min(P_k, 10\beta^* \rho k \omega)$$

$$P_k = 2\mu_t S_{ij} S_{ij} - \frac{2}{3} \rho k \frac{\partial u_i}{\partial x_j} \delta_{ij}$$

$$S_{ij} = \frac{1}{2}\left(\frac{\partial u_i}{\partial x_j} + \frac{\partial u_j}{\partial x_i}\right)$$

The constant β^* is equal to C_μ used previously, whose value is 0.09. The turbulent eddy viscosity is calculated by:

$$\mu_t = \frac{\rho a_1 k}{\max(a_1 \omega, \Omega F_2)}$$

$$F_2 = \tanh\left\{\left[\max\left(2\frac{\sqrt{k}}{\beta^* \omega y}, \frac{500\nu}{y^2 \omega}\right)\right]^2\right\}$$

21

$$\Omega = \sqrt{2W_{ij}W_{ij}}$$

$$W_{ij} = \frac{1}{2}\left(\frac{\partial u_i}{\partial x_j} - \frac{\partial u_j}{\partial x_i}\right)$$

For the specific rate of dissipation, several blending functions are used to modify the constants based on proximity to boundaries. The transport equation is:

$$\frac{\partial(\rho\omega)}{\partial t} + \text{div}(\rho\omega\mathbf{U}) = \alpha\rho S^2 - \beta\rho\omega^2 + \text{div}\left[(\mu + \sigma_{\omega,1}\mu_t)\text{grad}(\omega)\right] + 2(1 - F_1)\rho\sigma_{\omega,2}\frac{1}{\omega}\frac{\partial k}{\partial x_i}\frac{\partial \omega}{\partial x_i}$$

where the blending function employed is:

$$F_1 = \tanh\left\{\left\{min\left[max\left(\frac{\sqrt{k}}{\beta^*\omega y},\frac{500v}{y^2\omega}\right),\frac{4\rho\sigma_{\omega,2}k}{CD_{k\omega}y^2}\right]\right\}^4\right\}$$

and

$$CD_{k\omega} = max\left(2\rho\sigma_{\omega,2}\frac{1}{\omega}\frac{dk}{dx_i}\frac{d\omega}{dx_i},10^{-10}\right)$$

$$S^2 = 2S_{ij}S_{ij}$$

The value y in the blending function is the distance from the nearest boundary. For the constants α, β, σ_k, and σ_w, the following blending function is utilized:

$$C = C_1F_1 + C_2(1 - F_1)$$

where the near (C_1) and far-field (C_2) values of the constants are given Table 1

2.3.3 OpenFOAM and rhoCentralFoam

To model the gas dynamics within the system, the open source CFD package OpenFOAM (Open Source Field Operation and Manipulation) was used. OpenFOAM is a collection of C++ libraries and compiled programs, which allow users to easily model continuum mechanics systems. The package includes several precompiled mesh

Table 1: Near- and Far-field values of constants for transport equations in the k- ω -SST model.

	α	β	σ_k	σ_ω
Near wall (C_1)	5/9	3/40	0.85	0.5
Far-field (C_2)	0.44	0.0828	1	0.856

creation and manipulation utilities, data manipulation utilities, and solvers [34]. In addition, a large online user community actively contributes and develops the software.

OpenFOAM utilizes the finite volume method to discretize the partial differential equations that govern the continuum mechanics problems it solves. The finite volume method involves breaking the domain under investigation in to individual volumes (cells). These cells are centered on nodes, points at which the properties of the fluid will be determined. To calculate these properties, the governing partial differential equations of the system are linearized over the cell domain. Divergence and gradient terms can be calculated by transforming them into integrals over the face of each cell, which allow for the calculation of flux across these faces (Gauss's divergence theorem). Properties at the nodes are determined by interpolation using various schemes.

The fluid flow simulations in this study were performed using the transient, transonic, density based solver "rhoCentralFoam", included with the OpenFOAM package. This solver was developed by Greenshields et al. [35]. To calculate the fluxes across the cell faces, rhoCentralFoam utilizes the central upwind interpolation methods of Kurganov et al. [36, 37]. Additionally, rhoCentralFoam employs total variation diminishing (TVD) flux limiters, such as the van Leer limiter used in this study [38]. The solver uses the implicit Euler discretization scheme. The solver's algorithm works by first predicting the inviscid flow properties then substituting these into the

23

viscous equations and correcting them. For a complete description of the algorithm see [35]. The solver was tested against several benchmark tests [39, 40]. The results of the simulation of an underexpanded jet versus the benchmark test case are shown in Figure 9.

2.3.4 SIMION and the Hard Sphere Model

SIMION is "is a software package primarily used to calculate electric fields and the trajectories of charged particles in those fields when given a configuration of electrodes with voltages and particle initial conditions, including optional RF (quasistatic), magnetic field, and collisional effects" [41]. SIMION has applications in modeling electrostatic and magnetic lenses, as well as more complex systems such as
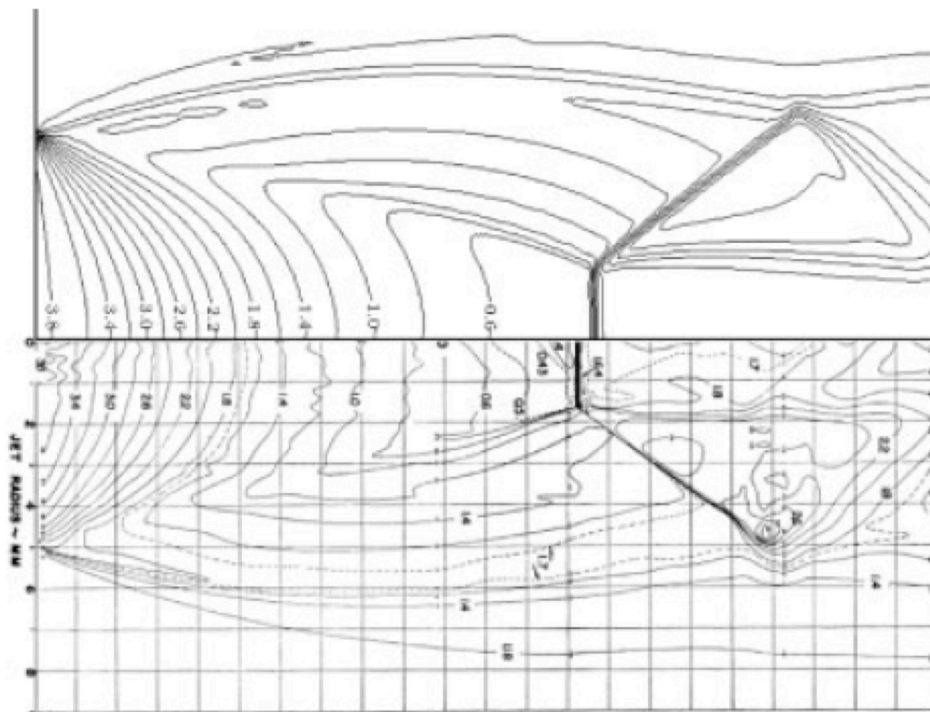
Figure 9: Comparison between rhoCentralFoam solution of underexpanded test case (top) versus benchmark test (bottom) performed in [40]. Image reprinted with permission from [35].

24

ion funnels, quadrupoles, time-of-flight (TOF), ion cyclotron resonance cells, and other ion optics applications [42]. Many major ion optics and mass spectrometry companies in the industry use the software. The software has been used with success to simulation ion funnels for research [17, 43-45].

SIMION geometries are defined in a square Cartesian grid and can be either two dimensional, axisymmetric, or fully three-dimensional. Support for mirrored geometries is also available. The Laplace equation (in addition to other partial differential equations) is solved using the finite difference method and other ordinary differential equations solved using Runge-Kutta. The software is a full FDM package that allows for the definition of the geometry, boundary conditions, initial conditions, and solution parameters without the need for third party software.

Support for ion-gas interactions is included as the collision model "hs1". This model assumes that both the ions and gas are hard spheres that interact solely though elastic collisions. The coupling is one-way (i.e. the background gas is unaffected by the ion-gas interactions). The velocity due to kinetic energy of the background gas through which the ions are travelling follows the Maxwell-Boltzmann distribution. The mean relative speed between the ion and background gas ($\bar{c}$) is computed and used to calculate the effective mean free path (λ_{eff}) of the ion-background gas couple using the equation:

$$\lambda_{eff} = \frac{kT|\mathbf{v}_{ion}|}{\bar{c}P\sigma}$$

where k is the Boltzmann constant, $\mathbf{v}_{ion}$ is the velocity of the ion, P is the pressure, and σ is the collision cross sectional area of the ion. Based on the effective mean free path, the probability, P, of a collision is estimated using the equation:

$$P(\lambda_{eff}) = 1 - e^{-\frac{|\mathbf{v}_{ion}|\Delta t}{\lambda_{eff}}}$$

where Δt is the time-step of the ion. A random number between zero and one is chosen and if it is less than the probability estimated previously, a collision is simulated.
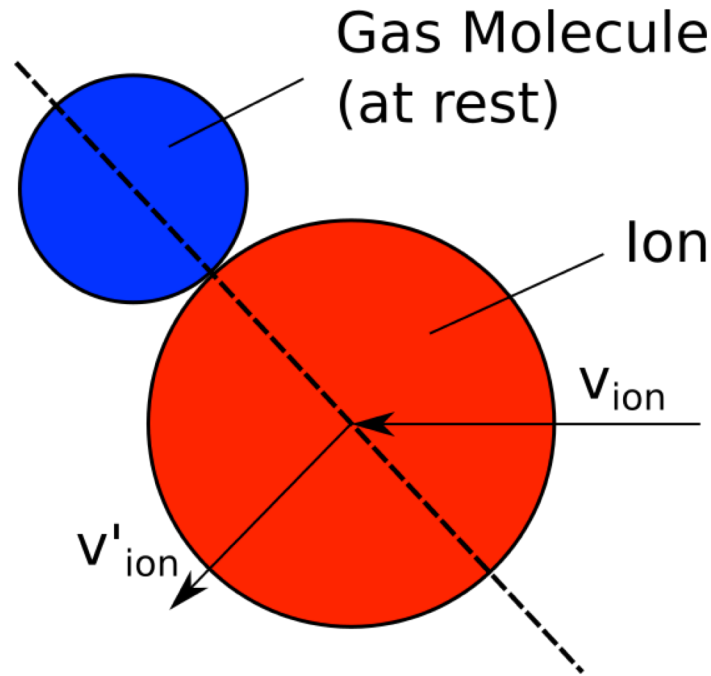
Figure 10: Schematic diagram of an ion and gas molecule interacting as modeled with the hard sphere model.

To simulate a collision, a reference frame is chosen in which the gas molecule is at rest, as shown in Figure 10. Transformation of the velocity vectors into polar coordinates allows this problem, initially in three dimensions, to be converted to a two dimensional problem. This can be performed due to the fact that the ion was in some two-dimensional plane immediately before and immediately after the collision. During the collision modeling the velocity is attenuated due to the elastic collision, which accurately simulates kinetic cooling. After the post-collision velocities are computed,

the velocity vectors are transformed back to Cartesian coordinates and the reference frame adjusted to the original.

2.4 Fused Deposition Modeling Background

Additive manufacturing (AM) includes many techniques though which parts are produced through the successive addition of material in there dimensions to generate a functional part. AM techniques are in contrast to traditional manufacturing techniques, such as machining, which remove material from the bulk to produce a final component. The main advantage of AM processes is the ability to create complex, organic shapes, often too difficult to be produced with traditional machining methods, with little need for process planning. Gibson refers to this as "complexity for free" indicating that whether one is producing a simple cube or complex model of a human organ, the processing requires the same effort [46].

Fused deposition modeling (FDM) is an AM technique in which components are fabricated by extruding a material, generally a thermoplastic polymer, in an x-y plane, producing cross-sections of a component. Successive layers are deposited one on top of another in the z- direction, producing a three dimensional component. The material, often in the form of a solid filament, is fed into a nozzle through a pinch roller system. The nozzle is heated to a temperature above the polymer's glass transition temperature, rendering it molten. As the pinch roller feeds successive filament into the nozzle, a pressure build-up forces the molten thermoplastic out of the extruder as a thin string, often referred to as a "road". Using computer control, the nozzle is traversed in the x-y plane in the path representing a cross section of the part. The molten material physically binds (fuses) to either the heated bed or a previously extruded layer, thus

27

forming a solid, albeit porous, component. After the completion of a cross section, the distance between the nozzle and layer is indexed in the z-direction and the process repeated to generate the next cross-section. This process is shown schematically in Figure 11.
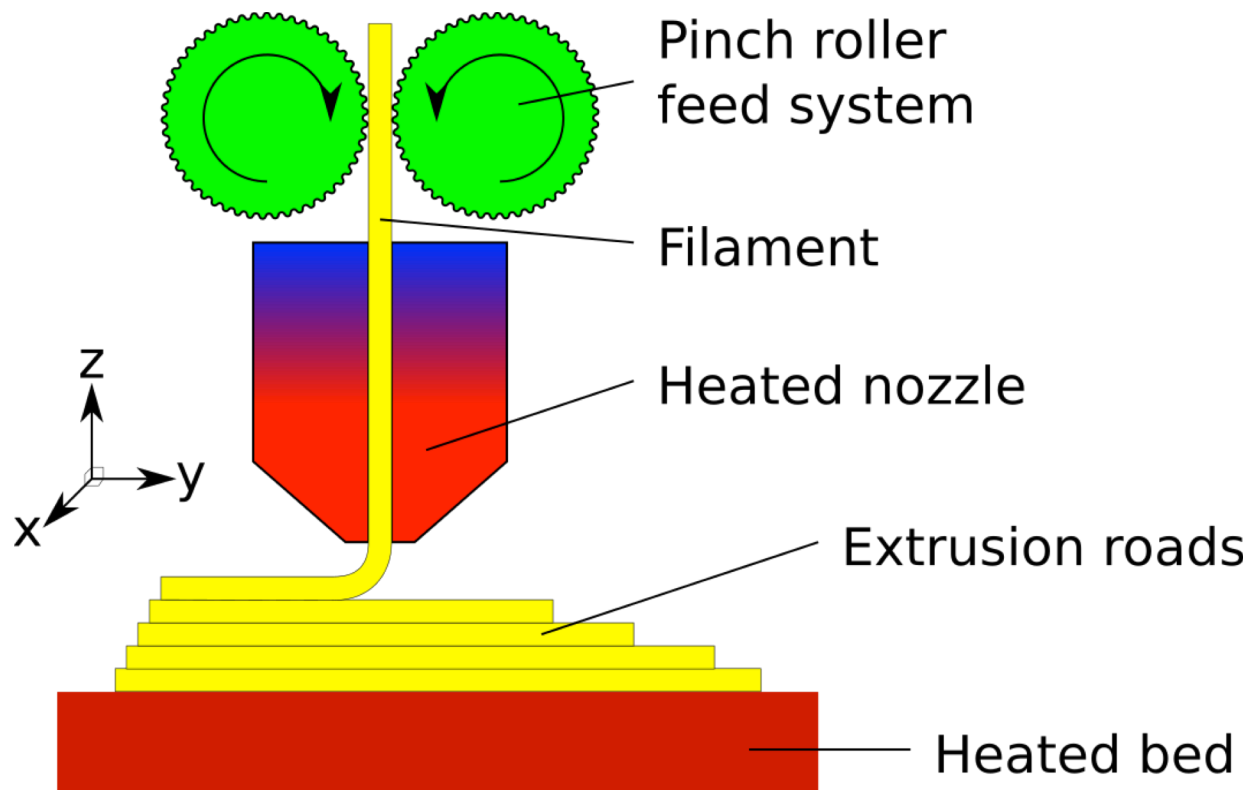
Figure 11: Schematic diagram of the FDM process. The pinch roller feed system forces the filament through the heated nozzle where it is extruded onto the bed or previously deposited layer. This extrusion is done layer-by-layer, generating a solid part.

The process of producing a part by FDM involves: 1) generating a three dimensional representation of the object using a CAD software package, 2) converting the CAD drawing into the standard stereolithography (STL) file format used by most additive manufacturing machines, 3) generating the tool path for the device using specialized software that slices the three dimensional STL file in to two dimensional cross sections based on specified build parameters, 4) extrusion of the thermoplastic

material to generate the three dimensional part, 5) removal of the part from the build plate, 6) post-processing the part to achieve desired surface finish or mechanical properties.

Several commercial and open source FDM machines exist on the market today, where the process is often referred to as 3D printing. The market leader in 3D printers is Stratasys (Eden Prairie, Minnesota) and holds the original patent for FDM [47]. Stratasys acquired Makerbot, the first 3D printer aimed at a household consumer market, in 2013 [48]. Affordable, open source 3D printer designs have become increasingly popular, many of which are based on the "RepRap" design [49].

The mechanical properties of the parts produced using FDM can vary greatly due to the anisotropy inherent in the fabrication process. Variation in part orientation [50] and build parameters [51] greatly affects these properties. Ahn et al. examined the build parameters that affected the tensile strength of parts. The parameters investigated were bead (i.e. road) width, air gap (distance between successive layers), build temperature, and raster orientation. Of these parameters, raster orientation was found to have the most significant affect on tensile strength. Highest strength was achieved when the air gap was negative (resulting in highly fused layers) and the raster angle was parallel to the tensile direction. Bead width and model temperature had a negligible affect on the strength [52]. Additionally, parts printed with the planar layers parallel to the direction of force had a compressive strength of 41.26 MPa. When the planar layers were printed perpendicular to the compressive force direction, the compressive strength was reduced to 36.97 MPa [53].

Bellini et al. examined the tensile strength of parts produced using FDM as well as the individual filament (pre extrusion) and extrusion road. They found that the strength difference between the filament and extrusion road varied negligibly, however the strain experienced by an extruded road was one third of that of the unextruded filament. This result is due to the orientation imposed on the polymer chains in the molten state as they are extruded through the nozzle, rendering the polymer more brittle [54].

FDM part use in fluid applications has been limited due to the porous nature of the components produced [55]. Although a strong mechanical bond exists between adjacent roads, fusion is not perfect, resulting in voids as shown in Figure 12. Chemical processing [56, 57], painting with epoxies and coatings [5], and epoxy injection [58] have all demonstrated that post-processing of FDM-fabricated components can be
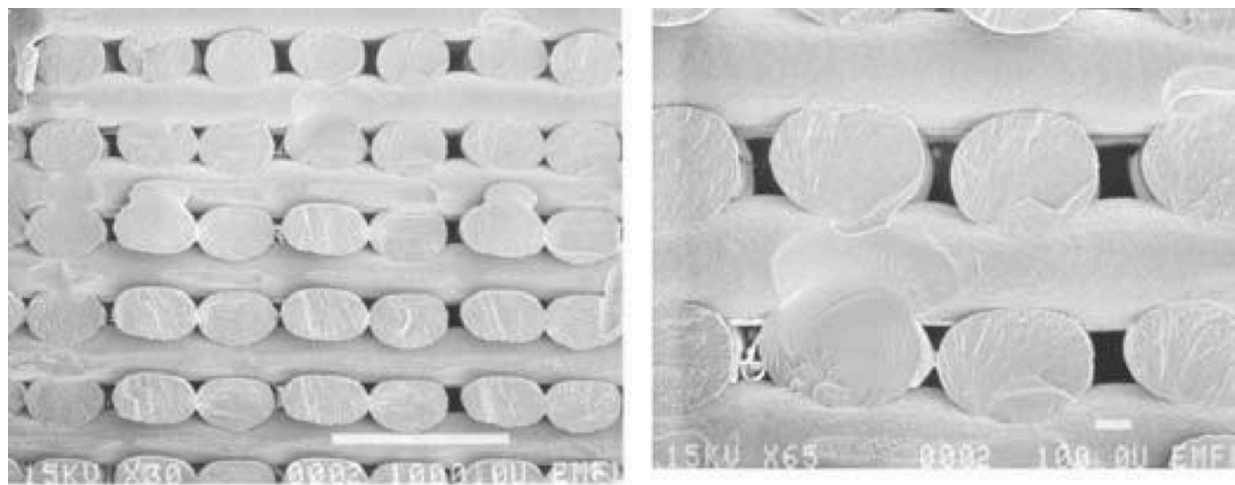
(a) Overview   (b) Close up

Figure 12: Cross-sectional image of an FDM-fabricated component. Note the voids between adjacent extrusion roads in the image. Reprinted with permission from [54].

effectively sealed. In addition, these processes generally improve the strength and surface finish of the final product.

During this study, all parts were produced on the Stratasys uPrint SE Plus. This printer can print in eight colors with support material. Its build area is 203 x 203 x 152 mm and has a layer height of 0.254 mm or 0.330 mm. The support material is SR-30 and can be dissolved in Stratays's proprietary WaveWash Support cleaning system [59].

2.5 Plating Background

Electroplating is an electrochemical process that produces a metal film on the surface of a conductive work piece or a non-conductive work piece after being rendered conductive. This work piece acts as an electrode (cathode) and is immersed in an electrolyte solution containing the ions of the metal to be deposited. An additional electrode (anode), generally made of the same metal as the ions in solution, is placed in the electrolyte solution. Passing a current between the positively charged anode and the negatively charged cathode through the electrolyte solution results in the deposition of a solid metal film on the surface of the cathode. Reduction of the metal ions in solution at the cathode forms the plate. Oxidation of the solid metal on the surface of the anode replenishes the ions in solution [60]. The growth mechanism of a continuous film results from either a layer growth or nucleation/coalescence growth pattern [61, 62]. A typical electroplating tank apparatus is shown schematically in Figure 13.

The final thickness of the deposited metal is a function of the deposition time, current of the electrochemical process, and the electrochemical equivalent (Z) of the

metal ion. The electrochemical equivalent of the metal ion is a measure of the amount of material deposited per Coulomb of charge. It is calculated by:

$$Z(M^{n+}) = \frac{A_M}{nF}$$

where A_m is the atomic weight of metal M, n is the valency of the metal ion, and F is Faraday's constant (equal to 96,487 Coulombs, equivalent to the charge of one mole of electrons). For example, electrochemical equivalent of the Cu^{2+} ion is 0.3293 g/C. The amount of material deposited, in grams, can therefore be calculated using the electrochemical equivalent using the function:

$$w = ZQ = ZIt$$

where I is the current of the process and t is the total deposition time. Assuming a
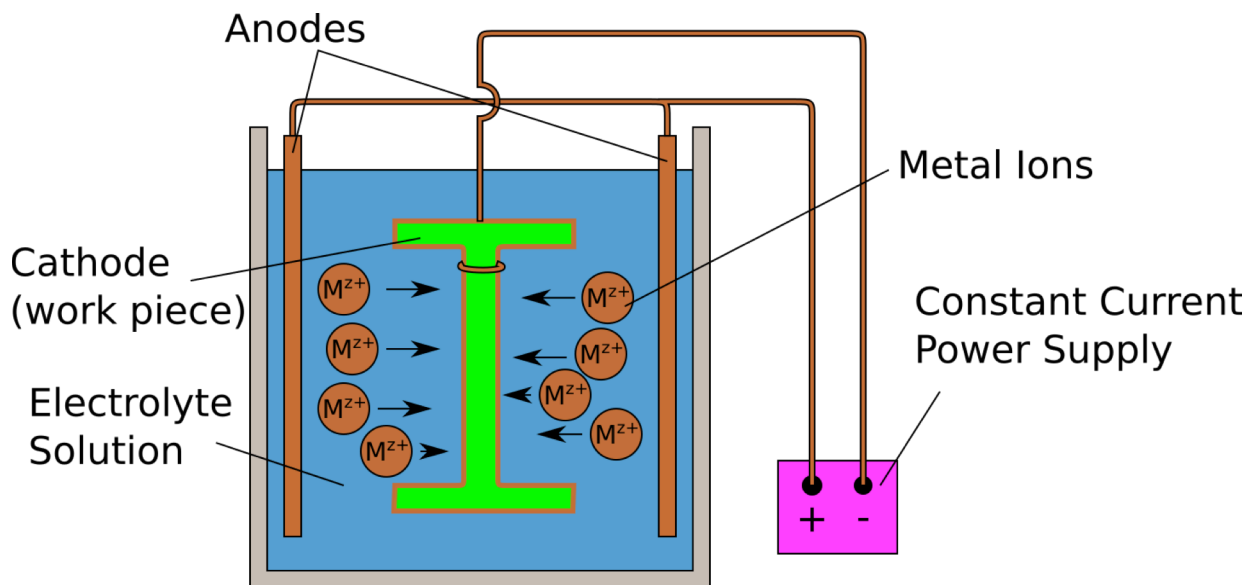
Figure 13: Schematic overview of an electroplating setup. A constant current power supply supplies the current that passes through the anodes to the cathode through the electrolyte solution.

uniform thickness (h) and constant density of material (ρ) over a part with a surface area (A), the thickness of a deposition can be estimated with:

$$h = \frac{w}{A\rho}$$

2.5.1 Electroplating Bath Formulations

Copper is one of the most commonly plated metals due to its cost and relative availability. Some of its more common uses are as interconnects in the semiconductor industry, plating vias in printed circuit boards, and build-up layers to level the surfaces of engineering components. It is also very commonly used as an under layer for plating on plastic due to its ability to withstand large changes in thermal expansion [60]. Additionally, copper exhibits good throwing power, which is the ability to uniformly plate areas irrespective of their proximity to an anode. Practically, this allows for the plating of irregularly shaped work pieces. Although a myriad of ion systems exist to perform copper electrodeposition, commercially used formulations of plating baths include alkaline cyanide, pyrophosphate complex, acid sulfate, and acid fluoroborate ion systems. The system used in this study is the acid copper sulfate system. The formulations for both conventional and high-throw acid copper sulfate plating baths are shown in Table 2. In this study a conventional throw solution of the acid copper sulfate was used.

Due to its susceptibility to corrosion, copper is often plated with other metals after its use as a build-up material. The process of electrodeposition of nickel is similar to that of copper, both of which employ soluble anodes, which replenish metal ions in solution. The bath formulation used in this study is the Watt's bath. It contains two nickel ion sources, Nickel Sulfate, $NiSO4 \cdot 6H_2O$ and Nickel Chloride, $NiCl_2 \cdot 6H_2O$, at

33

Table 2: Typical concentrations of components in an acid copper sulfate plating bath. The formulations for conventional and high-throw solutions are shown. Data from [60].

Copper sulfate solutions	Conventional Solutions	High Throw Solutions
Copper Sulfate, $CuSO_4 \cdot 5H_2O$, g/L	200 – 250	60 – 100
Sulfuric Acid, H_2SO_4, g/L	45 – 90	180 – 270
Chloride, Cl^-, mg/mL	–	50 – 100

concentrations of 225 – 400 and 30 – 40 g/L respectively. Additionally, the Watt's formulation contains a small amount (30 – 45 g/L) of boric acid, H_2BO_3.

2.5.2 Tollen's Reagent and Plating on Plastics

As mentioned previously, electroplating must be performed on a conductive component in order to provide the electrons for reduction at the cathode. Several methods for producing a conductive surface exist including painting with conductive paint, graphitizing, and electroless deposition of metals. For this study the electroless deposition of silver via Tollen's reagent was chosen to render the non-conductive work pieces conductive. The use of silver films produced in this was has been shown to be effective in producing a conductive substrate on to which electroplating can be performed [60, 63]. Tollen's reagent is an organic chemistry reagent that is used to qualitatively determine the presence of aldehydes [64] but has also been used to generate silvering for mirrors [65]. The reaction of Tollen's reagent is given by:

$$(C_5H_{11}O_5)CHO + 2[Ag(NH_3)_2]^+ + OH^- \rightarrow (C_5H_{11}O_5)COO^- + 2NH_4^+ + 2NH_3 + 2Ag^0$$
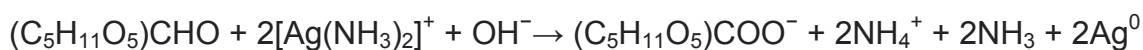
The silver ammonium complex $[Ag(NH_3)_2]^+$ is mixed with glucose in a highly alkaline environment. The resulting reaction produces solid silver, generating a highly conductive thin film on all surfaces within the reaction vessel.

Although electroless plating preparations, such as Tollen's reagent, readily deposit on polymeric materials (plastics), low surface roughness severely impedes the adhesion of these films. Because of this, special surface preparation methods must be performed to ensure adequate adhesion of the resultant films. The first process is
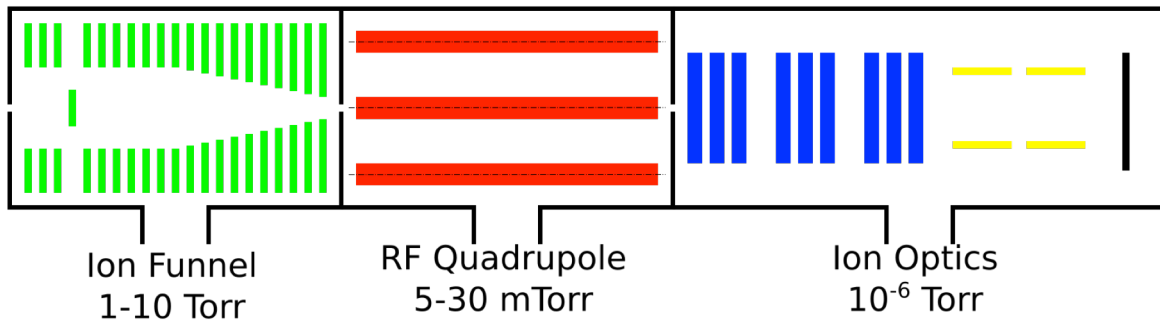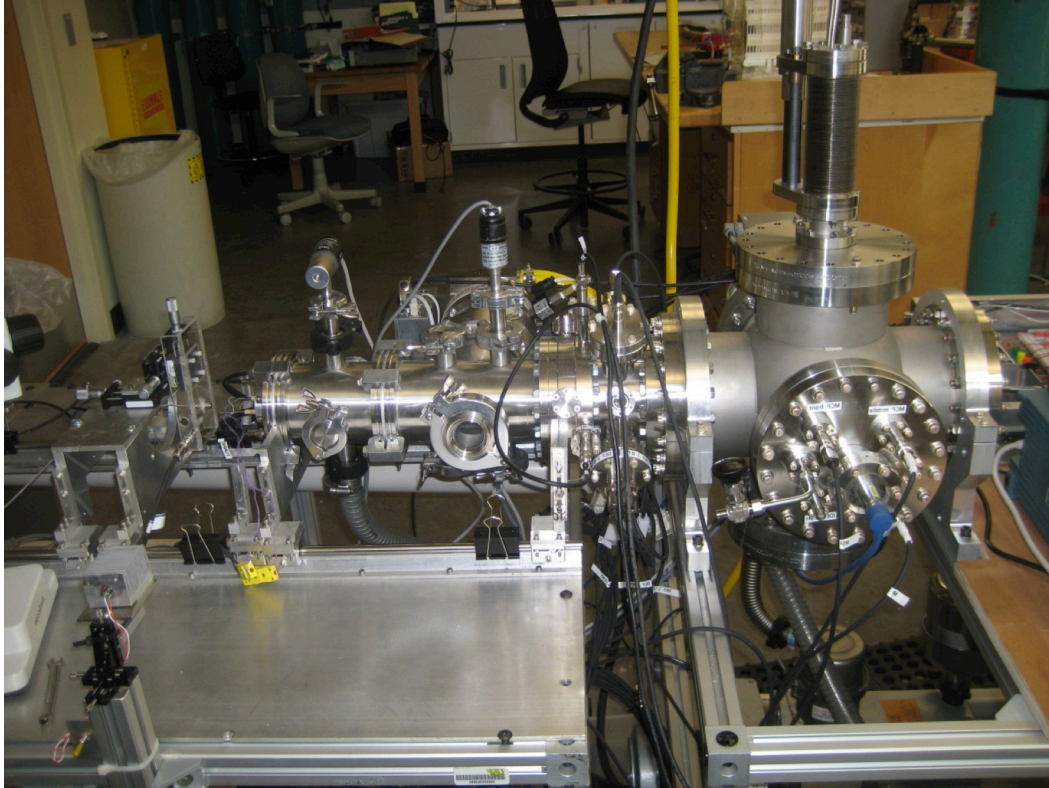
Figure 14: Image of the macromolecular patterning system. Ion injection occurs on the left with three subsequent differential pumping stages. The system is shown schematically in the bottom panel.

etching. The polymeric part is soaked in a chromic acid solution (a mixture of CrO_3 and H_2SO_4). The hexavalent chromium (Cr^{6+}) acts as a strong oxidizing agent. For example, when plating on the ter-polymer ABS (acrylonitrile-butadiene-styren), the chromium with selectively attack the butadiene phase of the solid [66]. The result is that a micro-pitted surface is produced which increases the number of locations to generate a mechanical bond with the substrate. Extra care must be taken when using the chromic acid solution as any residual hexavalent chromium remaining on the surface will severely hinder the subsequent electroless deposition. The use of special reducing agents, such as sodium bisulfite ($NaHSO_3$), reduces the hexavalent chromium to its less reactive trivalent form.

In addition to etching, a sensitizing binding agent is used to improve the adhesion of the electrolessly deposited film. For Tollen's reagent, the compound stannous chloride ($SnCl_2$) is used. Prior to silver deposition, the work piece is soaked in a solution of stannous chloride and hydrochloric acid and then rinsed. Ions of Sn^{2+} remain on the surface and act as a binding agent for the silver. Using this process, care must be taken to ensure that the work piece remains wet prior to silver deposition [67].

2.6 Physical Apparatus and Materials

2.6.1 Ion Funnel Experiments

The ion funnels used in this study were part of a larger differential vacuum pumping system. This system was originally designed as a macromolecular patterning device wherein large bio- or macromolecules generated via electrospray could be patterned at a small scale under high vacuum. The overall system as well as schematic model is shown in Figure 14. The first stage, and focus of Chapters 3 and 4, contains

the ion funnel. This chamber was generally held at a pressure of around 1 to 10 Torr using an oil sealed rotary vane roughing pump. The subsequent chamber contains an RF quadrupole at a pressure of approximately 5 to 30 mTorr. This chamber utilizes collisional cooling to homogenize the kinetic energy of the particles prior to entering the final chamber as well as serve as an intermediate pumping stage between the first and third chambers. The final chamber contains the ion optics, raster plates, and substrate. The ion optics shaped the ion beam as it enters the chamber. The raster plates deflect
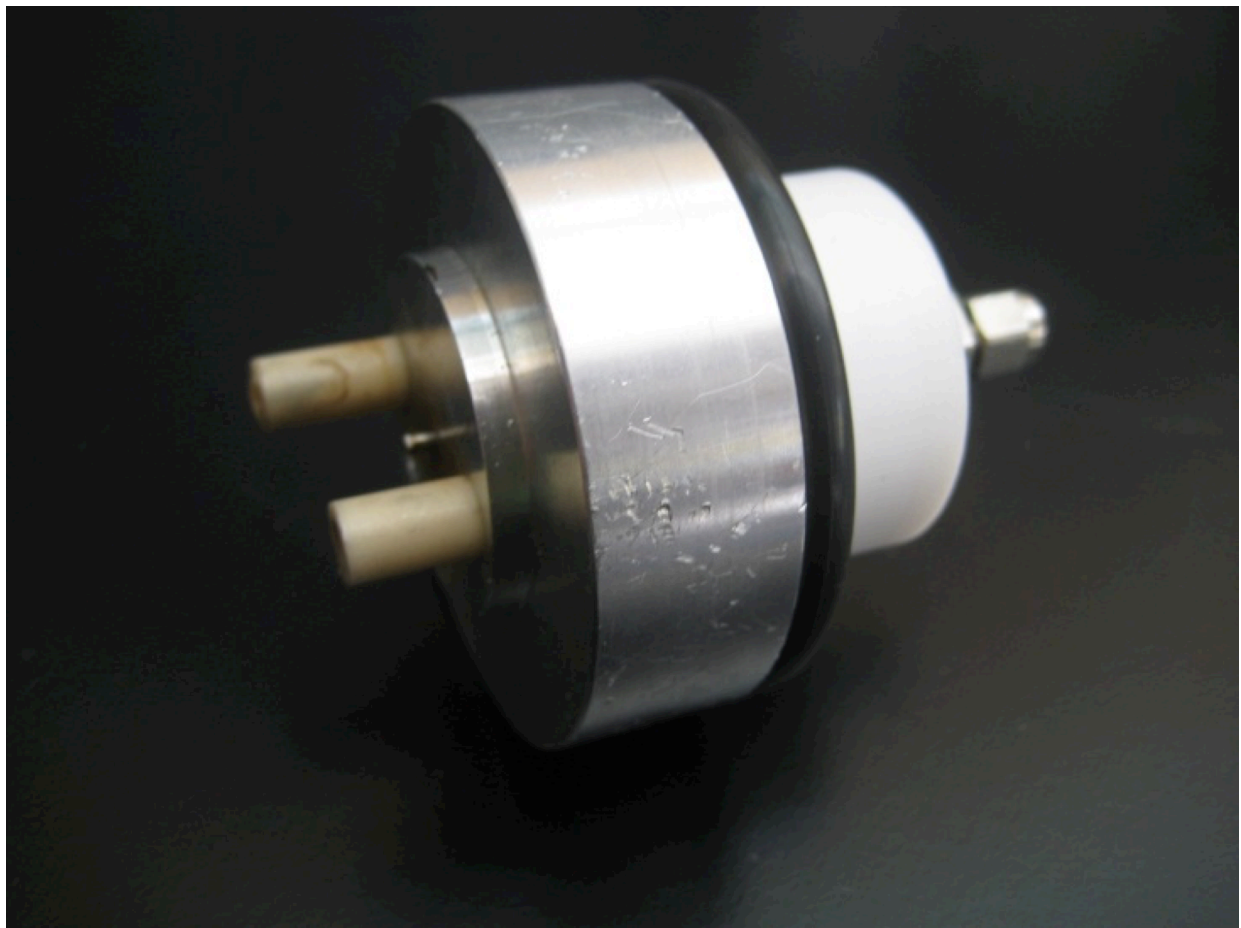
Figure 15: Image of the heater block and atmospheric interface capillary. Ions enter from atmospheric conditions into the capillary on the left and are injected into the vacuum system out of the right.

the beam so that it can be directed in a controlled manner toward the substrate for patterning. The RF quardupole chamber and ion optics chamber were each pumped by 230 liters per second turbomolecular pumps backed by oil sealed rotary vane mechanical pumps.

To generate the electrospray, a custom OEM syringe pump was designed and used to inject the material at a controlled rate. This pump was powered using an in-house build custom controller, which was interfaced with the computer serially and controlled via LabVIEW. The solution that was sprayed was contained within a 1 mL glass Hamilton syringe. This was connected via PEEK tubing to a conical, stainless steel 26 gauge needle. The high voltages required to generate the electrospray were produced using the same controller as the syringe pump.

The interface between atmosphere and vacuum is a 64 mm long, 1.59 mm OD, 0.508 mm ID stainless steel capillary. This is mounted inside of an aluminum heater block using Swagelock fittings, as shown in Figure 15. The heaters that power the heater block are controlled using PID control and are part of the in-house built custom controller used for the syringe and electrospray voltages.

To power the ion funnels used in this study, a separate custom controller was used. This controller contained four DC power supplies to control the voltage gradient along the funnel, the jet disrupter, and the extraction lens voltages. The voltage gradients along the funnels were generated by connecting each of the lenses of the funnels in series with 510 kOhm resistors and applying DC voltages to the first and last lenses of each funnel. In addition to the DC signals produced, the controller generated the two out of phase RF signals that were applied to the adjacent lenses of the funnel.

38

Each DC and RF supply was monitored by a dedicated integrated circuit. The controller was connected serially to the computer and controlled and monitored by a LabVIEW program.

2.6.2 Electroplated FDM Experiments

All experiments using the electroplated FDM components were performed on the vacuum chamber shown in Figure 16. Figure 16 shows the arrangement for the hermacity tests. Helium is pumped in to the high-pressure side of the sample and the low pressure side monitors the helium using an RGA. The sample is placed in between the flanges circled in red. The pressure of the helium injected in to the system is
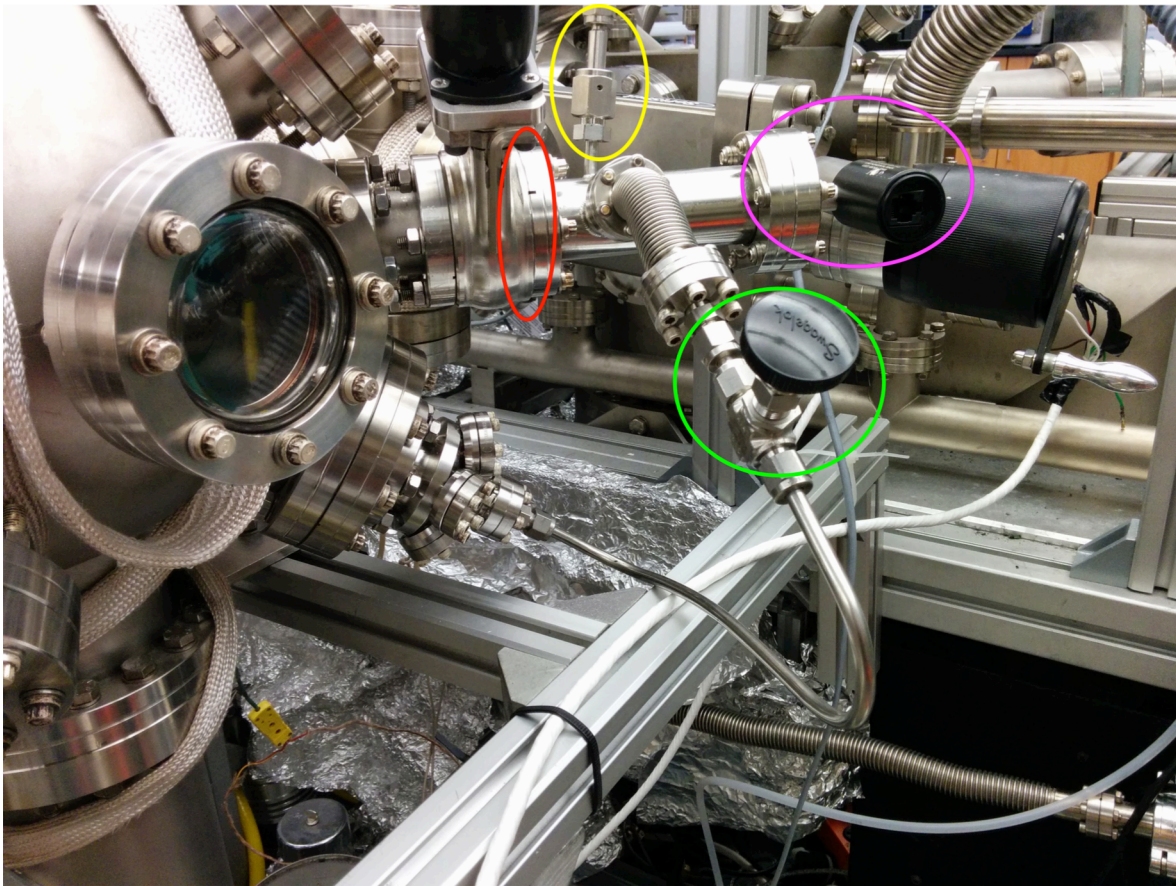
Figure 16: Image of the vacuum chamber used for the hermacity tests when sealing the components using electroplating.

monitored by the pressure gauge circled in magenta. The helium is injected through the port circled in yellow. After pumping the high-pressure side down, it is isolated using the value circled in green. The full details of the hermacity test procedure are found in Chapter 5. For the proof of concept testing the flange circled in red is removed and replaced with the component in test. The chamber is pumped by a turbomolecular pump backed by an oil-sealed rotary vane pump.

The RGA used in the system was an RGA-300 produced by Stanford Research Systems. This unit is capable of measuring the mass of ions up to 300 AMU. It has a resolution better than one AMU, has a partial pressure range of six decades (10^{-5} to 10^{-11} Torr), and has a detection limit of 5×10^{-14} Torr. The device uses a quadrupole mass filter to discriminate the ions generated by the dual thoriated-iridium filament. The system communicates with the computer via RS-232 and is completely programmable. However, for this study the software package RGA Windows was used to measure all partial pressures [68].

Electroplating was performed using a commercially purchased kit from Caswell Plating (Lyons, NY). The kit was supplied with the crystalized metal salts used to produce the electroplating baths, a powdered degreaser, and liquid brighteners. Nickel and copper anodes were also supplied with the kit. Three 2-gallon HDPE buckets were also included, in which the degreaser and electroplating solutions were placed. To suspend the work pieces while in the baths, tank bars were produced using 1/2" copper tubing. Two constant current DC power supplies were used to generate the appropriate current to perform the plating: a Sorensen XT 30-2 for low current applications and a

Sorensen DCS33-33E for high current applications.   To monitor the current, a multimeter was placed in series with the electroplating circuit.

CHAPTER 3: ENHANCED SIMULATION OF AN RF ION FUNNEL INCLUDING GAS TURBULENCE[1]

3.1 Abstract

Electrodynamic ion funnels are used to enhance the transmission of ions in electrospray-based ion injection systems in the 0.1 to 30 Torr pressure range. Jet disrupters are commonly employed to prevent droplets and high pressure jets from entering subsequent vacuum regions. This study presents the simulation and testing of an ion funnel containing a jet disrupter using computational fluid dynamics (CFD) and SIMION ion trajectory simulations. Traditional modeling approaches have utilized approximations for the bulk fluid flow fields without including the time-varying nature of the turbulent flow present in the system, thus yielding idealized results. In this study, the fluid flow fields are calculated using CFD. In an effort to include time-dependence, a random velocity vector, whose magnitude is proportional to the square root of the turbulence kinetic energy, was calculated at each time step and added to the velocity of the ions. These simulations predicted that the transmitted ion current is effectively modulated by the variation of the jet disrupter voltage. The addition of the random velocity vector produced results that closely matched the experiments. The simulations yielded the dependence of the transmission on the jet disrupter voltage, and the voltage necessary for maximum ion throughput was accurately predicted. In addition, the

magnitude of the predicted transmission closely matched that of the experimental results. This modeling approach could be extended to similar ion transport and filtering systems in which the effects of turbulent fluid flow cannot be ignored.

3.2 Introduction

Electrospray ionization is a process, which enables the extraction of macro-molecular ions directly from the solution environment [6]. The method allows mass spectrometry of thermally fragile molecular materials such as proteins and polymers [7]. This process can also be used for the deposition of thin films of such materials in vacuum [8-10, 15, 69]. Systems employing electrospray as an ion source utilize several differential pumping stages through which ions are transported for deposition or analysis. Optimizing ion throughput while maintaining vacuum is crucial for these systems.

The ion funnel, developed by Shaffer et al. [17], improves the transmission of ions through the first vacuum stage (0.1 to 30 Torr). The device consists of several stacked ring electrodes, the diameters of which reduce along the axis thus forming a conical shaped electrode cavity. Improvements on this initial design include the reduction of electrode spacing [70] and the addition of a jet disrupting electrode [19] increasing the sensitivity and decreasing the pumping requirements (and transmitted droplets) respectively.

The implementation of a jet disrupter in an RF ion funnel allows for the use of a high conductance atmospheric/vacuum interface, increasing the amount of injected ions [19]. This electrode is located in the center of the funnel and can also act as a gate, preventing the transmission of ions, as well as preventing large solvent droplets and

43

high pressure gas jets from passing into the subsequent chamber. As a result, this electrode reduces the pumping speed required for the second stage, and prevents the entrance of droplets into the higher vacuum stages. The efficiency of the jet disrupter crucially depends on the applied DC voltage [71].

Several studies have investigated ion funnels with jet disrupting electrodes, both experimentally and numerically [19, 71]. These studies are accurate in their prediction of the optimum jet disrupter voltage however the calculated transmission values are idealized. The focus of the presented study is on an improved method of modeling an ion funnel that contains a jet disrupter which was then validated experimentally. This study adds to previous investigations by utilizing a calculated flow field over the simulated domain and an approximation of the time-varying nature of the fluid flow, resulting in a simulation that closely matches experimentally obtained results. This was accomplished via computational fluid dynamics (CFD) and ion trajectory simulations in combination with experimental verification. The calculation of a steady state fluid flow field combined with an ion trajectory model for the performance of a parametric simulation study of the jet disrupting element voltage allowed for the calculation of the optimum applied electric field. In this study, the computational fluid dynamics package OpenFOAM [34] and ion trajectory simulation software SIMION [42] were used to simulate the forces acting on ions within the first differential pumping stage of the system.

44

3.3 Methods

3.3.1 Physical Apparatus and Materials

Electrospray is performed by applying a potential difference between a solution carrying needle and a counter electrode. For a needle-electrode spacing of approximately 1 to 2 mm, voltages in the range of 1 to 2 kV are typical. In the case of electrospray injection into vacuum, the counter electrode is formed by the intake orifice or capillary to the first differential pumping stage. High ion transmission from the first pumping stage into the second is desired, which makes it necessary to utilize beam shaping ion optical elements in this stage to guide the ions to an exit aperture and into the next pumping stage. This is often achieved with the use of an ion funnel [45, 70, 71].

The focusing effect of the ion funnel is a function of the applied electric fields. A typical ion funnel contains several stacked ring electrodes with decreasing diameter and an inter-electrode spacing in the range of 0.5 to 2.0 mm. A sinusoidal RF voltage is applied to each electrode, with adjacent electrodes being 180 degrees out of phase. Superimposed on these electrodes is a linear DC voltage gradient. As the ions travel down the electrode stack the RF fields create an effective potential V_{eff} perpendicular to the axis of the electrode inner diameters [72]. This potential forces the charged droplets and ejected solute ions back towards the axis of the ion guide. V_{eff} can be expressed as:

$$V_{eff} = Kf(r, z)$$

with

$$K = \left(\frac{Z^2 \cdot q^2 \cdot V_0{}^2}{4 \cdot m \cdot \omega^2 \cdot z_0{}^2} \right)$$

where m and Z are the ion mass and charge state, q is the electronic charge, ω and V_0 are the RF frequency and amplitude, and z_0 is the electrode spacing. The magnitude

45

of the force acting on the charged particles depends on the axial and radial positions z and r, but is strongest near the electrodes. The DC voltage applies a force on the ions along the beam axis. Due to the combination of the DC and RF fields and the decreasing diameters of the electrodes, the ions are directed radially inward as they are pushed forward.

The electrospray was generated using a syringe pump (New Era NE-300) and an in-house designed control system. The solution was dispensed with a 1 ml Hamilton Glass Syringe through a Hamilton 26 gauge conically tipped hypodermic needle. The injected molecular species used for testing was cytochrome-c (Sigma-Aldrich, >95% purity, Lot# 031M7022V). Twenty milligrams of cytochrome-c were mixed with 18 ml methanol, 1.8 ml DI water and 0.2 ml glacial acetic acid and the solution refrigerated at approximately 4 °C until use.

The interface between atmosphere and the first differential pumping stage consists of a heated aluminum block with a 64 mm long, 0.508 mm (0.020") ID capillary. Two 40 Watt DC cartridge heaters controlled by an in-house built PID controller are used to heat the aluminum block. The heated capillary serves to increase the desolvation rate of the injected droplets.

The RF ion funnel (shown in Figure 17) is located in the first chamber, which is typically operated at a pressure of approximately 2 Torr (when using a 0.508 mm ID intake capillary and a 28 cubic feet per minute mechanical evacuation pump). The RF ion funnel contains 99 ring electrodes, in which the first 54 electrodes have constant inner diameters of 25.4 mm. The last 45 electrodes linearly decrease in inner diameter from 25.4 mm to approximately 2 mm. All electrodes are 0.5 mm thick and spaced 0.5

mm apart. The 20th and 21st electrodes are replaced by the jet disrupting electrode, which is located in the space between where these two electrodes would be placed. This electrode is a 6.5 mm diameter disk concentric to the ring electrodes supported by very thin members. There is a final "extraction lens" electrode placed after the last of the tapered electrodes with a diameter of approximately 2 mm. The purpose of this electrode is the extraction and focusing of the ion beam into the second vacuum chamber. This design is similar to that of Kim, et al. [19].

All electrodes (except the jet disrupter and extraction lens) are serially connected through a chain of 510 kOhm resistors. This enables the application of a DC voltage gradient along the funnel axis, which accelerates ions towards the exit aperture. Superimposed on this linear voltage gradient are two 180° out of phase sinusoidal (approximately 700 kHz) RF voltages, which are coupled in an alternating fashion into the electrodes. This generates the pseudo potential and resultant force mentioned above, which steers the ions away from the electrodes towards the funnel-axis. In combination the RF and DC fields result in a funneling effect, propelling the ion stream into the exit aperture of the funnel region, thereby significantly increasing the ion transmission rate.

3.3.2 Computational Fluid Dynamics Simulations

Computational fluid dynamics simulations were performed using the OpenFOAM computational fluid dynamics toolbox [34]. Due to the symmetric and concentric nature of the capillary and ion funnel geometry, an axially symmetric model was developed. This simplified geometry strongly reduced the computation time required for modeling, thus enabling a larger number of simulations to explore a wider range of funnel

47
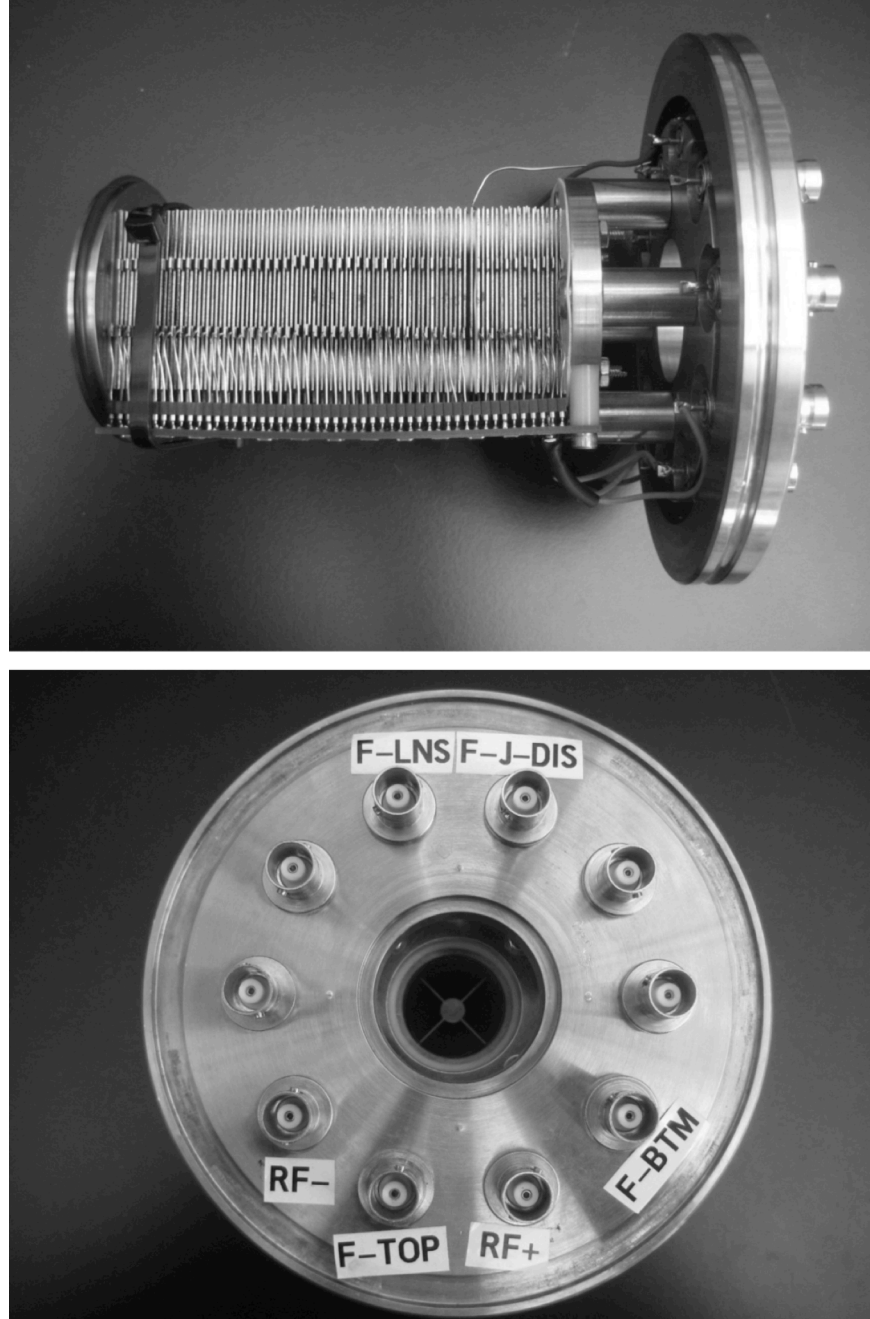
Figure 17: Images of the RF Ion Funnel removed from the first differential pumping chamber. In the top image the parallel plate ring electrodes can be observed. The bottom image, taken along the axis of the funnel, shows the jet disrupting element.

potentials. High pressure gradients were expected to result in shock features at the exit

of the capillary into the chamber. An OpenFOAM solver developed by Greenshields et

al. suitable for viscous, compressible, transonic flow situations was utilized [35]. The k-

ω SST turbulence model [73] was used due to its ability to accurately predict flows with

48

shock features and high gradient flows [33]. Wall boundaries were modeled using the no-slip condition. Pressure inlet and outlet boundary conditions were placed at the atmospheric and low pressure boundaries respectively. Viscosity was modeled using the two coefficient Sutherland's equation with coefficients of 110.4 K and 1.458 x 10^{-6} kg·(ms)$^{-1}$·(K)$^{-1/2}$ for S and C_1 respectively. The geometry was meshed using the open source software Gmsh [74].

3.3.3 Ion Trajectory Simulations

SIMION version 8.0 was used to perform ion trajectory simulations. SIMION solves the Laplace equation to determine the electric field at a point, then uses Runge-Kutta time integration to predict ion flight paths. Other groups have successfully used SIMION to predict the trajectory of ions through RF ion funnels [17, 43-45]. An ion-gas interaction model (HS1) based on simple hard-sphere physics was modified and used to simulate the interaction between the background gas and ions. This model is in agreement with several other published results [75, 76].

The original HS1 model included with SIMION 8.0 allows the user to specify a uniform velocity, temperature, and pressure background gas field for the computational domain. The code of the model was modified for this study to allow the importation of vector and scalar fields representing these spatially varying bulk gas properties. In this way the steady-state result fields from CFD simulations could be included with the ion trajectory simulations. Due to the nature of the turbulence model employed for the gas flow simulations, the resulting bulk flow fields are time-averaged. In reality this is not the case as turbulence manifests as random time-varying fluctuations within these fields around a mean value. To account for this time-varying component, the turbulence

49

kinetic energy (k) field calculated during the CFD simulations was also imported into the ion trajectory simulations.

The turbulence kinetic energy is defined as:

$$k = \frac{1}{2}\left(\overline{u'_x{}^2} + \overline{u'_y{}^2} + \overline{u'_z{}^2}\right)$$

where u'_x, u'_y, and u'_z are the time-varying components of the velocity in the x-, y-, and z- directions respectively. For the current study, at each time step a randomly oriented velocity component scaled proportionally to the square root of the turbulence kinetic energy is calculated. This velocity component is added to the time-averaged value from the imported bulk flow velocity field. In this way the influence of the time-varying component of the turbulence is included. This velocity component is referred to as the "randomization parameter" in this study. Without the addition of the randomization parameter simulations would not run to completion as ions become virtually trapped in areas of the least local energy.

Positive ions were used in all simulations (and experiments). To run a simulation, 100 single ions were assumed to be ejected from the end of the capillary, randomly distributed within a circle whose diameter is that of the inner diameter of the capillary. The ions were flown individually with no Coulombic space charge interaction. The mass of the ions was 12,233 amu (cytochrome-c) with a charge state of +15 [17]. The initial kinetic energy of the ions was taken as a uniform value based on the average simulated velocity at the capillary exit and the mass of cytochrome-c. The energy corresponding to this velocity was 12.8 eV, however due to the elevated pressure of the system ions quickly reach thermal equilibrium with the background gas, dissipating initial kinetic energy via collisions [77]. Simulations were terminated when all 100 ions

had contacted a solid surface in the funnel (i.e. one of the electrodes of the system) or had passed through the exit aperture. The transmission efficiency of the simulation was determined by counting the number of ions that passed through the exit aperture and did not come in contact with either the electrodes or the jet disrupter.

The DC voltage gradient applied to the lenses in the simulation began at 200 V at the first electrode and varied linearly to 40 V at the last electrode. A sinusoidal alternating voltage was applied to the lenses with an amplitude of 100 V_{pp} and a frequency of 700 kHz. A voltage of 20 V was applied to the extraction lens. The voltage applied to the jet disrupter was varied from 100 V to 260 V.

3.3.4 Experimental Procedure

To determine the validity of the simulated ion trajectories, experiments were performed with the physical apparatus. Electrospray was performed by pumping the solution at a rate of 1 µl/min through the Hamilton needle. The needle and capillary inlet were placed 1 mm apart. A voltage of +1800 V was applied to the needle and a voltage of +210 V applied to the capillary/heater block. The heater block was heated to a temperature of 130 °C. The presence of electrospray was confirmed optically with the use of a 532 nm laser to illuminate the resulting aerosol.

The ion current is proportional to the number of ions generated in the electrospray [12]. This current can therefore be used to quantify the amount of material injected into the system. By electrically coupling all of the electrodes in the funnel, the current deposited on them can be obtained and the total amount of current entering the system through the capillary is measured. In a similar manner, by coupling all of the electrodes in the subsequent chamber (quadrupole ion guide) and measuring the

51

resulting current when the funnel is energized the amount of material being transmitted through the funnel can be determined. The current in the second chamber divided by the total current into the funnel chamber yields the transmission efficiency.

The electrode voltages used in the physical experiment were identical to those applied in the SIMION simulations. For the current experiments the total current into the funnel was measured. The voltage of the jet disrupting element was then swept from 100 to 260 V and the current output through the funnel exit was measured. This was repeated several times.

3.4 Results and Discussion

Figure 18 shows the velocity and turbulence kinetic energy fields of the entire domain as well as the region around the capillary exit into the vacuum chamber calculated using OpenFOAM. The jet issuing from this region displays a barrel shock and a Mach disk, both characteristic features of under expanded supersonic jets [78]. Further along the beam axis the jet encounters the jet disrupting element, which deflects the jet radially away from the funnel axis. The flow reaches the inner edge of the ring electrodes then splits into two counter rotating vortices.

Because of the geometry of the capillary, the gas flowing within will become choked (i.e. the flow becomes mass flow rate limited). According to literature, along the centerline the location where the Mach number of the flow is 1 occurs several diameters upstream of the capillary exit [27]. In this simulation this point occurred 1.45 mm upstream of the capillary exit. The Mach disk in the simulation is located 3.6 mm downstream from the capillary exit, which matches the theoretical prediction of 3.55 mm from the literature [22].

52

It can be seen that the diameter of the jet boundary oscillates as it travels from the capillary exit. This is because the expanding gas in the jet, initially at a higher pressure than the surrounding gas, decreases in pressure below that of the surrounding gas during expansion. Because the gas velocity is greater than the speed of sound, the surrounding gas cannot immediately equalize the pressure at the jet boundary. The result is that the pressure of the gas within the jet will decrease to a value lower than that of the surrounding gas, causing a pressure gradient directed radially inward. This causes the flow to change direction back toward the funnel axis. When the gas travels toward the center it will increase in pressure and over shoot the surrounding gas
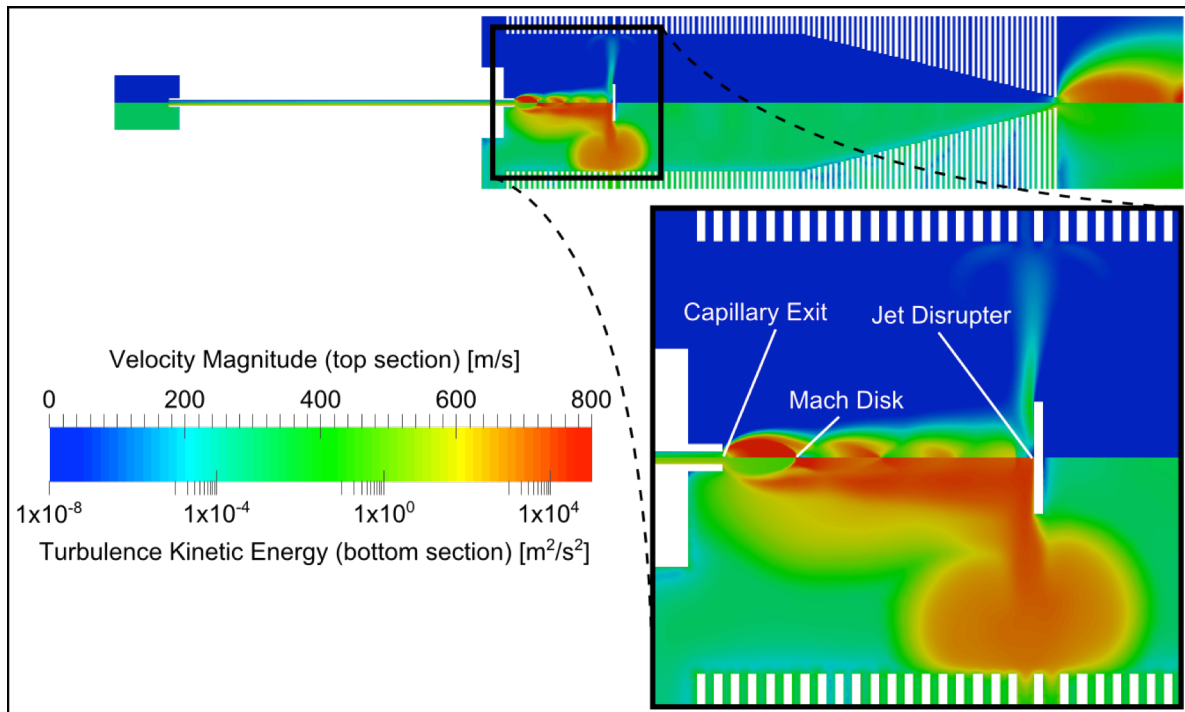
Figure 18: Velocity magnitude field (top section) and turbulence kinetic energy field (bottom section). A close up view of the capillary exit and jet disrupter is shown in the inset. Typical features of a highly under expanded jet, including the Mach disk and barrel shock, can be observed emitting from the capillary. The oscillatory behavior associated with these jets is also observed. The jet can be seen impinging on the jet disrupting element. The turbulence kinetic energy is highest within the jet after the Mach disk as well as in the flow radiating outward from the jet disrupter.
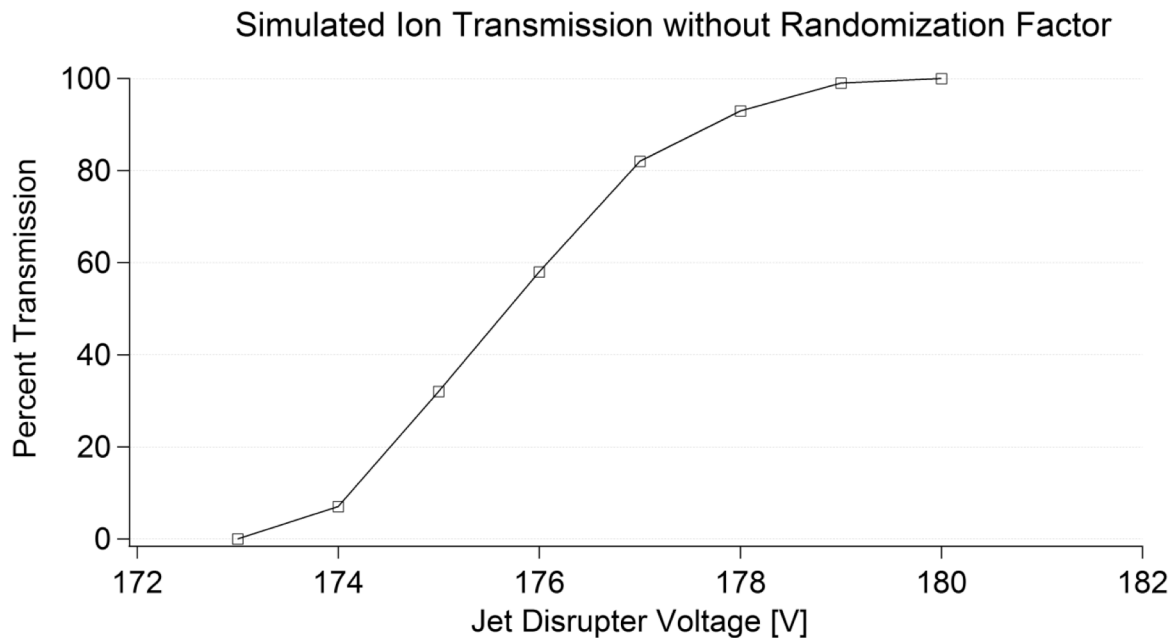
Figure 19: This graph indicates the initial results from the SIMION simulations in the absence of the randomization factor. It should be noted that for this idealized system there was a very narrow range of voltages that could be applied to the jet disrupting element. Below this range all ions collided with the jet disrupting element. Above this range ions become confined in local low energy areas, preventing completion of the simulation.

pressure, which will result in a second expansion of the jet. The end result is an oscillation of the flow toward and away from the axis in an attempt to reach equilibrium with regard to the pressure.

The results from these CFD simulations were coupled with the model of the ion funnel used in SIMION to calculate ion trajectories. Initial attempts, which did not include the randomization factor, produced simulated transmission results that increased sharply from no transmission to 100% within a range of a few volts as shown in Figure 19. Also, in the simulations, if the jet disrupter voltage was further increased after reaching a value which produced 100% transmission, the simulated ions would became spatially confined, forcing the simulation to run indefinitely.

Changes were made to include the spatially varying randomization factor, which is added to the velocity of the ions in the simulation, as described earlier. This was added to include the time-varying nature of turbulence into a model that had previously been approximated using a steady-state fluid flow field. The magnitude of the randomization factor vector is scaled by the square root of the turbulence kinetic energy. The turbulence kinetic energy field is shown in Figure 18. This modification prevented ions within the simulation from becoming confined, forcing them to either impact an electrode or become ejected locally into an area where they continue along the length of the funnel. The results of the ion trajectory simulations are shown in Figure 20, plotted together with the data obtained from the experiments in which the jet disrupting element voltage was varied. In these simulated results, close to 50% of the ions injected were transmitted through the funnel using a jet disrupter voltage of 175. The maximum transmission obtained experimentally was approximately 54% using the same jet disrupter voltage. This voltage is approximately 5 V above the DC potential of the electrodes adjacent to the jet disrupter which is in agreement with Kim, et al. [19]. Some difference in transmission between experiment and simulation is expected, since the actual experiment includes contributions from solvent ions, droplets, etc. which are not addressed in this study. In addition, simulation statistics including the finite number of ions simulated and the random nature of the velocity vector can affect the results.

The overall shape of the curve obtained from the experimental results closely matches that of the simulated results as shown in Figure 20. The onset of ion transmission, slope before the peak, as well as the voltage where peak transmission is observed were accurately predicted in the simulations. Various parameters can

www.manaraa.com

Simulated and Experimental Ion Transmission
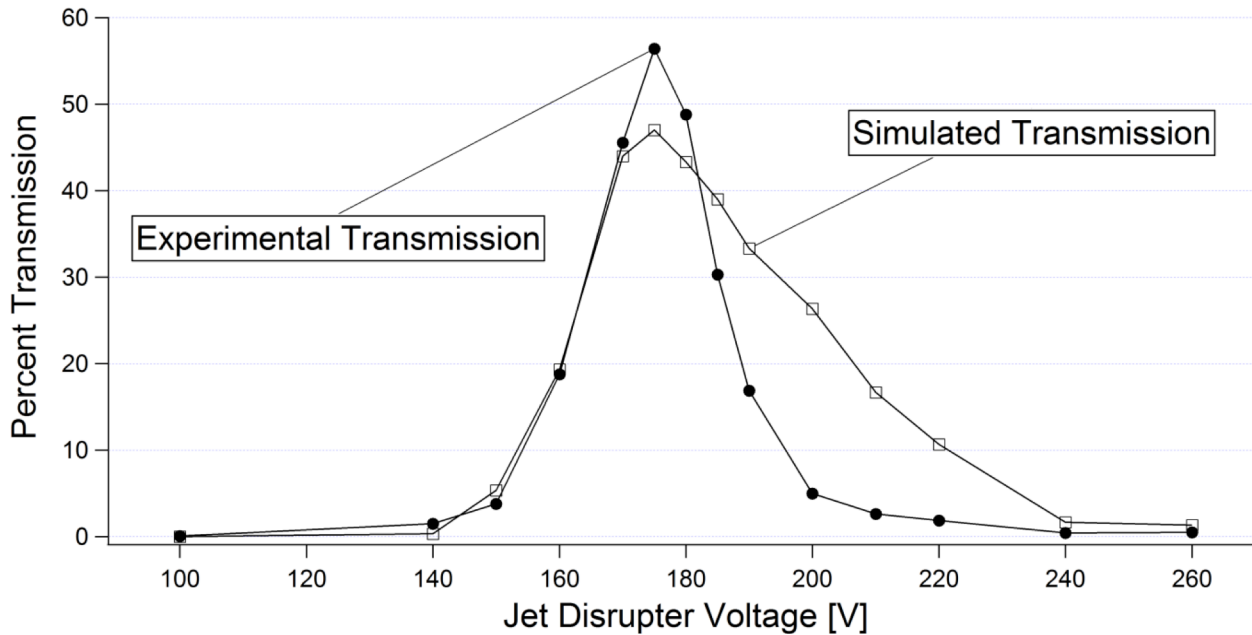
Figure 20: Simulations (after addition of the randomization factor) and experimental results for transmission as a function of voltage on the jet disrupter. The voltage for the onset of transmission, peak transmission voltage as well as actual values of transmission were similar in both cases.

influence the effectiveness of the funnel in focusing the ions, which are assumed to be due mainly to the presence of solvent ions and droplets in the spray. These parameters include solution concentration, solution flow rate, desolvation temperature, emitter to capillary distance, and emitter diameter. Also of importance is the pH of the solution which will affect the average charge state of the solute ions [79].

In the physical apparatus all of the small ion-containing droplets did not completely evaporate prior to entering the vacuum chamber. In addition, highly charged and comparably heavy droplet residues were also formed due to droplet evaporation [80]. Because these large particles are injected with a high velocity their trajectory along the funnel axis becomes more difficult to alter than the free, gas-phase ions. The

56

jet disrupter prevents these particles from continuing along the beam line. In experimentation however, all injected charged particles are counted toward transmission, including those that contact the jet disrupter. In SIMION all particles are idealized as gas phase ions. This results in a discrepancy in the simulations when not accounted for. The desolvation temperature, emitter to capillary distance and flow rate all influence the size of the resulting droplets and therefore the rate of production of gas phase ions [13].

The absence of space charge effects also plays a role in the accuracy of the simulations. With the presence of a high number of particles in a small area, the space charge causes the resulting cloud of ions to become larger, thereby increasing the risk of accidental collision with electrodes. This effect is not accounted for in these simulations and is an area of interest for future numerical investigation. The addition of space charge effects would likely decrease the number of transmitted ions due to the increased rate of accidental collisions with electrodes. However, other studies state that the ion funnel is effective over a wide range of m/z values, indicating some robustness to space charge effects [80].

Other groups have performed ion funnel simulations [17, 45] including some that include constant gas flow fields [43] as well as spatially varying analytical estimations of gas flow field [19, 70, 71]. The presence of ion-gas collisions within the simulation is necessary for the correct function of the model. The collisions between ions and background gas reduce the energy of the ions to a level where the applied electric field will effectively alter the ions' trajectories; however, if these collisions become too frequent the strength of the electric field will no longer be sufficient to alter these

57

trajectories. The studies, which include gas flow only, provide estimations of the flow field. By solving the equations of fluid motion, CFD can provide even more insight into the nature of gas flow in such a complex system.

Tang, et al. performed numerical and experimental investigation of an electrospray ion funnel similar to this current investigation [71]. They approximated the fluid flow within the funnel as the superposition of an axial flow and a radial flow at the surface of the jet disrupter. This simulation resulted in a maximum theoretical efficiency of 100%. Although accurately predicting the voltage at which maximum transmission occurs, this simulation resulted in unrealistic transmission efficiency values. The introduction of the randomization factor to the gas flow in the present study results in a more realistic simulation and, therefore, a transmission much less than 100% as is always observed in the experimental situation.

3.5 Conclusion

The presented results demonstrate that combining CFD calculated flow fields and a modified form of SIMION's HS1 ion-gas collision model provides a good simulation of RF ion funnels. The transmission behavior when varying the jet disrupter voltage was similar in both the simulation and experiments; the shape of the curves and corresponding maxima were comparable. This study represents an enhancement of the simulation of ion transport within an ion funnel that utilizes a jet disrupter. Earlier simulations with analytical approximations of gas flow or a stationary bath gas resulted in too high transmission values. The introduction of a randomization factor allowed the modeling of the time-varying nature of the turbulent flow, not present in the previous studies, resulting in a more quantitatively accurate simulation. The use of this model

58

could be extended to other ion transport systems in which the turbulent effects of the fluid flow are present.

CHAPTER 4: HIGH TRANSMISSION 3D PRINTED FLEX-PCB BASED ION FUNNEL[2]

4.1 Abstract

In this study a novel fabrication method for an RF ion funnel is presented. RF ion funnels are important devices for focusing ion clouds at low vacuum conditions for mass spectrometry or deposition related applications. Typically, ion funnels are constructed of stainless steel plate ring electrodes with a decreasing diameter where RF and DC potentials are applied to the electrodes to focus the ion cloud. The presented novel design is based on a flexible circuit board that serves both as the signal distribution circuit and as the electrodes of the ion funnel. The flexible circuit board is rolled into a 3D printed scaffold to create a funnel shape with ring electrodes formed by the copper electrodes of the flexible circuit board. The design is characterized in direct comparison with a conventional steel-plate electrode design. The discussed results show that the new funnel has similar performance to the conventionally designed funnel despite much lower manufacturing costs.

4.2 Introduction

Electrospray ionization (ESI) extracts macro-molecular ions from solution and is frequently employed in mass spectrometry and thin film deposition for thermally fragile molecular materials [8, 11, 15, 69, 81-83]. During ESI, ions are produced at atmospheric pressure, while analysis and deposition are usually performed at

---

magnitudes lower pressures. As a result, ESI systems are usually based on a sequence of differentially pumped vacuum stages. In such vacuum systems it is important to optimize the ion transmission through the different stages. The RF ion funnel with jet disrupter design is frequently used in the first vacuum stage to optimize ion transmission in the low Torr range [71]. Initial ion funnel designs were constructed with electrode stacks made of stainless steel plates. More recently, commercial mass analysis systems such as the Agilent 6490 LC/QQQ utilize ion funnels constructed of rigid printed circuit boards [20]. The presented study focuses on the performance of an RF ion funnel constructed using flexible circuit board technology and a 3D printed scaffold structure.

The new ion funnel design was characterized in direct comparison with a conventional steel plate based funnel design. The experimental protocol of the presented study follows earlier ion funnel characterization efforts to enable direct comparison of our results. There have been several studies analyzing the efficiency of RF ion funnels with designs similar to Kim et al. [70]. These studies have investigated the effects of varying the jet disrupter voltage [19, 71] and the RF amplitude [70] on the ion transmission efficiency.

4.3 Methods

4.3.1 Physical Apparatus and Materials

Electrospray ionization is performed by applying an electric field of several kilovolts per centimeter between an electrospray emitter needle or capillary and a counter electrode held at a distance of a few millimeters. When injecting into a vacuum chamber the counter electrode is often a heated capillary serving as a mass transport

61

interface between atmospheric conditions and the first vacuum stage. The injection process involves forcing a solution containing the ionized solute through the electrospray emitter at a flow rate on the order of 1 microliter per minute. Under the applied electric field this results in the formation of a Taylor cone [13] with subsequent formation of an ionized aerosol, which enters the first vacuum stage via the heated capillary. During transfer through the capillary, part of the solvent evaporates and ionized solute emerges as individual molecular ions.

This mix of ions and droplets encounters the ion funnel upon entering the first pumping stage. The ion funnel focuses the liberated ion component into the funnel exit, while blocking most of the remaining aerosol droplets via the in-stream jet disrupter. This results in a substantial transmission of ions into the subsequent pumping stage while preventing the transmission of droplets and other neutral particles [18, 44, 45, 70, 71, 84]. The device typically contains 100 stacked ring electrodes decreasing in diameter along the axis. The inter-electrode spacing is generally between 0.5 and 2.0 mm. A sinusoidal RF voltage is applied to these electrodes with the signal applied to adjacent electrodes being 180 degrees out of phase with one another. The RF field creates an effective electric potential V_{eff} perpendicular to the inner diameter of the electrode stack forcing the ions radially inward. V_{eff} is expressed as:

$$V_{eff} = Kf(r,z)$$

where

$$K = \left(\frac{Z^2 \cdot q^2 \cdot V_0{}^2}{4 \cdot m \cdot \omega^2 \cdot z_0{}^2} \right)$$

and m and Z are the ion mass and charge state, q is the electronic charge, ω and V_0 are the RF frequency and amplitude, and z_0 is the electrode spacing. [85] The

magnitude of the effective electric potential is dependent on the axial and radial positions, z and r respectively. This results in a field that points perpendicularly inward, away from the surface of the cavity formed by the electrodes. The DC voltage gradient generates a force parallel to the axis of travel forcing the ions toward the exit aperture and into the second vacuum stage. The combination of applied electric fields along with the decreasing ring diameter serves to move the ions forward and radially inward.

The jet disrupting electrode allows for a high conductance atmosphere to vacuum interface, increasing the amount of transmitted ions [19, 71]. This electrode is located concentric to the other ring electrodes in front of the capillary exit. When provided with an appropriate electric potential the jet disrupting electrode blocks the transmission of large diameter solvent droplets and high pressure gas jets from passing into the next vacuum stage, while allowing liberated ions to pass around the electrode. Blocking the high pressure gas jet reduces the pumping speed required for the subsequent vacuum stage. The efficiency of the ion funnel is heavily dependent on the DC voltage applied to the jet disrupter [19, 84].

The electrospray source was established using an in-house designed control system and syringe pump. The solution was injected through a 1 ml Hamilton Glass Syringe into a Hamilton 26 gauge conically tipped hypodermic needle with a final inner diameter of 125 μm (Hamilton, 7785-01). The molecular species cytochrome-c was used for testing. Twenty milligrams of stock cytochrome-c (Sigma-Aldrich, >95% purity, Lot # 031m7022V) were mixed with 18 ml methanol, 1.8 ml deionized water and 0.2 ml glacial acetic acid. Once the solution was formed it was refrigerated at approximately 4º C until use.

The interface between atmosphere and the first vacuum stage consists of a heated aluminum block with a receptacle for a 1/16" outer diameter capillary through which the ions pass from the ESI emitter into the first vacuum chamber. The capillary is 64 mm long and has an internal diameter of 0.508 mm (0.020"). Two 40 Watt DC cartridge heaters heat the block and are controlled by an in-house built PID controller. Heating the capillary increases the desolvation rate of the injected droplets resulting in more gas phase ions.

The first vacuum chamber contains the RF ion funnel and is typically operated at a pressure of approximately 1.9 Torr. The functionality of the two different ion funnels was compared using the same vacuum system. The design of the flexible circuit board funnel allowed operation as a drop-in replacement for the conventional funnel, which enabled a direct comparison of the performance of the two funnel designs. The conventional ion funnel (shown in Figure 21) used for comparison is similar to the design of Kim et al. [19] consisting of 99 ring electrodes punched into square stainless steel plates. The first 54 electrodes have a constant diameter of 25.4 mm with the diameter of the last 45 electrodes decreasing linearly from 25.4 mm to approximately 2 mm. Electrodes are spaced 0.5 mm apart and are 0.5 mm thick. The jet disrupting electrode replaces the 20th and 21st electrodes and is made of a 6.5 mm diameter disk concentric to the ring electrodes and supported by four 1 mm wide beams. At the end of the funnel there is a final "extraction lens" electrode with a DC potential applied to it. The purpose of the extraction lens is to focus the beam into the second vacuum chamber and block RF cross-talk between the ion funnel and the quadrupole ion guide in the subsequent chamber [19].

64
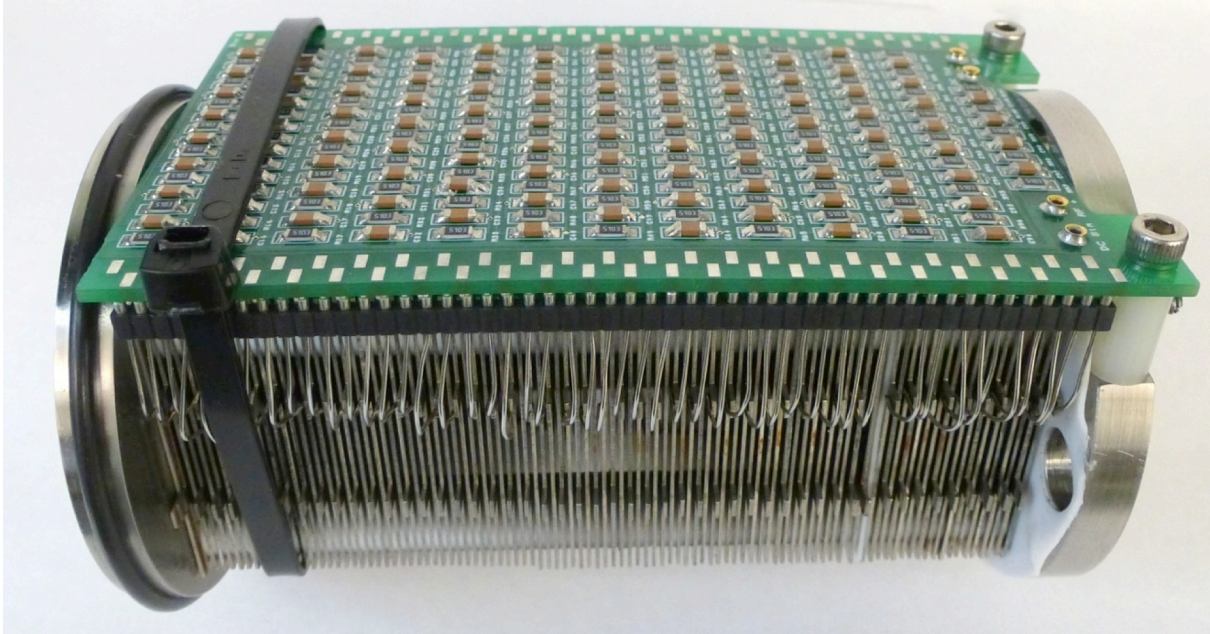
Figure 21: Image of the conventional ion funnel removed from the flange. The photo is perpendicular to the axis of the funnel, showing the circuit board and stainless steel plate electrode connections.

The flexible printed circuit board based funnel was constructed using a 3D printed scaffold serving to hold the flexible board in place in a funnel shape. The flexible circuit board has 99 traces printed in such a way that when rolled into the 3D printed housing, it creates an arrangement of electrodes similar to those of the stacked ring electrodes of the conventional ion funnel. Details are shown in Figure 22. The entire flexible ion funnel included 5 distinct parts printed in acrylnitrile-butadiene-styrene (ABS). ABS was chosen because of its durability and strength characteristics. The five 3D printed parts are the front plate, the two-part flexible circuit board scaffold, the jet disrupter, and the back plate. The front plate contains holes for shoulder bolts used to mount the funnel to the vacuum chamber flange. The flange contains the aluminum heating block and the capillary and seals the vacuum chamber from the atmosphere. The scaffold section containing the rolled flexible circuit board was printed in two separate pieces to allow for

65

the insertion of the 3D printed jet disrupter between two sections of electrode traces on the flexible circuit board. The housing segments have a slot cut in one side, allowing the insertion of the electrode part of the flexible circuit board into the scaffold, while enabling contact to the signal distribution network and external connectors to the RF and DC supplies. The back plate connects to the front plate by four rods on the outside of the scaffold. This serves to hold the housing segments and jet disrupter together
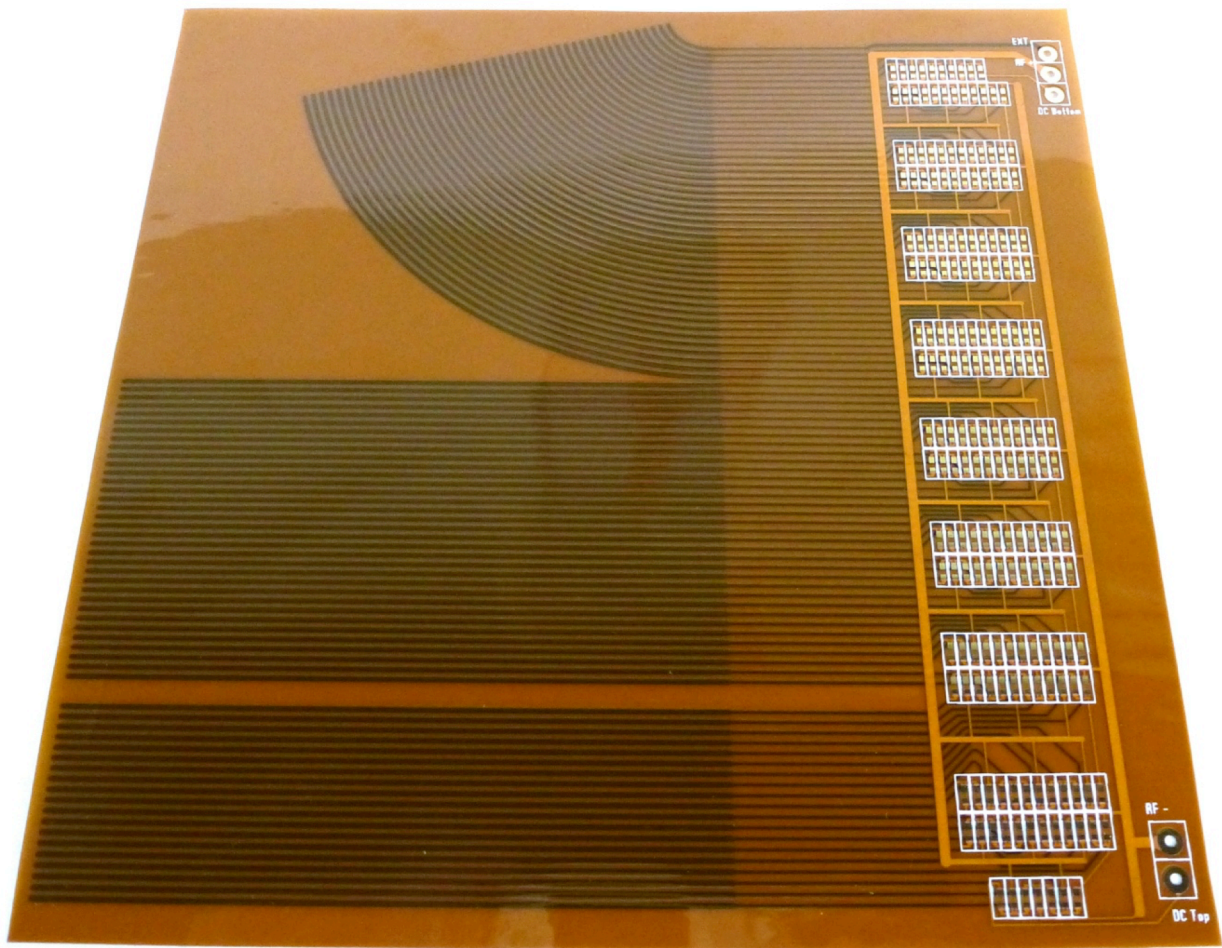
Figure 22: Images of the flexible RF Ion funnel during assembly. In the top image the circuit board is shown before electronic components are added, cutting, and solder mask removal. The bottom image, taken along the axis of the funnel before solder mask removal, shows how the flexible circuit board rolls forming the traces into ring electrodes.

66
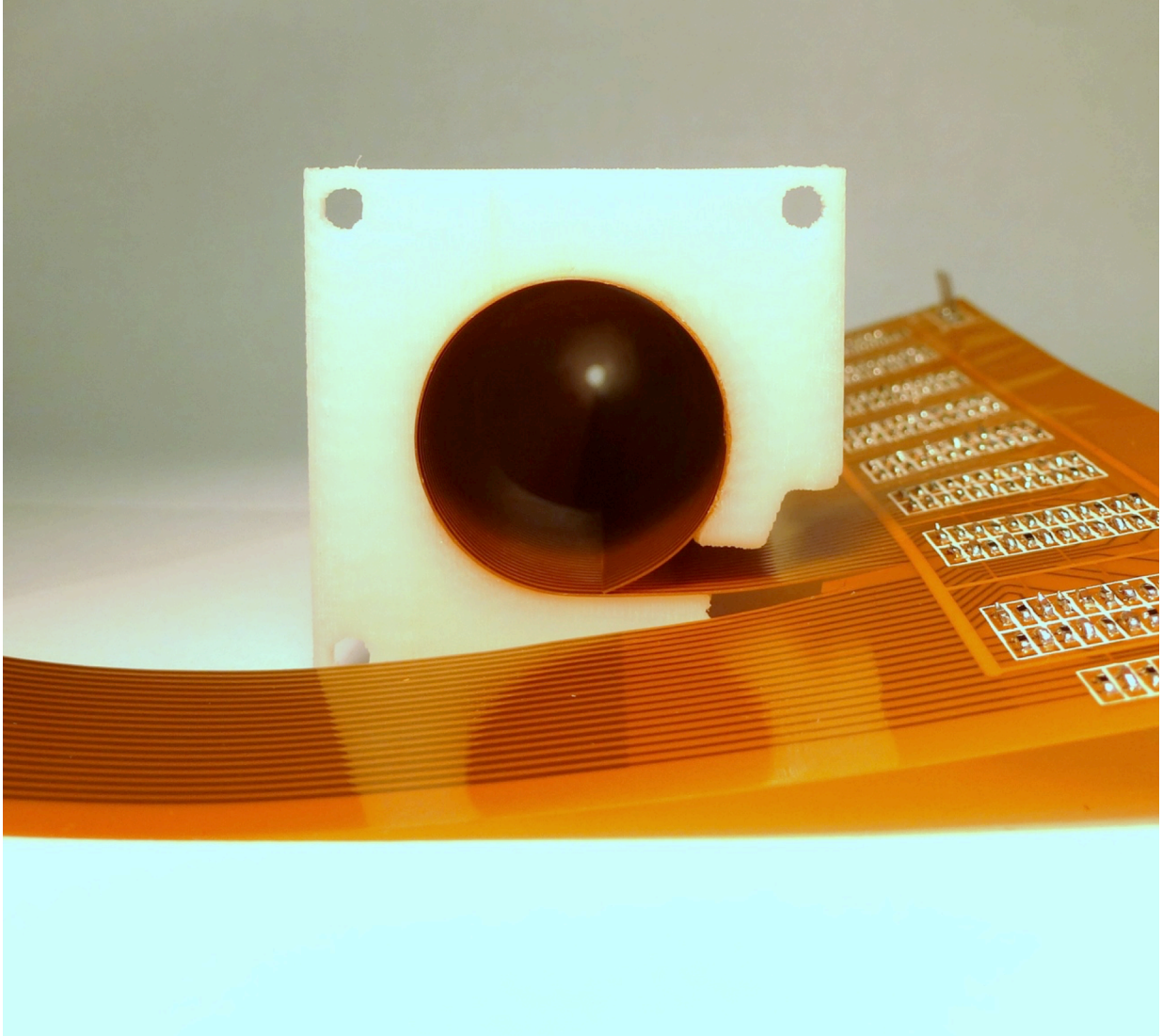
Figure 22 (continued)

via compression. A Viton gasket around the edge of the back plate is used to create an adequate seal between the two chambers. The orifice in the back plate was drilled out to a diameter slightly larger than the 2 mm extraction lens implemented on the flexible circuit board. This ensured that the extraction lens also serves as the mass conductance limiting orifice and interface between the first and second differential vacuum stages. The complete assembly is shown in Figure 23**.**

67
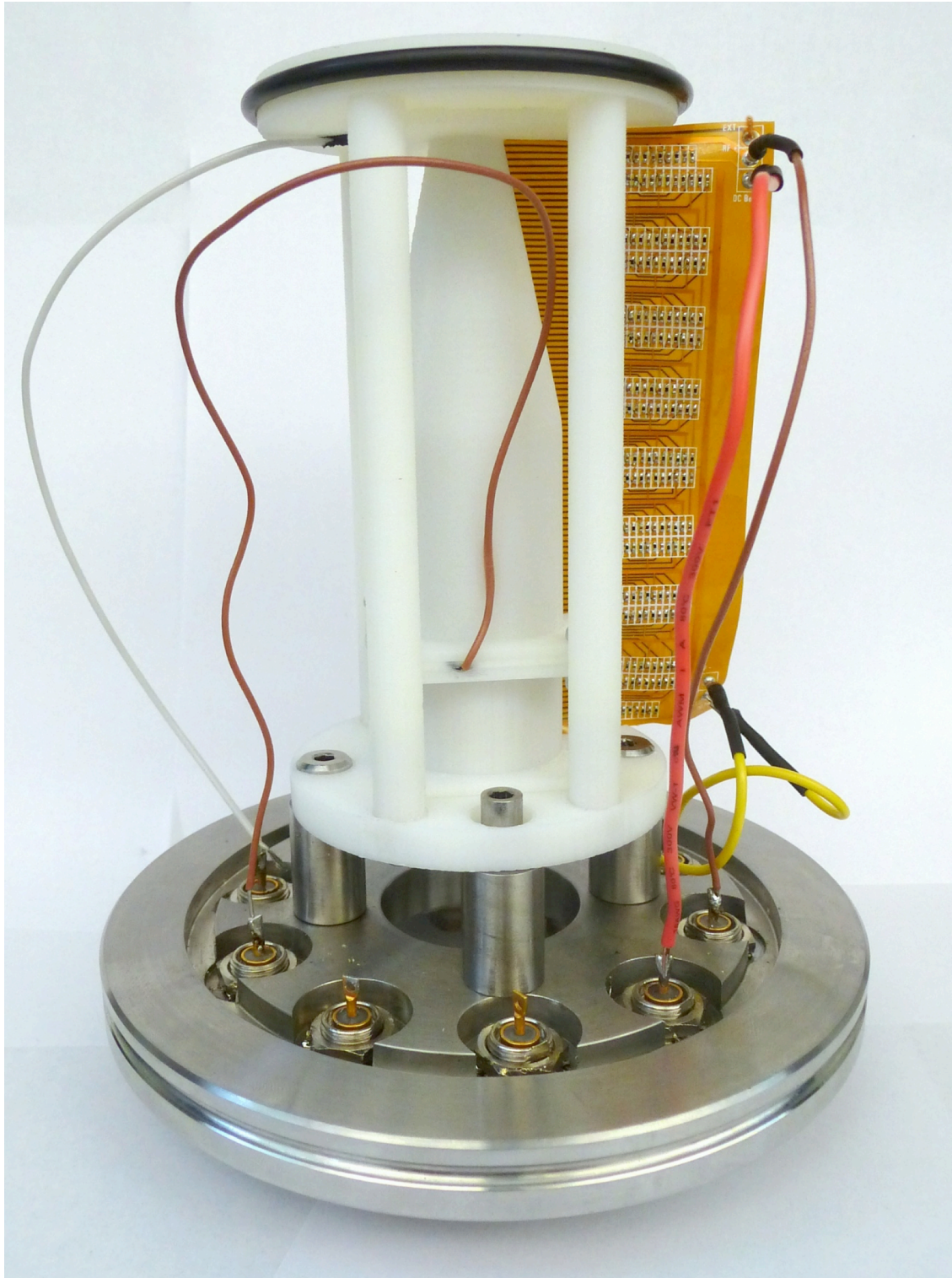
Figure 23: Assembled flexible board ion funnel, shown perpendicular to axis of the funnel. While focusing an ion cloud, ions will enter in through the bottom and exit from the top through the extraction lens.

The constant diameter section of the flexible ion funnel has a diameter of 20.4 mm. The electrodes are 0.5 mm wide and spaced 0.5 mm apart; the same spacing as the conventional funnel design. The jet disrupter electrode replaces the 20th and 21st electrodes and is made of a 6.3 mm diameter 3D printed ABS disk concentric to the ring electrodes and supported by four 1 mm wide beams. To make the jet disrupter conductive it was coated with conductive paint (CAIG CircuitWriter). The solder mask of the flexible printed circuit board was removed to expose the traces.

All ring electrodes, with the exception of the extraction lens, are connected in series by a chain of 510 kOhm resistors. The first and last electrodes on the resistor chain have DC potentials applied to them and are referred to as "funnel top" and "funnel bottom" respectively. The series resistor chain works as a DC voltage divider providing a linear DC voltage gradient to the electrodes along the funnel axis, forcing ions towards the extraction lens. The extraction lens is the last ring electrode. It has a 2 mm diameter and is biased by a separate DC voltage supply. Two 180º out of phase RF voltages are fed alternatingly into the electrode stack via 0.01 µF coupling capacitors. The combined effect of the RF and DC fields coupled with gas flow results in a focusing effect, forcing the ions towards the extraction lens and significantly increasing the ion transmission into the subsequent chamber. The conventional funnel has a resonant frequency near 600 kHz and a capacitance of approximately 2.7 nF. The flexible funnel has a greatly reduced capacitance of approximately 0.1 nF. Stainless steel plate electrodes have a large area of overlap, while traces on circuit board have a thickness of only about 0.035 mm (1 oz. copper/inch) resulting in a much smaller area of overlap, dramatically reducing the capacitance. In order to compare the funnels using the same

69

RF power supply with the same resonant frequency, a 2.6 nF capacitor was added in parallel with the RF signal inputs of the flexible funnel.

4.3.2 Experimental Procedure

The experiments were performed using a solution flow rate of 1 μL/min through a Hamilton needle serving as emitter. The needle was held at a potential of +1850 V relative to ground and at a 1 mm spatial separation from the capillary. The capillary was heated to 130ºC and held at a +210 V potential relative to ground. Electrospray stability was monitored using an optical microscope and a 532 nm laser illuminating the aerosol. The measured ion current is proportional to the number of ions generated during electrospray [12]. Therefore, the current can be used to measure the amount of material in the system. The current deposited on the ion funnel's electrodes, while unbiased, can be measured by electrically coupling all of the electrodes in the funnel and connecting them to a picoammeter. This yields an approximation of the total amount of current entering the system through the capillary. Current measurements were performed using a Keithley 6485 picoammeter. It is important to note that the measured current is composed of both gas-phase ions and droplets containing both ions and solvent. The total current exiting the funnel region was measured utilizing the rods and aperture plate of a quadrupole collision cell located in the second vacuum chamber of the setup. The current measured on the collision cell rods divided by the total ion funnel current yields a measure for the transmission efficiency of the ion funnel. This measurement protocol includes current contributions from both the injected ions as well as from solvent molecules. Although the solvent ions and charged droplets contribute to the total current entering the funnel, they cannot be focused and therefore

70

cannot contribute to the current out of the funnel. Presently, however, solute ion current and solvent ion and droplet current cannot be measured independently when sprayed from solution.

For the study two experiments were performed using each of the two funnels. In the first experiment the jet disrupter voltage was varied from 100V to 260V, while maintaining all other DC voltages and the RF amplitude at their optimized (for transmission) values. The conventional ion funnel has the highest transmission at DC voltages of 200 V funnel top, 175 V jet disrupter, 40 V funnel bottom, and 20 V extraction lens. The flexible ion funnel has slightly different optimized voltages due to the different mechanical design. They are 200 V funnel top, 160 V jet disrupter, 12.75V funnel bottom, and 9.5 V extraction lens. The second experiment varied the RF
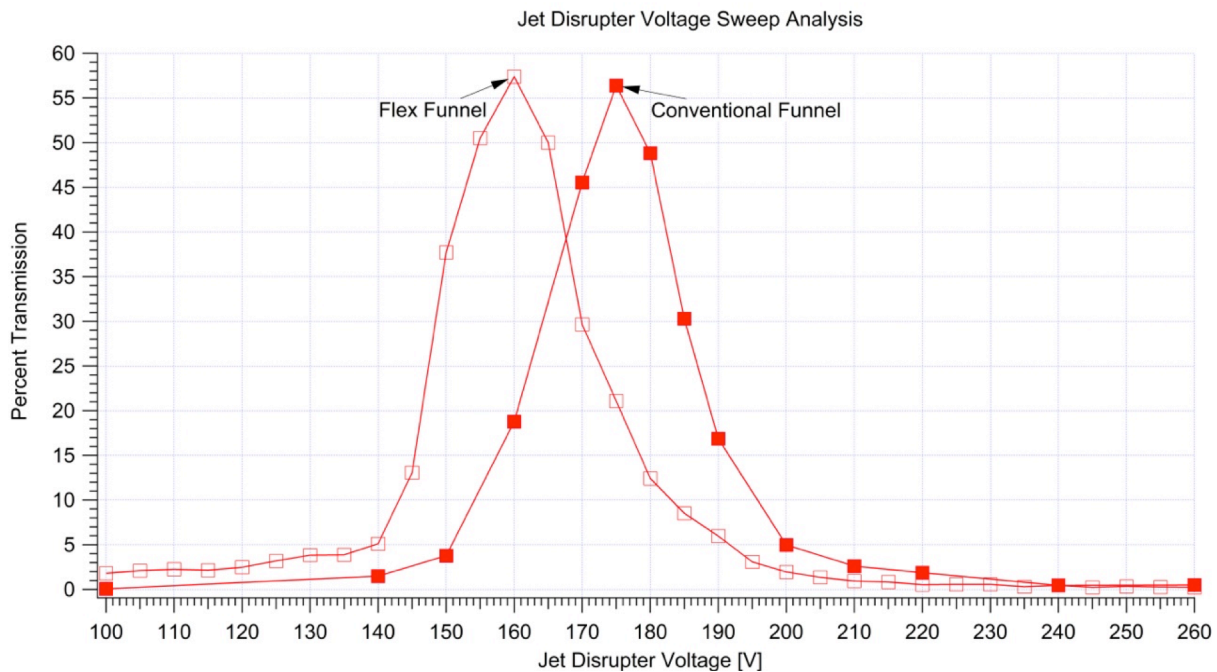
Figure 24: Ion transmission results as a function of the jet disrupter voltage. The maximum transmission for the flexible funnel (open symbols) is approximately 57% at 160 V while the conventional funnel reached 55% at 175 V (solid symbols).

71

amplitude of the applied signal while keeping all DC voltages constant at their optimized values. Varying the RF amplitude was accomplished by sweeping the DC driving voltage of the RF matching network circuit from 0 V to 7 V in increments of 0.25V resulting in RF Vpp values ranging from 0 Vpp to approximately 105 Vpp. The Vpp is measured as the maximum potential difference occurring between two adjacent electrodes during an RF cycle. In each experiment the transmission efficiency was measured as the parameter of interest (jet disrupter voltage or RF amplitude) was varied. The experiments were repeated several times to eliminate contributions of variations in the electrospray emission.

4.4 Results and Discussion

The results of the first experiments where the jet disrupter voltage was varied are shown in Figure 24, where the transmission efficiency is plotted as a function of the jet disrupter voltage for both the flexible board ion funnel and the conventional ion funnel. Both the flexible board ion funnel and the conventional funnel yielded transmissions of around 55% at jet disrupter voltages of 160 V and 175 V respectively. Both funnels have a maximum-transmission jet disrupter DC voltage that is approximately 5V higher than their adjacent electrodes agreeing with results given by Kim, et al. [19].

The graph shows that the curve shapes for the flexible and conventional ion transmissions are very similar, indicating an essentially identical behavior. The difference between the absolute voltage values are most likely a result of the slightly different geometries of the two funnels.

The transmission data of the second experiment where the RF drive voltage was varied are shown in Figure 25. This graph shows the transmission efficiency as a

72

function of RF peak-to-peak voltage (V_{pp}) for each funnel. The conventional funnel transmission reaches a maximum at approximately 60 Vpp and then remains constant with increasing amplitudes, likely due to unstable trajectories and fragmentation at higher RF amplitudes, and in agreement with results by Kim et al. [19]. The flexible board funnel on the other hand showed a transmission curve that did not peak in the covered amplitude range and continues to increase beyond 61%.

The reason for this difference in behavior may lie in the potentially higher gas pressures in the flexible board funnel. When the gas pressure within the electrode cavity
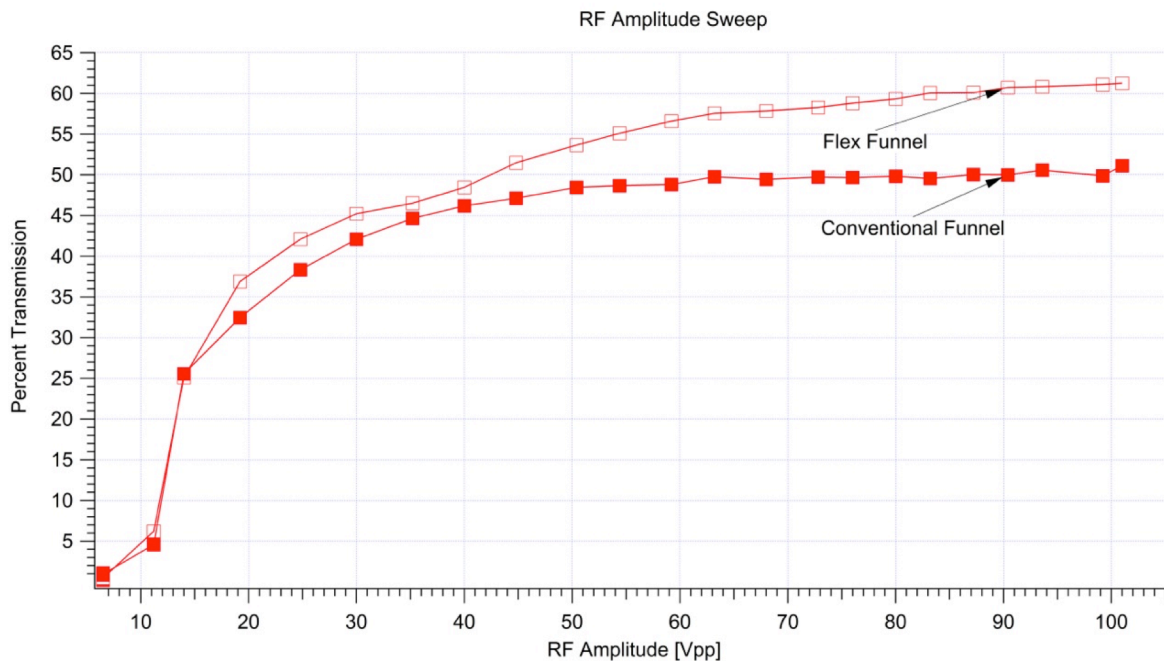
Figure 25: Ion transmission results as a function of RF amplitude. The flexible funnel (open symbols) transmits approximately 60% at approximately 90 Vpp, however it continues to increase with higher voltages at least up to the voltages tested. Pressures in the flexible ion funnel are thought to be higher and allow the RF to continually affect the transmission past 90 Vpp. The maximum transmission for the conventional funnel (solid symbols) is approximately 50% at approximately 60 Vpp and remains constant with increasing amplitude. The asymptotic behavior in transmission is due to unstable trajectories and fragmentation.

73

is higher the effectiveness of the RF potential is decreased, therefore requiring higher amplitudes to reach maximum efficiency. While the chamber pressure readings were similar for both funnels at about 1.9 Torr, the actual pressure within the flexible board funnel was most likely higher due to its closed construction. The pressure gauge was mounted on a flange protruding from the chamber. Because of this, these pressure readings do not reflect the actual pressure in the interior of the ring electrodes of the funnel since the capillary injects a gas stream directly into the funnel interior. This was considered by Shaffer et al. who used an ion funnel with Teflon sheets inserted between the electrodes resulting in a gas flow similar to the flexible ion funnel [18]. They estimated the pressure to be approximately 2 to 3 times higher in the funnel than the gauge reading. In contrast the conventional steel plate based ion funnel used in this study used Teflon washers between the plates, hence gas is able to escape the interior of the funnel through the space between the electrodes. As a result, it can be assumed that the pressure within the flexible board funnel was considerably higher than in the conventional funnel. This suggests that the maximum transmission of the flexible board funnel should occur at a higher voltage than in the conventional funnel, i.e. the maximum voltage was not yet reached in the covered V_{pp} range.

Because the base material of the flexible circuit board is nonconductive, ion transmission stability becomes a concern as a result of latent charge build-up. During the course of experimentation however, no degradation of the ion current was noted after four hours of continuous experiments recorded for this study in addition to extensive unrecorded trials. To date, the ion funnel has not required any special cleaning due to material build-up. After more extensive use however, cleaning by use

74

of an appropriate solvent may be necessary. Due to the smooth nature of the flexible printed circuit board, the exposed surface can be easily cleaned using a laboratory tissue or cotton swab.

4.5 Conclusion

An ion funnel design based on a flexible circuit board and a 3D printed scaffold has been demonstrated. The transmission behavior of the new design was compared with a conventional ion funnel built from a stack of machined steel plates. The experiments showed that the flexible board ion funnel achieved an ion transmission performance almost identical to that of the conventional ion funnel. The dependence of the transmission on the RF amplitude was somewhat different in the flexible board funnel design, most likely due to the different gas flow characteristics in this funnel due to the closed design of the internal funnel volume. This resulted in a higher pressure compared to the open design of the conventional funnel, which allowed a degree of gas conductance between the electrodes.

While performing with similar efficiency, the flexible board ion funnel offers several distinct advantages over the conventional funnel. Electrodes are made only of traces instead of plate electrodes, thereby reducing the area of overlap of the electrodes by several magnitudes. This strongly reduces the overall capacitance, increasing the device impedance while also dramatically reducing the total power consumption of the device. This raises the prospect of low-power ion funnel devices for battery operated mobile applications such as on-location hazardous material detection. Another benefit is that potentially very narrow and closely spaced electrodes could be implemented. According to Gerlich, as the inter-electrode spacing is reduced, the effective focusing

75

potential is increased [85]. This would additionally reduce the power demand of the device.

Another advantage of the flexible board based funnel is the cost of manufacture. The use of flexible circuit board technology in combination with the 3D printed support structure allows for a significantly simplified construction procedure. This results in a total cost that is approximately one magnitude lower than that for the conventional design while maintaining the ion transmission performance of the device. Additionally, the use of these materials significantly reduces the device weight, further lending itself to use in mobile applications.

4.6 Acknowledgments

CHAPTER 5: SEALING FDM COMPONENTS FOR VACUUM APPLICATIONS USING ELECTROPLATING[3]

5.1 Abstract

The use of electroplating as a post-processing technique for FDM-fabricated components was demonstrated for applications in high-vacuum technology. Copper and nickel electroplating were performed and the hermacity of the samples was tested under high-vacuum. Samples with total thicknesses of 8.0, 13.0, 25.4, and 49.2 μm were produced. The two samples with the thinnest plating buckled under the forces required to seal them using standard vacuum fittings from atmosphere. Thicker samples withstood the stresses and were completely impervious to helium. A proof-of-concept component (KF 25 full nipple) was processed and tested on the system. High-vacuum was achieved however, due to the extensive processing in aqueous environments water was a major contaminant through adsorption and limited the ultimate achievable pressure.

5.2 Introduction

Rapid prototyping using Fused Deposition Modeling (FDM) has become a useful fabrication technique due to its low-cost and ability to generate organic shapes too difficult for traditional manufacturing methods [46]. FDM parts used as sealed pressure or vacuum vessels are intriguing due to the lightweight and low-cost nature of the

---

[3] This chapter has been submitted to the journal "Additive Manufacturing" and is awaiting review.

material and ease of customizability of the parts produced. However, this topic has only been investigated by a small number of researchers, and only while using the parts produced as positive internally pressurized vessels [5, 57, 58]. The use of electroplating to seal FDM parts and utilize them as high-vacuum vessels has yet to be investigated and is the focus of this study. The hermacity of electroplated components was systematically investigated and a proof-of-concept vacuum component was constructed and tested.

It is well documented that gasses easily diffuse through most polymers [86] and are generally impermeable to most metals [24]. Because of the impermeability of most metals, metallization of polymers is applied in various industries including food and medical packaging [87] and vacuum insulation paneling [88] where the diffusion of gasses through polymers is undesirable. During its 20-year serviceable lifetime, vacuum insulation paneling is expected to maintain a pressure of below 7.5×10^{-2} Torr. Although 7.5×10^{-2} Torr is two orders of magnitude above high-vacuum (approximately 7.5×10^{-4} Torr), this demonstrates the use of metalized polymers in maintaining vacuum over long periods of time.

Parts fabricated using FDM are generally thermoplastic materials, commonly the co-polymer acrylonitrile-butadiene-styrene (ABS). FDM parts as pressurized vessels produced using ABS are limited due to holes in as-printed, unprocessed parts. The incomplete fusion of all adjacent extrusion roads results in the formation of pores during the deposition process, which readily allow air and other gasses to pass through.

Other groups have demonstrated the holes in the FDM parts can be effectively sealed using appropriate processing methods for cosmetic and functional uses.

78

Stratasys suggests two methods of sealing FDM parts fabricated with ABS: their proprietary "Finishing Touch Smoothing Station" or a brief soak in a solvent such as dichloromethane or acetone. These methods are only appropriate for lower pressure applications and are generally used for cosmetic purposes in order to reduce the surface roughness of the parts [56]. Epoxy injection into the internal cavities of FDM parts has been successfully implemented as a strength increasing and permeability reducing processing technique [58]. McCullough et al. explored the use of FDM parts for microfluidic applications [57]. To be an effective microfluidic device, a part produced by FDM needs to be impermeable to water. In their study, samples were soaked in various acetone-water mixtures for up to 48 hours. The use of a co-solvent with acetone effectively sealed gaps between the extrusion roads while still maintaining critical part features and dimensions. Samples that previously drew water into the gaps between extrusion roads were effectively rendered impervious after processing. Mirales et al. analyzed several methods for sealing FDM parts using various sealants and epoxies applied to the surface or drawn into the structure via vacuum infiltration. Internal pressures up to approximately 276 kPa (2145 Torr) were observed in the best performing samples [5].

Vacuum vessels are generally cylindrical or spherical. The hoop stress experienced by a thin-walled cylindrical vacuum vessel is described by the hoop stress equation:

$$\sigma_h = \frac{\Delta P \cdot R_m}{t}$$

and for a spherical vacuum vessel:

$$\sigma_h = \frac{\Delta P \cdot R_m}{2t}$$

79

where σ_h is the hoop stress, ΔP is the pressure difference, R_m is the mean radius of the vessel, and t is the vessel wall thickness. Ahn et al. [52] cites the compressive strength of FDM fabricated ABS in the 30 to 40 MPa range, depending on extrusion raster orientation. Using the value of one atmosphere (101325 Pa or 760 Torr) as the pressure difference in these equations shows even when applying very large safety factors, FDM offers the opportunity to generate vacuum vessels of useful dimensions. Additionally, it has been shown additively manufactured parts that have been electroplated exhibit much higher strength than their unplated counterparts [89, 90].

5.3 Methods and Materials

All FDM samples in this study were produced on a Stratasys uPrint SE Plus extruding the ABSPlus P430 polymer. ABSPlus P430 is a co-polymer mixture of 70 - 75% ABS and methyl methacrylate (MMA) co-polymer and 25 – 30% styrene-acylonitrile (SAN) co-polymer [91].

To test the ability of electroplating to seal an FDM component, the part must be processed using several chemical baths. However, typically FDM parts are not fully sealed and contain numerous pores on the surface and voids within the part. Chemical residues from previous steps can seep into these spaces and have a detrimental effect on subsequent steps. Therefore, the first step in processing the parts is to seal them. This is done using one or more 15 second dips in dichloromethane [56]. After soaking, samples are air dried for at least 18 hours in order to ensure adequate evaporation of all volatile residues.

ABS is one of the most commonly plated plastics due to its ability to be etched, producing a micro-roughened surface. The etchant is a mixture of concentrated sulfuric

80

acid and chromic acid. Adhesion of autocatalytically deposited metal films onto the polymer surface after etching is greatly enhanced when compared to unetched ABS. Samples were etched in the chromic acid/sulfuric acid mixture for 10 minutes at 60 ºC and subsequently washed in deionized water. After rinsing, samples were soaked in a sodium bisulfite solution in order to reduce any remaining hexavalent chromium from the etching procedure [66].

Both electroless and electroplating were performed using commercially purchased kits (Caswell Plating, Lyons, NY). Autocatalytic silver, in the form of Tollen's Reagent was used to render the plastic conducive prior to electroplating. For copper electroplating an acid copper sulfate formulation was used for the bath. A Watts formulation was used for the nickel plating [60].

Adhesion of the autocatalytic silver was performed using the "Scotch Tape test" as described in ASTM D3359b using Type 810 Scotch Tape. In this test a grid of lines spaced approximately 1 mm apart are cut in to the surface of the film using a razor blade. Then, a piece of pressure sensitive tape is placed on the surface of the film over this grid. The tape is then removed at a 180° angle. The amount of material removed from the surface serves as a qualitative comparison between two films.

A complete processing procedure for preparing the electroplated samples is as follows:

1. One or more dichloromethane soaks for 15 seconds each

2. Drying in atmosphere for at least 18 hours

3. Chromic acid/sulfuric acid etch for 10 minutes at 60 ºC

4. Sodium bisulfite solution soak for 10 minutes at room temperature

81

5. Autocatalytic silver deposition

6. Drying in atmosphere for 1 hour

7. Degreaser soak for 5 minutes at 60 ºC

8. Electroplating with copper or nickel
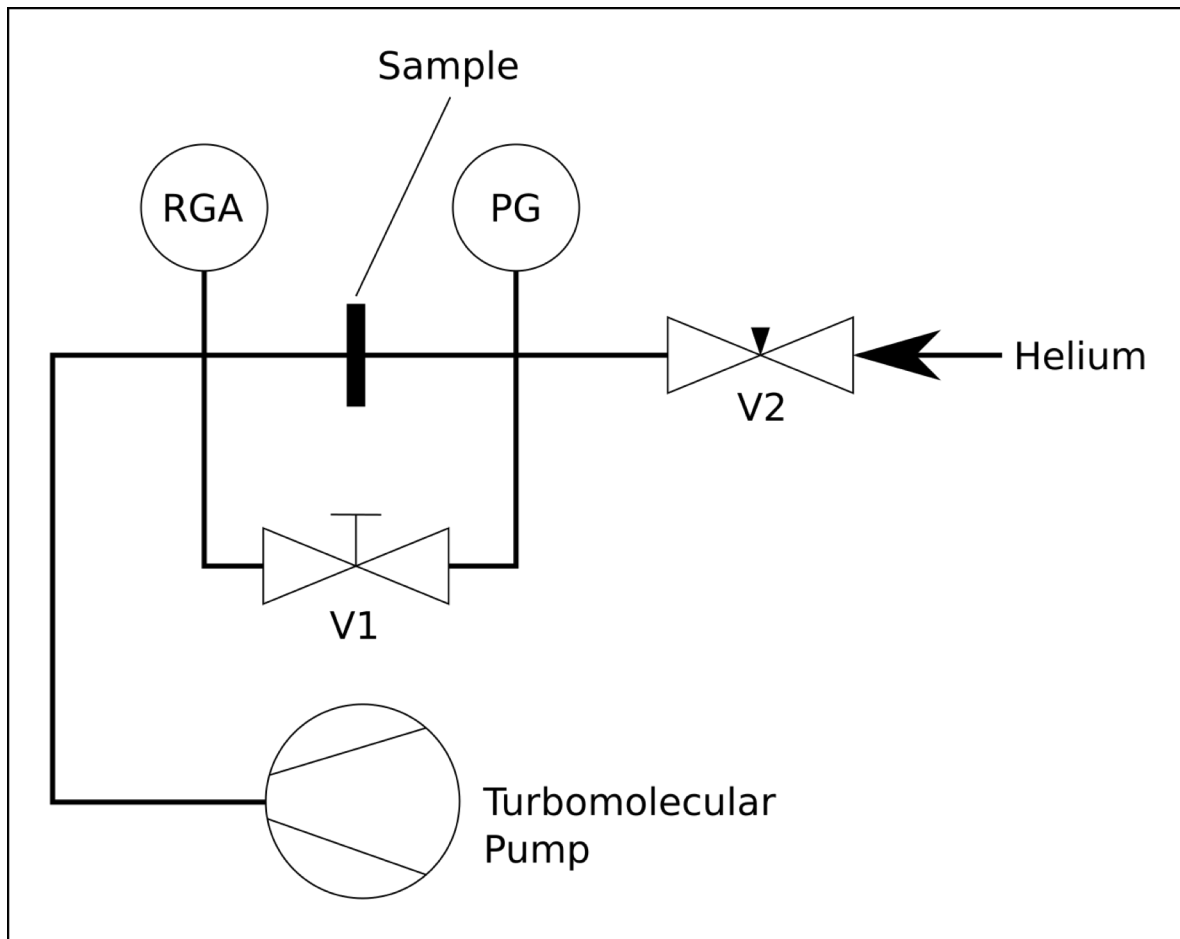
Figure 26: Vacuum system diagram showing Helium input, pressure gauge (PG), and residual gas analyzer (RGA).

To test the hermacity of the electroplated samples, parts were placed into the vacuum chamber setup shown in Figure 26 and similar in design to [88]. Samples were placed in between two 2.75" CF flanges. With V2 closed, valve V1 was opened and the system pumped to its ultimate pressure (5×10^{-7} Torr). V1 was then closed and V2 opened,

allowing a fixed amount of helium to flow in to the volume adjacent to the sample. During this time, the residual gas analyzer (RGA-300 Stanford Research Systems, Sunnyvale, CA) continuously monitored the partial pressure of helium. The RGA has a minimum detectable partial pressure of 5×10^{-14} Torr. The RGA continued to monitor the helium partial pressure for a period of 20 hours to ensure that there were not any low conductance leaks.
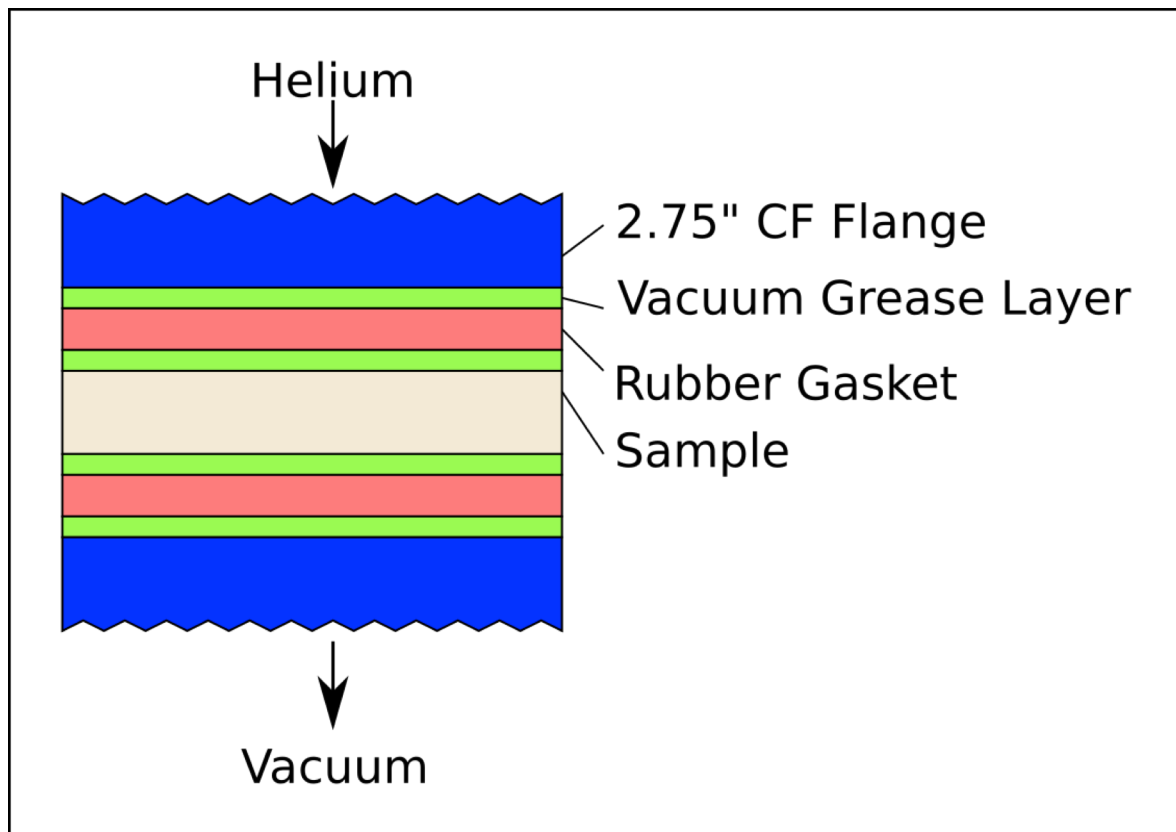
Figure 27: Sample arrangement for measurement of permeation.

Hermacity test samples are sealed against atmosphere using the arrangement shown in Figure 27. In place of standard copper gaskets, flat rubber gaskets were substituted. A layer of vacuum grease was placed between both the sample and flanges and the rubber gaskets. To ensure that a proper seal was established, a leak

83

test was performed using the RGA and a stream of helium directed toward the sample from an atmospheric pressure source.

5.4 Results and Discussion

5.4.1 Film Properties
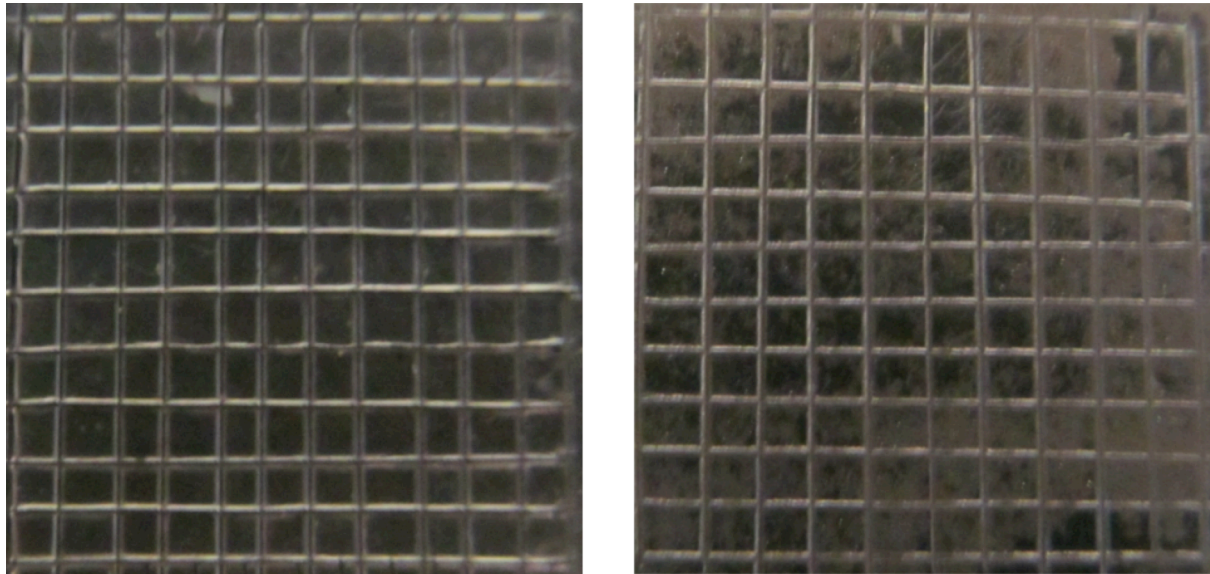
Figure 28: Results of the "Scotch Tape" adhesion test performed on the autocatalytic silver films. The etched sample is shown on the left, the unetched sample is shown on the right. Significant removal of the silver is observed on the unetched sample.

Adhesion of the autocatalytic silver was assessed using the "Scotch Tape test". Etched and unetched samples were produced in order to determine the effect of the chromic acid etching on the film adhesion. Both samples were sealed using a single 15-second dichloromethane soak. One sample was etched using the chromic acid solution, then both samples were coated using autocatalytic silver. Results of the test are shown in . The unetched sample shows significant removal of the silver film, indicating poor adhesion. In the etched sample, however, no material was removed after performing the test.
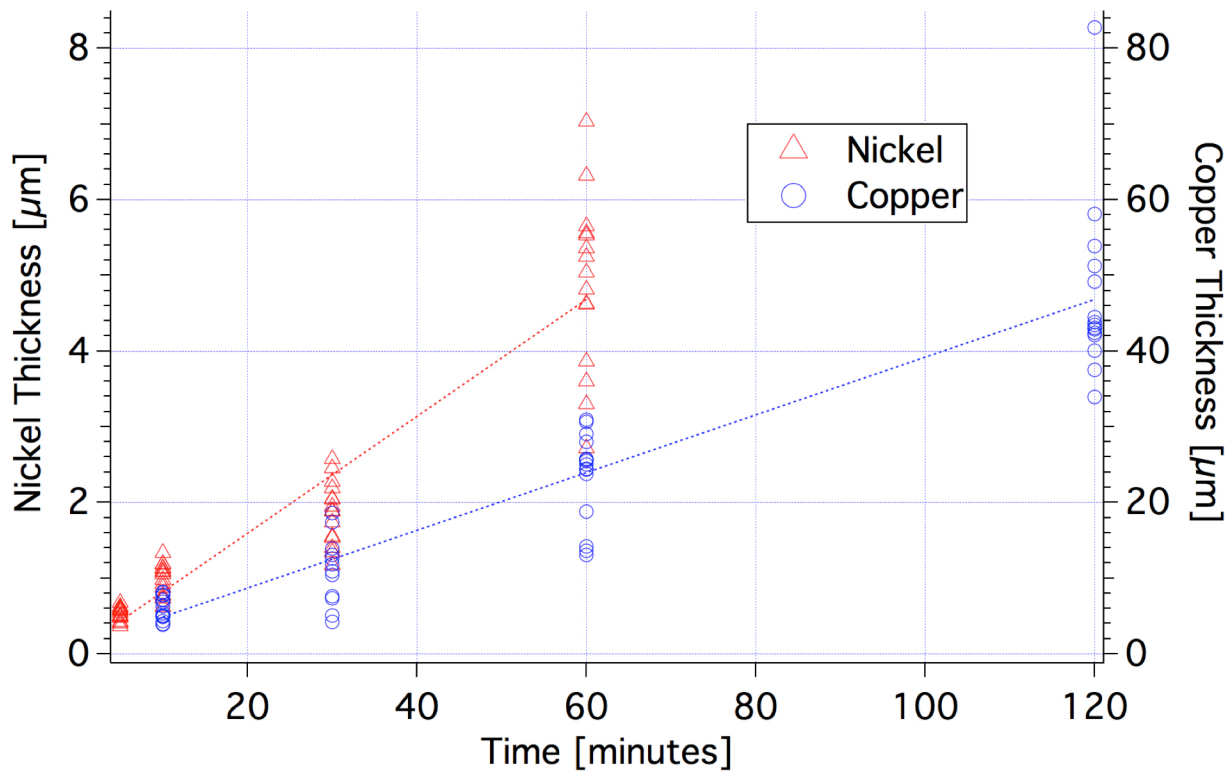
Figure 29: Thickness measurements of the nickel and copper electroplated films. Copper samples were deposited for 10, 30, 60, and 120 minutes and nickel films for 5, 10, 30, and 60 minutes.

Hexavalent chromium in the etchant solution is an extremely strong oxidizer that selectively oxidizes and removes the butadiene phase of the ABS. This results in a micro-roughened surface with voids that provide a location to attach the subsequently deposited film and improve mechanical adhesion. This etching process is most often used with autocatalytic nickel, however the results of this test show that the etching process is also beneficial for increasing the adhesion of autocatalytic silver.

Figure 29 shows the results of the measurements of the film thicknesses for both the copper and nickel-electroplated films deposited for various lengths of time. Samples were prepared according to the protocol listed above. For copper, deposition times of 10, 30, 60, and 120 minutes were performed using a current density of 3.25 A/dm^2.

85
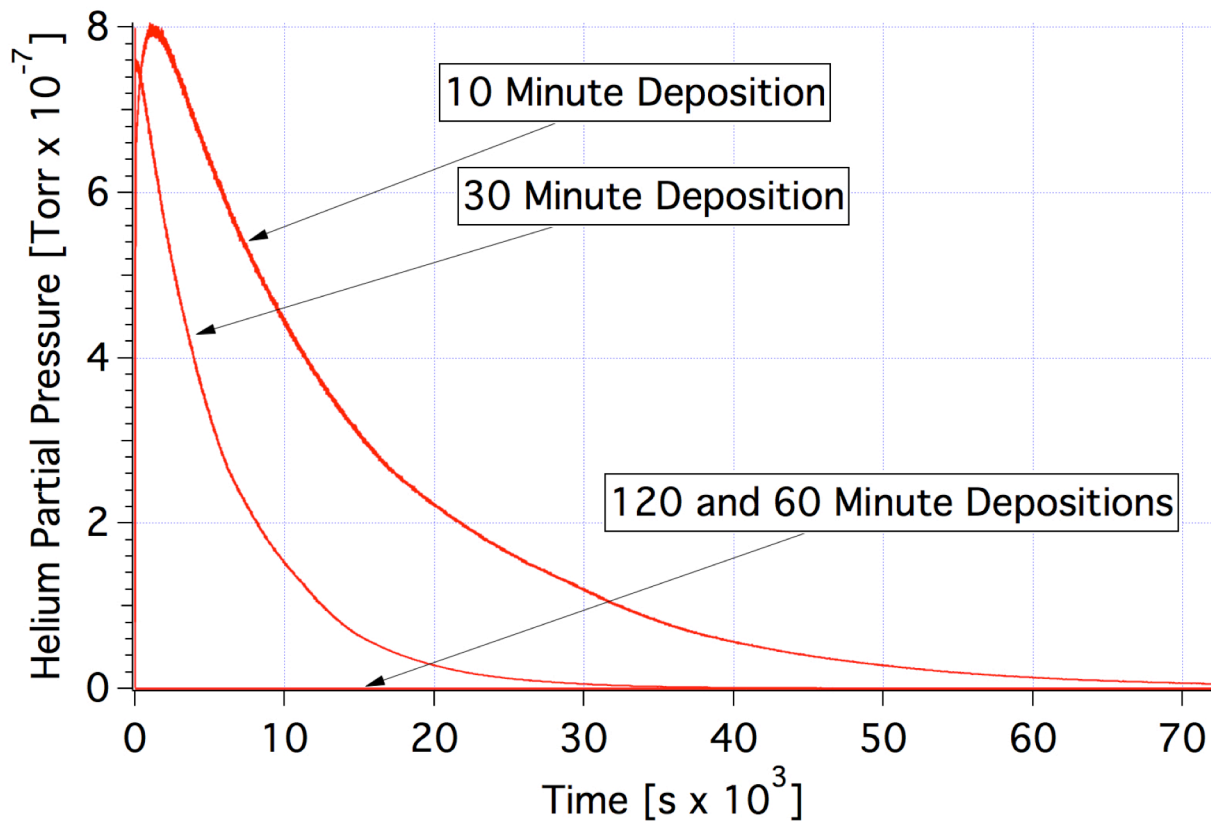
Figure 30: Results of the hermacity tests of electroplated samples. The times shown indicate the copper deposition time. Nickel deposition time was held constant at 30 minutes. The 120 and 60-minute depositions are at the baseline level of helium for the system (approximately 1×10^{-11} Torr).

This current density was chosen in order to maintain a densely packed film, while decreasing the deposition time. For the nickel electroplating a current density of 1 A/dm^2 was used to generate a smooth, dense film [60]. Nickel was deposited for 5, 10, 30, and 60 minutes.

Average thicknesses for the copper samples were 6.1, 11.1, 23.5, and 47.3 µm for the 10, 30, 60, and 120-minute depositions respectively. The nickel samples had average thicknesses of 0.53, 1.0, 1.9, and 4.9 µm for 5, 10, 30, and 60-minute depositions respectively. The deposition of the nickel film helps improve the corrosion

86

resistance of the components [60]. A nickel deposition time of 30 minutes was chosen for all hermacity and proof-of-concept samples.

5.4.2 Hermacity Test Results

For hermacity testing, circular, 48.1 mm diameter, 5 mm thick samples were printed. The diameters of the disks are the same as a Conflat 2.75" copper gasket. The samples were printed using a solid infill to minimize the amount of residual air trapped within the structure. The samples were sealed, etched, and electrolessly plated using the process mentioned earlier. The electroplating process consisted of first plating using the acid copper sulfate for various plating times, then plating with nickel for 30 minutes. Current densities for the copper and nickel were 3.25 A/dm^2 and 1 A/dm^2 respectively. The resulting total film thicknesses were estimated to be 8.0, 13.0, 25.4, and 49.2 μm for the 10, 30, 60, and 120 minute copper depositions respectively. After the addition of helium to the high-pressure side of the apparatus, the partial pressure of helium was monitored on the low-pressure side for 20 hours. The results of these experiments are show in Figure 30. These results are similar to those found in previous studies where low-conductance leaks though metalized polymer films were analyzed [88]. The failure of the 10 and 30-minute deposition samples is a result of cracking, delamination, and buckling at the interface between the polymer substrate and metal film. The decay of the helium partial pressure over time is a result of the depletion from the high-pressure side of the apparatus through the defects in the sample. The formation of the delaminated regions was a result of attaching the samples to the vacuum chamber, as high stresses are applied when tightening the gasket seals around the part in order to ensure proper sealing of the sample from atmosphere. These

stresses put the film in to compression parallel to its surface. In the presence of an internal delamination defect at the metal/polymer interface, a blister will form once a critical stress, whose value is proportional the film thickness squared, is reached [92]. These blisters can propagate and create "tunnels" through which the helium can pass.

5.4.3 Proof of Concept Device

For a final proof-of-concept an ISO KF 25 full nipple, a typical vacuum component, was constructed using the methods described in this study. A 3D rendering
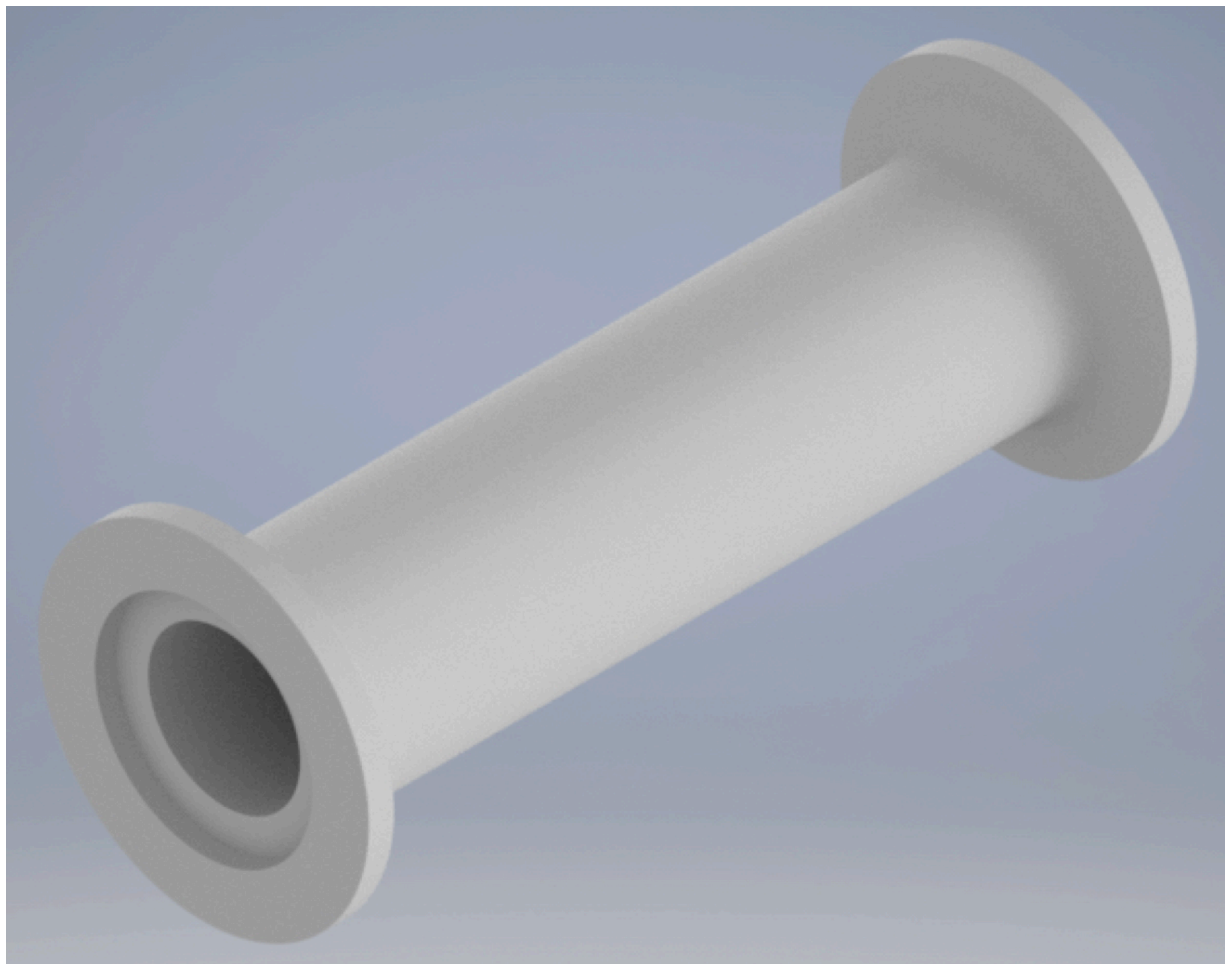
Figure 31: Computer rendering of the proof-of-concept component (top) and image of component connected to the vacuum system (bottom).
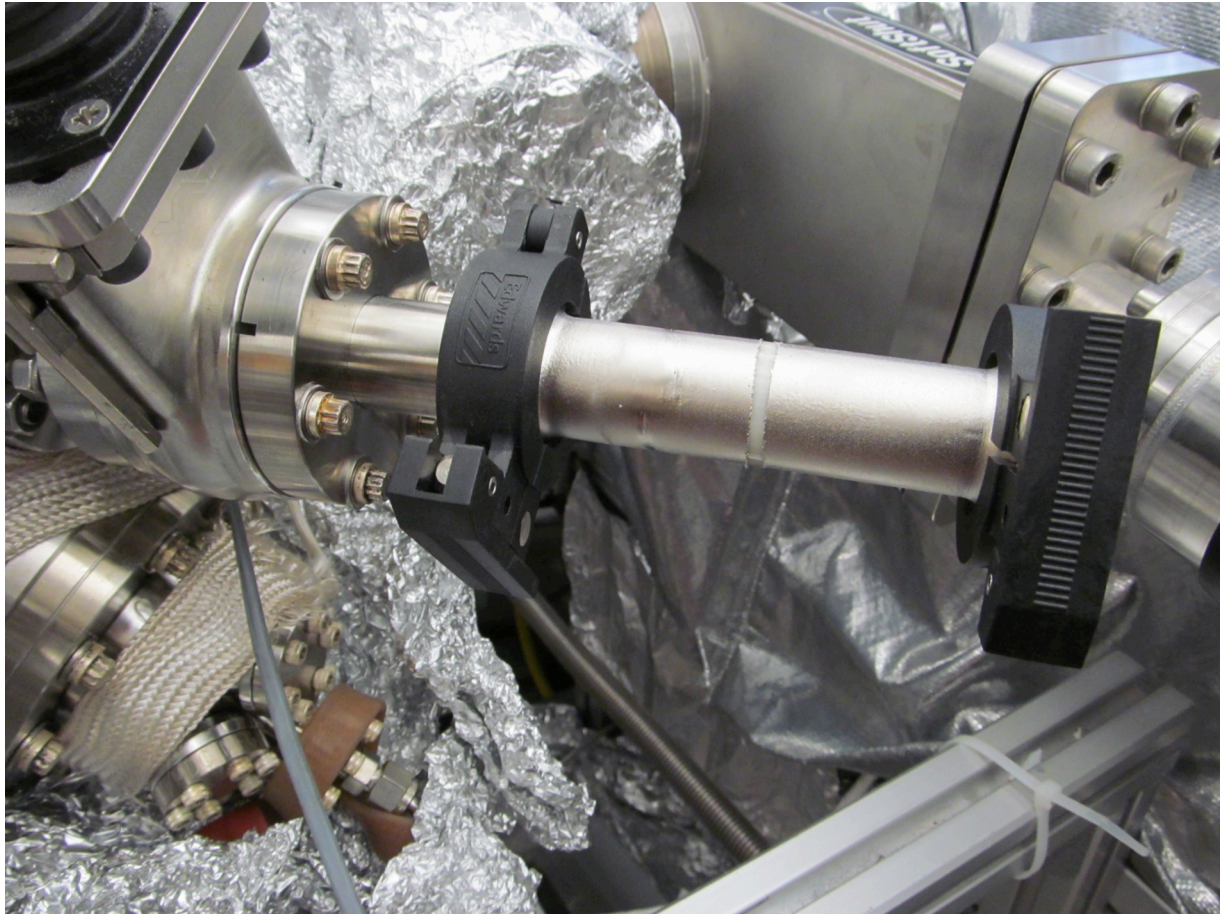
Figure 31 (continued)

of the component as well as an image of it connected to the vacuum system is show in

Figure 31. Slight modifications to the processing procedure were necessary to produce

the final product.   First, in order to adequately seal the component, three

dichloromethane dips were necessary as opposed to the single dip used for the

hermacity test components. Initial attempts using only a single dip produced a part with

many unsealed pores. It is believed these pores are the result of air bubbles trapped on

the surface of the part by surface tension. Where a bubble is present, solvent will not

contact the polymer surface and not adequately dissolve the material at that point. The

result was an appreciable amount of etchant solution was absorbed into the component,

rendering the subsequent step of electroless plating ineffective. The presence of corners and more complex geometric features is believed to have introduced void producing bubbles on the surface, necessitating the further processing. Second, for the electroplating procedure, a conforming internal anode, called a stringer, was used in addition to the regular anodes of the plating bath. The purpose of this extra anode was to ensure the internal surface of the nipple was adequately plated. For this sample, copper plating was performed for 120 minutes and nickel plating for 30 minutes.

After attaching the nipple to the vacuum chamber, the gate valve separating it from the low-pressure side was slowly opened. A sharp total pressure rise was observed, increasing from the mid 10^{-7} Torr range in to the high 10^{-5} Torr range. A leak test using helium was performed on the sample confirming that it was sealed from atmosphere. Using the RGA, the partial pressure of water was monitored and it was observed to be the primary contaminant causing the increase in pressure. The sample was allowed to remain under vacuum for approximately 48 hours where it was observed the partial pressure of water was continuously reduced. The total pressure within the system also continuously fell, albeit at an exponentially slowing rate. With stainless steel vacuum chambers, a contamination-free environment is produced by heating the chamber to 150 ºC under vacuum to desorb any volatile substances on the chamber walls [24]. Because the glass transition temperature of ABS is around 108 ºC [93], an increase to this temperature is impractical. The desorption rate of gasses from surfaces under vacuum exhibit an exponential dependence on temperature, however, indicating that even a modest increase in the temperature of the system will result in a significant

90

increase in the rate of desorption and reduction in time needed to reach the ultimate pressure of the system.

5.5 Conclusion

Electroplated FDM parts were tested for hermacity and applicability as vacuum components. Samples were successfully sealed using the electroless and electroplating protocol outlined in the study. The ability to withstand the forces encountered for proper sealing using conventional vacuum equipment is a necessary requirement of any component produced by this method. The samples with thinner films (approximately 8.0 and 13.0 µm) were not able to withstand these forces and buckled, resulting in helium conduction through the samples.

The proof-of-concept component successfully reached high-vacuum, however, the presence of a large amount of water contamination limited the system's performance. The various aqueous baths used to process the part introduced it to greater than normal concentrations of water, causing higher adsorption than standard stainless steel parts exposed only to atmospheric humidity. The processing methods, in combination with the inability to adequately heat the part to the most effective bake-out temperature, limits the ultimate usable pressures under which components processed in this way can perform.

The use of FDM-fabricated components for vacuum applications has been successfully demonstrated. As with all rapid prototyping techniques, this process allows for the quick turnaround from concept to functional vacuum component. Additionally, components can be completely customized and are not limited by standard machining and welding techniques. Their lower weight and low cost are additional benefits over

traditional stainless steel vacuum components. Further work should be done to investigate how parts encapsulated using electroplating could perform as electrodes or other in-vacuum components.

5.6 Acknowledgments

CHAPTER 6: CONCLUSIONS AND FUTURE WORK

The combination of the numerical solution of the fluid flow within the ion funnel chamber with electrodynamics simulations of SIMION provided a more accurate portrayal of the physical system when compared to previous studies. Although qualitatively accurate, these other models did not quantitatively predict the transmission of the ions through the system. Variation of the simulated jet disrupter voltage accurately predicted the ion transmission values when compared to the experimental device.

The increasingly popular use of atmospheric ion sources in analytical scientific equipment requires the accurate modeling of ion-gas interactions. Techniques such as atmospheric pressure chemical ionization (APCI), atmospheric pressure photoionization (APPI), and atmospheric pressure matrix assisted laser desorption ionization (AP-MALDI) all generate ions at atmospheric conditions then inject them into differential pumping systems. The simulation method outlined in this study could be applied to these techniques in order to further verify its function in accurately prediction transmission.

Using FDM and flexible printed circuit board technology an ion funnel, which performed to the same ion transmission standards as the traditional design, was produced. The traditional design, which consisted of a series of stacked stainless steel ring electrodes, was expensive to machine, time consuming to construct, and weighed

93

significantly more than the novel design. Although there were slight variations with regard to the performance of the novel device while varying the RF voltage amplitude applied to the lenses, this can most likely be explained by lack of gas flow through the lenses, which is experienced by the traditional design. Variation of the jet disrupter voltage produced curves of nearly identical shape, with differences attributable to the variation of funnel entrance DC voltages. The jet disrupter voltage at which maximum transmission was observed was approximately 5 volts higher than adjacent electrodes' DC potentials, in agreement with the literature.

The main source of impedance within the circuit that drives the ion funnel is the intrinsic capacitance of the device. Because the traditional design consists of a series of parallel plates the capacitance is much higher than that of the novel design. The lenses, which essentially form parallel plate capacitors, have been reduced in size in the novel model resulting in a much lower capacitance. The result is less power consumption and the ability to easily produce a much higher RF amplitude.

The strength of the focusing field generated by the ion funnel is a function of how closely spaced the lenses are, with closer spacing resulting in a stronger field. With the traditional design of the funnel, the width of the parallel plate electrodes limits the spacing of the electrodes. Using the flexible printed circuit board however, the traces can be produced extremely thin and in extremely close proximity. This would allow for some novel ion funnel designs with double or triple the number of electrodes without much penalty to device construction and while maintaining the same form factor.

The most important work to be done to further the use of this technology would be to test the performance of the device as part of a mass spectrometry setup. The

data obtained in the present study only measured the output current, which gave no indication of the condition of the ions it was transmitting. Connecting this to a system that contained a quadrupole mass filter or a triple quadrupole filter/fragmenter/filter setup would allow for the characterization of the device for use as an analytical instrument.

Using FDM to produce a vacuum chamber was realized through electroless and electroplating of the component. The hermacity of electroplated FDM components was tested by generating samples with various plate thicknesses and placing them in a system with relatively high pressure helium on one side and vacuum on the other. The helium peak was monitored using an RGA. The thinner plated samples were unable to withstand the mechanical forces required to seal the components to the vacuum system and failed. The thicker plated samples were able to successfully seal the part from the high-pressure side. A proof of concept vacuum component was produced which was pumped to 10^{-6} Torr. The ultimate pressure could have been improved with the ability to bake the component. Because the fabrication material used was ABS polymer, which has a relatively low glass transition temperature, a bake-out was not practical.

Electroless plating was used in this study to generate the conductive layer for later electroplating, however, electroless plating can also be used to produce a hermetic seal. Electroless nickel can be deposited in layers several micrometers thick. This has been demonstrated using parts produced by additive manufacturing [94]. Using this technique, more complex components with organically shaped internal cavities and blind recesses could be easily plated. Additionally, this would reduce the number of processing steps by removing the need to electroplate.

95

An interesting extension of the studies here would be to combine the novel ion funnel design and a vacuum chamber produced using FDM to make a polymer-based ion injection system. This system would cost a fraction of the price of the original design and be significantly less massive than its stainless steel counterpart. The use of polymer components in vacuum systems could be a way to produce mobile instruments in the future for in-field analysis of unknown chemicals toxic agents.

To overcome the inability to bake out the material, the base material for the chamber could be produced using the higher temperature material Ultem (polyetherimide). This material can be used in commercially available FDM devices and has a glass transition temperature of 186 ºC [95]. A modest increase in the temperature significantly reduces the desorption time of water from surfaces. Using Ultem would allow for a modest bake-out and the ability to reach much lower ultimate pressures.

REFERENCES

1. Tridas, E.M., Anthony, J.M., Guldiken, R., and Schlaf, R., *Enhanced simulation of an RF ion funnel including gas turbulence.* Journal of Mass Spectrometry, 2015. **50**(1): p. 206-211.

2. Moskovets, E., *Ghost peaks observed after atmospheric pressure matrix-assisted laser desorption/ionization experiments may disclose new ionization mechanism of matrix-assisted hypersonic velocity impact ionization.* Rapid Communications in Mass Spectrometry, 2015. **29**(16): p. 1501-1512.

3. Gimelshein, S., Lilly, T., and Moskovets, E., *Numerical Analysis of Ion-Funnel Transmission Efficiency in an API-MS System with a Continuum/Microscopic Approach.* Journal of The American Society for Mass Spectrometry, 2015: p. 1-12.

4. Tridas, E.M., Allemang, C., Mast, F., Anthony, J.M., and Schlaf, R., *High transmission 3D printed flex-PCB-based ion funnel.* Journal of Mass Spectrometry, 2015. **50**(7): p. 938-943.

5. Mireles, J., Adame, A., Espalin, D., Medina, F., Winker, R., Hoppe, T., Zinniel, B., and Wicker, R., *Analysis of sealing methods for FDM-fabricated parts*. 2011, University of Texas El Paso.

6.   Dole, M., Mack, L.L., Hines, R.L., Mobley, R.C., Ferguson, L.D., and Alice, M.B., *Molecular Beams of Macroions.* The Journal of Chemical Physics, 1968. **49**(5): p. 2240-2249.

7.   Fenn, J., Mann, M., Meng, C., Wong, S., and Whitehouse, C., *Electrospray ionization for mass spectrometry of large biomolecules.* Science, 1989. **246**(4926): p. 64-71.

8.   Lyon, J.E., Cascio, A.J., Beerbom, M.M., Schlaf, R., Zhu, Y., and Jenekhe, S.A., *Photoemission study of the poly(3-hexylthiophene)/Au interface.* Applied Physics Letters, 2006. **88**(22): p. -.

9.   Wang, W., Alsmeier, J.H., Wolak, M., and Schlaf, R., *Determination of the charge neutrality level of poly(3-hexylthiophene).* The Journal of Chemical Physics, 2013. **138**(5): p. -.

10.   Li, Z., Berger, H., Okamoto, K., Zhang, Q., Luscombe, C.K., Cao, G., and Schlaf, R., *Measurement of the Internal Orbital Alignment of Oligothiophene-TiO2 Nanoparticle Hybrids.* The Journal of Physical Chemistry C, 2013. **117**(27): p. 13961-13970.

11.   Morozov, V.N. and Morozova, T.Y., *Electrospray deposition as a method to fabricate functionally active protein films.* Analytical chemistry, 1999. **71**(7): p. 1415-1420.

12.   Kebarle, P., *A brief overview of the present status of the mechanisms involved in electrospray mass spectrometry.* Journal of Mass Spectrometry, 2000. **35**(7): p. 804-817.

13. Cloupeau, M. and Prunet-Foch, B., *Electrostatic spraying of liquids in cone-jet mode.* Journal of Electrostatics, 1989. **22**(2): p. 135-159.

14. Cole, R.B., *Some tenets pertaining to electrospray ionization mass spectrometry.* Journal of Mass Spectrometry, 2000. **35**(7): p. 763-772.

15. Kebarle, P. and Tang, L., *From ions in solution to ions in the gas phase-the mechanism of electrospray mass spectrometry.* Analytical Chemistry, 1993. **65**(22): p. 972A-986A.

16. La Mora, D. and Fernandez, J., *The current emitted by highly conducting Taylor cones.* Journal of Fluid Mechanics, 1994. **260**: p. 155-184.

17. Shaffer, S.A., Tang, K., Anderson, G.A., Prior, D.C., Udseth, H.R., and Smith, R.D., *A novel ion funnel for focusing ions at elevated pressure using electrospray ionization mass spectrometry.* Rapid Communications in Mass Spectrometry, 1997. **11**(16): p. 1813-1817.

18. Shaffer, S.A., Prior, D.C., Anderson, G.A., Udseth, H.R., and Smith, R.D., *An ion funnel interface for improved ion focusing and sensitivity using electrospray ionization mass spectrometry.* Analytical chemistry, 1998. **70**(19): p. 4111-4119.

19. Kim, T., Tang, K., Udseth, H.R., and Smith, R.D., *A multicapillary inlet jet disruption electrodynamic ion funnel interface for improved sensitivity using atmospheric pressure ion sources.* Analytical chemistry, 2001. **73**(17): p. 4162-4170.

20. *Development of World's Most Sensitive Tripple Quad MS*.   April 4, 2015]; Available   from: http://www.chem.agilent.com/Library/slidepresentation/Public/6490LCMS_QQQ_ presentation.pdf.

21. Blazek, J., *Computational Fluid Dynamics: Principles and Applications:(Book with accompanying CD)*. 2005: Elsevier.

22. Fenn, J.B., *Mass spectrometric implications of high-pressure ion sources.* International journal of mass spectrometry, 2000. **200**(1): p. 459-478.

23. Versteeg, H.K. and Malalasekera, W., *An introduction to computational fluid dynamics: the finite volume method*. 2007: Pearson Education.

24. O'Hanlon, J.F., *A user's guide to vacuum technology*. 2005: John Wiley & Sons.

25. Belotserkovskii, O.M., Oparin, A.M., and Chechetkin, V.M., *Turbulence: New Approaches*. 2005: Cambridge Int Science Publishing.

26. Ockendon, H. and Ockendon, J.R., *Waves and Compressible Flow*. Texts in Applied Mathematics. 2004, New York: Springer Science & Business Media.

27. Murphy, H.R. and Miller, D.R., *Effects of nozzle geometry on kinetics in free-jet expansions.* The Journal of Physical Chemistry, 1984. **88**(20): p. 4474-4478.

28. Launder, B.E. and Spalding, D., *The numerical computation of turbulent flows.* Computer methods in applied mechanics and engineering, 1974. **3**(2): p. 269-289.

29. Wilcox, D.C., *Reassessment of the scale-determining equation for advanced turbulence models.* AIAA journal, 1988. **26**(11): p. 1299-1310.

30. Menter, F., Kuntz, M., and Langtry, R., *Ten years of industrial experience with the SST turbulence model.* Turbulence, heat and mass transfer, 2003. **4**(1).

31. Menter, F.R., *Zonal two equation k-turbulence models for aerodynamic flows.* AIAA paper, 1993. **2906**: p. 1993.

32. Menter, F.R., *Two-equation eddy-viscosity turbulence models for engineering applications.* AIAA journal, 1994. **32**(8): p. 1598-1605.

33. Bartosiewicz, Y., Aidoun, Z., Desevaux, P., and Mercadier, Y., *Numerical and experimental investigations on supersonic ejectors.* International Journal of Heat and Fluid Flow, 2005. **26**(1): p. 56-70.

34. Jasak, H., Jemcov, A., and Tukovic, Z. *OpenFOAM: A C++ library for complex physics simulations*. in *International workshop on coupled methods in numerical dynamics*. 2007.

35. Greenshields, C.J., Weller, H.G., Gasparini, L., and Reese, J.M., *Implementation of semi-discrete, non-staggered central schemes in a colocated, polyhedral, finite volume framework, for high-speed viscous flows.* International journal for numerical methods in fluids, 2010. **63**(1): p. 1-21.

36. Kurganov, A. and Tadmor, E., *New high-resolution central schemes for nonlinear conservation laws and convection–diffusion equations.* Journal of Computational Physics, 2000. **160**(1): p. 241-282.

37. Kurganov, A. and Petrova, G., *Central-upwind schemes on triangular grids for hyperbolic systems of conservation laws.* Numerical Methods for Partial Differential Equations, 2005. **21**(3): p. 536-552.

38. Van Leer, B., *Towards the ultimate conservative difference scheme. II. Monotonicity and conservation combined in a second-order scheme.* Journal of computational physics, 1974. **14**(4): p. 361-370.

39. Ladenburg, R., Winckler, J., and Van Voorhis, C., *Interferometric studies of faster than sound phenomena. Part I. The gas flow around various objects in a free, homogeneous, supersonic air stream.* Physical Review, 1948. **73**(11): p. 1359.

40. Ladenburg, R., Van Voorhis, C., and Winckler, J., *Interferometric studies of faster than sound phenomena. Part II. Analysis of supersonic air jets.* Physical Review, 1949. **76**(5): p. 662.

41. SIMION. *SIMION® Version 8.1* 2015; Available from: http://www.simion.com.

42. Dahl, D.A., *SIMION for the personal computer in reflection.* International Journal of Mass Spectrometry, 2000. **200**(1–3): p. 3-25.

43. Lynn, E.C., Chung, M.-C., and Han, C.-C., *Characterizing the transmission properties of an ion funnel.* Rapid Communications in Mass Spectrometry, 2000. **14**(22): p. 2129-2134.

44. Kelly, R.T., Tolmachev, A.V., Page, J.S., Tang, K., and Smith, R.D., *The ion funnel: theory, implementations, and applications.* Mass spectrometry reviews, 2010. **29**(2): p. 294-312.

45. Julian, R.R., Mabbett, S.R., and Jarrold, M.F., *Ion Funnels for the Masses: Experiments and Simulations with a Simplified Ion Funnel.* Journal of the American Society for Mass Spectrometry, 2005. **16**(10): p. 1708-1712.

46. Gibson, I., Rosen, D.W., and Stucker, B., *Additive manufacturing technologies*. 2010: Springer.

47. Crump, S.S., *Apparatus and method for creating three-dimensional objects*. 1992, Google Patents.

48. Stratasys. *About Stratasys*. 2015 [cited 2015 September 23].

49. Jones, R., Haufe, P., Sells, E., Iravani, P., Olliver, V., Palmer, C., and Bowyer, A., *RepRap–the replicating rapid prototyper.* Robotica, 2011. **29**(01): p. 177-191.

50. Thrimurthulu, K., Pandey, P.M., and Venkata Reddy, N., *Optimum part deposition orientation in fused deposition modeling.* International Journal of Machine Tools and Manufacture, 2004. **44**(6): p. 585-594.

51. Hossain, M.S., Ramos, J., Espalin, D., Perez, M., and Wicker, R. *Improving tensile mechanical properties of FDM-manufactured specimens via modifying build parameters*. in *International Solid Freeform Fabrication Symposium: An Additive Manufacturing Conference. Austin, TX*. 2013.

52. Ahn, S.-H., Montero, M., Odell, D., Roundy, S., and Wright, P.K., *Anisotropic material properties of fused deposition modeling ABS.* Rapid Prototyping Journal, 2002. **8**(4): p. 248-257.

53. Lee, C., Kim, S., Kim, H., and Ahn, S., *Measurement of anisotropic compressive strength of rapid prototyping parts.* Journal of materials processing technology, 2007. **187**: p. 627-630.

54. Bellini, A. and Güçeri, S., *Mechanical characterization of parts fabricated using fused deposition modeling.* Rapid Prototyping Journal, 2003. **9**(4): p. 252-264.

55. Agarwala, M.K., Jamalabad, V.R., Langrana, N.A., Safari, A., Whalen, P.J., and Danforth, S.C., *Structural quality of parts processed by fused deposition.* Rapid Prototyping Journal, 1996. **2**(4): p. 4-19.

103

56.   Stratasys. *Finishing Processes*. 2015 [cited 2015 September 4, 2015]; Available from: http://www.stratasys.com/solutions/finishing-processes/electroplating.

57.   McCullough, E.J. and Yadavalli, V.K., *Surface modification of fused deposition modeling ABS to enable rapid prototyping of biomedical microdevices.* Journal of Materials Processing Technology, 2013. **213**(6): p. 947-954.

58.   Cater, M.R.S., *Permeability and Porosity Reduction of Fused Deposition Modeling Parts via Internal Epoxy Injection Methods*. 2014, The Ohio State University.

59.   Stratasys. *uPrint SE Plus*. 2015   [cited 2015 September 28]; Available from: http://www.stratasys.com/3d-printers/idea-series/uprint-se-plus.

60.   Schlesinger, M. and Paunovic, M., *Modern electroplating*. Vol. 55. 2011: John Wiley & Sons.

61.   Paunovic, M. and Schlesinger, M., *Fundamentals of electrochemical deposition*. Vol. 45. 2006: john wiley & sons.

62.   Budevski, E.B., Staikov, G.T., and Lorenz, W.J., *Electrochemical phase formation and growth: an introduction to the initial stages of metal deposition*. 2008: John Wiley & Sons.

63.   Sandlin, S., Kinnunen, T., Rämö, J., and Sillanpää, M., *A simple method for metal re-coating of optical fibre Bragg gratings.* Surface and Coatings Technology, 2006. **201**(6): p. 3061-3065.

64.   Siggia, S. and Segal, E., *Determination of Aldehydes in Presence of Acids, Ketones, Acetals, and Vinyl Ethers.* Analytical Chemistry, 1953. **25**(4): p. 640-642.

65. Curtis, H.D., *METHODS OF SILVERING MIRRORS.* Publications of the Astronomical Society of the Pacific, 1911. **23**(135): p. 13-32.

66. Mallory, G.O. and Hajdu, J.B., *Electroless plating: fundamentals and applications*. 1990: William Andrew.

67. Xia, Y., Venkateswaran, N., Qin, D., Tien, J., and Whitesides, G.M., *Use of electroless silver as the substrate in microcontact printing of alkanethiols and its application in microfabrication.* Langmuir, 1998. **14**(2): p. 363-371.

68. Systems, S.R. *Residual Gas Analyzers*. 2015 [cited 2015 October 2]; Available from: http://www.thinksrs.com/downloads/PDFs/Catalog/RGAc.pdf.

69. O'Shea, J.N., Taylor, J.B., Swarbrick, J.C., Magnano, G., Mayor, L.C., and Schulte, K., *Electrospray deposition of carbon nanotubes in vacuum.* Nanotechnology, 2007. **18**(3): p. 035707.

70. Kim, T., Tolmachev, A.V., Harkewicz, R., Prior, D.C., Anderson, G., Udseth, H.R., Smith, R.D., Bailey, T.H., Rakov, S., and Futrell, J.H., *Design and Implementation of a New Electrodynamic Ion Funnel.* Analytical Chemistry, 2000. **72**(10): p. 2247-2255.

71. Tang, K., Tolmachev, A.V., Nikolaev, E., Zhang, R., Belov, M.E., Udseth, H.R., and Smith, R.D., *Independent control of ion transmission in a jet disrupter dual-channel ion funnel electrospray ionization MS interface.* Analytical chemistry, 2002. **74**(20): p. 5431-5437.

72. Gerlich, D., *Inhomogeneous RF Fields: A Versatile Tool for the Study of Processes with Slow Ions*, in *Advances in Chemical Physics*. 2007, John Wiley & Sons, Inc. p. 1-176.

73.   Menter, F., Kuntz, M., and Langtry, R., *Ten years of industrial experience with the SST turbulence model.* Turbulence, heat and mass transfer, 2003. **4**: p. 625-632.

74.   Geuzaine, C. and Remacle, J.F., *Gmsh: A 3-D finite element mesh generator with built-in pre-and post-processing facilities.* International Journal for Numerical Methods in Engineering, 2009. **79**(11): p. 1309-1331.

75.   Ding, L., Sudakov, M., and Kumashiro, S., *A simulation study of the digital ion trap mass spectrometer.* International Journal of Mass Spectrometry, 2002. **221**(2): p. 117-138.

76.   He, L. and Lubman, D.M., *Simulation of External Ion Injection, Cooling and Extraction Processes with SIMION 6.0 for the Ion Trap/Reflectron Time-of-flight Mass Spectrometer.* Rapid Communications in Mass Spectrometry, 1997. **11**(13): p. 1467-1477.

77.   Chernushevich, I.V. and Thomson, B.A., *Collisional cooling of large ions in electrospray mass spectrometry.* Analytical chemistry, 2004. **76**(6): p. 1754-1760.

78.   Powell, A., *The sound-producing oscillations of round underexpanded jets impinging on normal plates.* The Journal of the Acoustical Society of America, 1988. **83**(2): p. 515-533.

79.   Iavarone, A., Jurchen, J., and Williams, E., *Effects of solvent on the maximum charge state and charge state distribution of protein ions produced by electrospray ionization.* Journal of the American Society for Mass Spectrometry, 2000. **11**(11): p. 976-985.

80.   Belov, M.E., Gorshkov, M.V., Udseth, H.R., Anderson, G.A., Tolmachev, A.V., Prior, D.C., Harkewicz, R., and Smith, R.D., *Initial implementation of an electrodynamic ion funnel with Fourier transform ion cyclotron resonance mass spectrometry.* Journal of the American Society for Mass Spectrometry, 2000. **11**(1): p. 19-23.

81.   Li, Z., Berger, H., Okamoto, K., Zhang, Q., Luscombe, C.K., Cao, G., and Schlaf, R., *Measurement of the Internal Orbital Alignment of Oligothiophene-TiO2 Nanoparticle Hybrids.* Journal of Physical Chemistry C, 2013. **117**(27): p. 13961-13970.

82.   Wang, W., Alsmeier, J.H., Wolak, M., and Schlaf, R., *Determination of the charge neutrality level of poly (3-hexylthiophene).* Journal of chemical physics, 2013. **138**(5): p. 054705.

83.   Dole, M., Mack, L.L., Hines, R.L., Mobley, R.C., Ferguson, L.D., and Alice, M.B., *Molecular Beams of Macroions.* Journal of Chemical Physics, 1968. **49**(5): p. 2240-2249.

84.   Smith, J.N., Flagan, R.C., and Beauchamp, J., *Droplet evaporation and discharge dynamics in electrospray ionization.* Journal of Physical Chemistry A, 2002. **106**(42): p. 9957-9967.

85.   Gerlich, D., *Inhomogeneous RF Fields: A Versatile Tool for the Study of Processes with Slow Ions*. Advances in Chemical Physics. 2007: John Wiley & Sons, Inc. 37.

86.   Comyn, J., *Polymer permeability*. 2012: Springer Science & Business Media.

87.   Chatham, H., *Oxygen diffusion barrier properties of transparent oxide coatings on polymeric substrates.* Surface and Coatings Technology, 1996. **78**(1): p. 1-9.

88.   Kwon, J.-S., Jang, C.H., Jung, H., and Song, T.-H., *Vacuum maintenance in vacuum insulation panels exemplified with a staggered beam VIP.* Energy and Buildings, 2010. **42**(5): p. 590-597.

89.   Markkula, S., Storck, S., Burns, D., and Zupan, M., *Compressive Behavior of Pyramidal, Tetrahedral, and Strut‑Reinforced Tetrahedral ABS and Electroplated Cellular Solids.* Advanced Engineering Materials, 2009. **11**(1‑2): p. 56-62.

90.   Kannan, S. and Senthilkumaran, D., *Investigating the Influence of Electroplating Layer Thickness on the Tensile Strength for Fused Deposition Processed ABS Thermoplastics.* International Journal of Engineering and Technology, 2014. **6**(2): p. 1047-1052.

91.   Stratasys. *Material Safety Data Sheet ABSPlus P430*. 2013   [cited 2015 September   4,   2015];   Available   from: http://usglobalimages.stratasys.com/Main/Secure/MSDS/P430-ABS_M30-ABS_Model/MSDS EU P430 US English.pdf.

92.   Thouless, M., *Combined buckling and cracking of films.* Journal of the American Ceramic Society, 1993. **76**(11): p. 2936-2938.

93.   Stratasys. *ABSlus-P430 Production-Grade Thermoplastic for Design Series 3D Printer*. 2015   [cited 2015 September 10]; Available from: http://usglobalimages.stratasys.com/Main/Secure/Material   Specs   MS/Fortus-Material-Specs/Fortus-MS-ABSplus-01-13-web.pdf.

94. McCarthy, D. and Williams, C. *Creating complex hollow metal geometries using additive manufacturing and electroforming*. in *International Solid Freeform Fabrication Symposium*. 2012.

95. Stratasys. *Ultem 9085 Resin*. 2015 [cited 2015 October 1]; Available from: http://www.stratasys.com/materials/fdm/~/media/83DA2BBEE7DE4A669CFEF6B 1FCA118AA.ashx.

109

APPENDIX A: PERMISSIONS

Below is the copyright permission for Figure 3 in Chapter 2.

To view this email as a web page, go here.

Do Not Reply Directly to This Email

To ensure that you continue to receive our emails,
please add rightslink@marketing.copyright.com to your address book.

RightsLink

Copyright Clearance Center

Thank You For Your Order!

Dear Mr. Eric Tridas,

Thank you for placing your order through Copyright Clearance Center's RightsLink service. Elsevier has partnered with RightsLink to license its content. This notice is a confirmation that your order was successful.

Your order details and publisher terms and conditions are available by clicking the link below:
http://s100.copyright.com/CustomerAdmin/PLF.jsp?ref=f4f9b06e-ae90-41d0-8992-dcce0da3d46a

Order Details
Licensee: Eric Miguel Tridas
License Date: Sep 22, 2015
License Number: 3714340211975
Publication: Journal of Electrostatics
Title: Electrostatic spraying of liquids in cone-jet mode
Type Of Use: reuse in a thesis/dissertation
Total: 0.00 USD

To access your account, please visit https://myaccount.copyright.com.

Please note: Online payments are charged immediately after order confirmation; invoices are issued daily and are payable immediately upon receipt.

To ensure that we are continuously improving our services, please take a moment to complete our customer satisfaction survey.

B.1:v4.2

+1-855-239-3415 / Tel: +1-978-646-2777
customercare@copyright.com
http://www.copyright.com

This email was sent to: **eric.m.tridas@gmail.com**

Below is the copyright permission for Figure 4 in Chapter 2.

To view this email as a web page, go here.

Do Not Reply Directly to This Email

To ensure that you continue to receive our emails,
please add rightslink@marketing.copyright.com to your address book.

RightsLink

Copyright Clearance Center

Thank You For Your Order!

Dear Mr. Eric Tridas,

Thank you for placing your order through Copyright Clearance Center's RightsLink service. John Wiley and Sons has partnered with RightsLink to license its content. This notice is a confirmation that your order was successful.

Your order details and publisher terms and conditions are available by clicking the link below:
http://s100.copyright.com/CustomerAdmin/PLF.jsp?ref=aa6b4b84-ea5f-4dea-8e09-e48acf09af94

Order Details
Licensee: Eric Miguel Tridas
License Date: Sep 22, 2015
License Number: 3714340753078
Publication: Journal of Mass Spectrometry
Title: Some tenets pertaining to electrospray ionization mass spectrometry
Type Of Use: Dissertation/Thesis
Total: 0.00 USD

To access your account, please visit https://myaccount.copyright.com.

Please note: Online payments are charged immediately after order confirmation; invoices are issued daily and are payable immediately upon receipt.

To ensure that we are continuously improving our services, please take a moment to complete our customer satisfaction survey.

B.1:v4.2

+1-855-239-3415 / Tel: +1-978-646-2777
customercare@copyright.com
http://www.copyright.com

Below is the copyright permission for Figure 7 Chapter 2.

To view this email as a web page, go here.

Do Not Reply Directly to This Email

To ensure that you continue to receive our emails,
please add rightslink@marketing.copyright.com to your address book.

RightsLink | Copyright Clearance Center

Thank You For Your Order!

Dear Mr. Eric Tridas,

Thank you for placing your order through Copyright Clearance Center's RightsLink service. Elsevier has partnered with RightsLink to license its content. This notice is a confirmation that your order was successful.

Your order details and publisher terms and conditions are available by clicking the link below:
http://s100.copyright.com/CustomerAdmin/PLF.jsp?ref=1cbf8226-ef89-4532-9e7b-a030878cdbbd

Order Details
Licensee: Eric Miguel Tridas
License Date: Sep 22, 2015
License Number: 3714341472872
Publication: International Journal of Mass Spectrometry
Title: Mass spectrometric implications of high-pressure ion sources
Type Of Use: reuse in a thesis/dissertation
Total: 0.00 USD

To access your account, please visit https://myaccount.copyright.com.

Please note: Online payments are charged immediately after order confirmation; invoices are issued daily and are payable immediately upon receipt.

To ensure that we are continuously improving our services, please take a moment to complete our customer satisfaction survey.

B.1:v4.2

+1-855-239-3415 / Tel: +1-978-646-2777
customercare@copyright.com
http://www.copyright.com

This email was sent to: **eric.m.tridas@gmail.com**

Below is the copyright permission for Figure 8 in Chapter 2.

To view this email as a web page, go here.

Do Not Reply Directly to This Email

To ensure that you continue to receive our emails,
please add rightslink@marketing.copyright.com to your address book.

RightsLink

Copyright Clearance Center

Your Request Has Been Submitted

Dear Mr. Eric Tridas,

Thank you for submitting your request through Copyright Clearance Center's RightsLink service. Emerald Group Publishing Limited has partnered with RightsLink to license its content online.

Your request will be reviewed within fifteen business days by a member of Emerald Group Publishing Limited permissions team, after which time you will receive an email with a royalty fee set by Emerald Group Publishing Limited. **At that time, you must accept the fee and terms to complete the order.**

Please Note: Emerald Group Publishing Limited may deny your request or you may decline an approved request. In either case, you will receive an e-mail notification. You will not be charged for any request not accepted by you.

Your requested order details are available by clicking the link below:
https://s100.copyright.com/CustomerAdmin/SVP3.jsp?ref=427521d6-7b89-4dac-a3a7-e40186036de6&pName=emerald

Order Details

Licensee:	Eric Miguel Tridas
Order Date:	Sep 25, 2015
Order Number:	501053640
Publication:	Rapid Prototyping Journal
Title:	Mechanical characterization of parts fabricated using fused deposition modeling
Type of Use:	Dissertation/Thesis
Total:	Not Available

B.3:v6.6

+1-855-239-3415 / Tel: +1-978-646-2777
customercare@copyright.com
http://www.copyright.com

113

www.manaraa.com

Below is the copyright permission for Figure 9 in Chapter 2.

To view this email as a web page, go here.

Do Not Reply Directly to This Email

To ensure that you continue to receive our emails,
please add rightslink@marketing.copyright.com to your address book.

RightsLink

Copyright Clearance Center

Thank You For Your Order!

Dear Mr. Eric Tridas,

Thank you for placing your order through Copyright Clearance Center's RightsLink service. John Wiley and Sons has partnered with RightsLink to license its content. This notice is a confirmation that your order was successful.

Your order details and publisher terms and conditions are available by clicking the link below:
http://s100.copyright.com/CustomerAdmin/PLF.jsp?ref=db010e3e-605d-4e3a-9367-6543aef37425

Order Details
Licensee: Eric Miguel Tridas
License Date: Sep 22, 2015
License Number: 3714350510138
Publication: International Journal for Numerical Methods in Fluids
Title: Implementation of semi-discrete, non-staggered central schemes in a colocated, polyhedral, finite volume framework, for high-speed viscous flows
Type Of Use: Dissertation/Thesis
Total: 0.00 USD

To access your account, please visit https://myaccount.copyright.com.

Please note: Online payments are charged immediately after order confirmation; invoices are issued daily and are payable immediately upon receipt.

To ensure that we are continuously improving our services, please take a moment to complete our customer satisfaction survey.

B.1:v4.2

+1-855-239-3415 / Tel: +1-978-646-2777
customercare@copyright.com
http://www.copyright.com

Below is the copyright permission for Figure 12 in Chapter 2.

To view this email as a web page, go here.

Do Not Reply Directly to This Email

To ensure that you continue to receive our emails,
please add rightslink@marketing.copyright.com to your address book.

RightsLink | Copyright Clearance Center

Your Request Has Been Submitted

Dear Mr. Eric Tridas,

Thank you for submitting your request through Copyright Clearance Center's RightsLink service. Emerald Group Publishing Limited has partnered with RightsLink to license its content online.

Your request will be reviewed within fifteen business days by a member of Emerald Group Publishing Limited permissions team, after which time you will receive an email with a royalty fee set by Emerald Group Publishing Limited. **At that time, you must accept the fee and terms to complete the order.**

Please Note: Emerald Group Publishing Limited may deny your request or you may decline an approved request. In either case, you will receive an e-mail notification. You will not be charged for any request not accepted by you.

Your requested order details are available by clicking the link below:
https://s100.copyright.com/CustomerAdmin/SVP3.jsp?ref=427521d6-7b89-4dac-a3a7-e40186036de6&pName=emerald

Order Details

Licensee:	Eric Miguel Tridas
Order Date:	Sep 25, 2015
Order Number:	501053640
Publication:	Rapid Prototyping Journal
Title:	Mechanical characterization of parts fabricated using fused deposition modeling
Type of Use:	Dissertation/Thesis
Total:	Not Available

B.3:v6.6

+1-855-239-3415 / Tel: +1-978-646-2777
customercare@copyright.com
http://www.copyright.com

This email was sent to: **eric.m.tridas@gmail.com**

Below is the copyright permission for the content in Chapter 3.

RightsLink — Copyright Clearance Center

Thank You For Your Order!

Dear Mr. Eric Tridas,

Thank you for placing your order through Copyright Clearance Center's RightsLink service. John Wiley and Sons has partnered with RightsLink to license its content. This notice is a confirmation that your order was successful.

Your order details and publisher terms and conditions are available by clicking the link below:
http://s100.copyright.com/CustomerAdmin/PLF.jsp?ref=8b359690-8fe0-4784-b17c-25ac4ff495e4

Order Details
Licensee: Eric Miguel Tridas
License Date: Sep 2, 2015
License Number: 3700780961305
Publication: Journal of Mass Spectrometry
Title: Enhanced simulation of an RF ion funnel including gas turbulence
Type Of Use: Dissertation/Thesis
Total: 0.00 USD

To access your account, please visit https://myaccount.copyright.com.

Please note: Online payments are charged immediately after order confirmation; invoices are issued daily and are payable immediately upon receipt.

To ensure that we are continuously improving our services, please take a moment to complete our customer satisfaction survey.

B.1:v4.2

+1-855-239-3415 / Tel: +1-978-646-2777
customercare@copyright.com
http://www.copyright.com

Below is the copyright permission for the content in Chapter 4.

To view this email as a web page, go here.

Do Not Reply Directly to This Email

To ensure that you continue to receive our emails,
please add rightslink@marketing.copyright.com to your address book.

RightsLink
Copyright Clearance Center

Thank You For Your Order!

Dear Mr. Eric Tridas,

Thank you for placing your order through Copyright Clearance Center's RightsLink service. John Wiley and Sons has partnered with RightsLink to license its content. This notice is a confirmation that your order was successful.

Your order details and publisher terms and conditions are available by clicking the link below:
http://s100.copyright.com/CustomerAdmin/PLF.jsp?ref=3faa52a4-bc04-46e2-b24c-6e62e499ae7a

Order Details
Licensee: Eric Miguel Tridas
License Date: Sep 2, 2015
License Number: 3700781111440
Publication: Journal of Mass Spectrometry
Title: High transmission 3D printed flex-PCB-based ion funnel
Type Of Use: Dissertation/Thesis
Total: 0.00 USD

To access your account, please visit https://myaccount.copyright.com.

Please note: Online payments are charged immediately after order confirmation; invoices are issued daily and are payable immediately upon receipt.

To ensure that we are continuously improving our services, please take a moment to complete our customer satisfaction survey.

B.1:v4.2

+1-855-239-3415 / Tel: +1-978-646-2777
customercare@copyright.com
http://www.copyright.com